

# Characterization of Extruded and 3D-Printed PETG Using Multi-Relaxation Test

by

XINRUI CUI

A thesis submitted in partial fulfilment of the requirements for the degree of

Master of Science

Department of Mechanical Engineering  
University of Alberta

© XINRUI CUI, 2022

## Abstract

Fused deposition modelling (FDM) is one of the most popular additive manufacturing (AM) methods, FDM can produce complex shapes at low cost in a short time, Polyethylene terephthalate glycol (PETG) is a popular FDM material which has increasingly been used due to its ease for printing, good chemical resistance, strong durability and odourless. Since material performance of the parts printed by FDM is lower than that using traditional manufacturing methods, mainly due to presence of voids and weak bonding between filaments. In addition, difference in the printing parameters also affects the FDM performance. It is therefore necessary to compare and characterize performance of PETG prepared using different manufacturing methods and, for the FDM method, using different printing parameters.

In this study, a newly developed test method, named multi-relaxation (MR) test, is used to characterize the relaxation behaviour of PETG specimens. Five types of PETG specimens were manufactured for the testing, including the conventionally extruded PETG, and 3D printed PETG specimens of  $[0^\circ]$ ,  $[\pm 30^\circ]_s$ ,  $[\pm 45^\circ]_s$  and  $[90^\circ]$  using FDM. The MR test results were analyzed using Eyring's model with four parameters to describe the relaxation behaviour at fixed strokes. These parameters are initial viscous stress at the onset of relaxation,  $\sigma_r(0)$ , reference stress,  $\sigma_0$ , time-independent quasi-static (QS) stress,  $\sigma_{st}$ , and relaxation time,  $\tau_r$ . For  $[90^\circ]$  specimen, however, only the QS elastic modulus ( $E_x$ ) could be determined due to its brittle behaviour, which was determined using both MR test and monotonic tensile test. For the other four types of PETG specimens, two types of specimens, i.e., with and without holes in the tab sections, were evaluated. The MR test results suggest that the holes in the tab sections can significantly reduce specimen performance, especially for  $[0^\circ]$  and  $[\pm 30^\circ]_s$  specimens. Therefore, specimens without holes were used to evaluate the influence of raster angle on the relaxation behaviour of PETG.

Comparisons of MR test results among different types of specimens suggest that  $[0^\circ]$  specimens are less stiff than the extruded specimens, but after removing the effect of voids in the former, these two types of specimens show very similar relaxation behaviour. Among 3D printed specimens, their stiffness is in the order of  $[0^\circ] > [\pm 30^\circ]_s > [\pm 45^\circ]_s$ . Those 3D printed specimens also showed different fracture behaviours. In particular,  $[0^\circ]$  specimens did not show any sign of fracture in the test, but  $[\pm 30^\circ]_s$  and  $[\pm 45^\circ]_s$  specimens started fracturing during the middle of the test.

For each type of PETG specimens, the relationship between total applied stress and its QS and viscous stress components and the variation of relaxation parameters ( $\sigma_0$  and  $\tau_r$ ) with stroke were investigated. Three transition points were detected in the deformation process. Variation of applied stress, QS stress,  $\sigma_r(0)$ ,  $\sigma_0$  and  $\tau_r$  among PETG 3D printed specimens was investigated, which indicated that the  $[\pm 30^\circ]_s$  specimens showed a different profile of stress-stroke curve after the second transition point from the other 3D printed specimens. The corresponding values for  $\sigma_r(0)$ ,  $\sigma_0$  and  $\tau_r$  after the second transition point are also different from their values for the other 3D printed specimens.

The study also examined applicability of the classical laminate theory (CLT) to prediction of the QS elastic modulus ( $E_x$ ) for 3D printed specimens. The results suggest that the CLT is applicable to the  $E_x$  prediction, but the prediction accuracy could be improved by consider the effect of voids on the mechanical performance.

## **Preface**

The purpose of this research is to entitle the Master of Science at the University of Alberta to 'XINRUI CUI'. No part of this thesis has been published previously.

## Acknowledgments

This is a unique and unforgettable research experience that I never had before. Although this is a challenging and tough time because of the pandemic, I still cherish and appreciate this opportunity that can help me learn new skills and motivate my potential. I sincerely thank my supervisor, my group members, and my family for their support to me so that I could complete the master's degree.

First, I would like to give much appreciation to my supervisor Dr. P-Y Ben Jar, for giving me this opportunity to be in his group to do the research and give me lots of suggestions and guidance when I proceed with my research. I also want to thank the skillful staff in the MEC E machine shop to machine and print my specimens and staff in NanoFab for training me using microscopes and analysis scanned 3D image results from X-ray microscope.

Then I would like to thank my group members, Donna, Furui, Hanlin and Steve for sharing their research experience with me and giving me suggestions when I face challenges. I appreciate your selfless help both academically and mentally.

Finally, I want to give much appreciation to my family. They have given me financial support so that I can study overseas. I would not be able to finish my degree without their help and

## Table of Contents

<b>Abstract</b> .....	<b>ii</b>
<b>Preface</b> .....	<b>iv</b>
<b>Acknowledgments</b> .....	<b>v</b>
<b>Lists of Tables</b> .....	<b>x</b>
<b>Lists of Figures</b> .....	<b>xi</b>
<b>Lists of Symbols</b> .....	<b>xvi</b>
<b>Chapter 1 Introduction</b> .....	<b>1</b>
1.1 Background and motivation .....	1
1.2 Review of literature on 3D printed PETG and multi-relaxation test.....	2
1.3 Thesis objective and outline.....	3
<b>Chapter 2 Test methods and test conditions used to characterize PETG</b> .....	<b>5</b>
2.1 Specimen dimensions and preparation.....	5
2.1.1 Extruded PETG dog-bone specimens.....	5
2.1.2 3D printed dog-bone specimens.....	6
2.2 Test method: Multi-Relaxation (MR) test.....	9
2.3 Test condition .....	11
2.3.1 Gripping method one.....	11
2.3.2 Gripping method two.....	12
2.4 Analysis of the MR test results.....	14
2.4.1 Model and equations .....	14
2.4.2 Curving fitting of the relaxation behavior .....	15

2.5 Determining the best test condition to be used for characterizing PETG specimens .....	19
2.5.1 Extruded PETG specimens .....	19
2.5.2 [0°] specimens .....	21
2.5.3 [±30°]s specimens.....	23
2.5.4 [±45°]s specimens.....	26
2.6 Methods used to obtain QS elastic modulus .....	28
2.6.1 Using MR test to obtain the QS stress-stroke relationship for PETG specimens .....	28
2.6.2 Monotonic tensile test.....	28
2.6.3 Finite element simulation of QS stress-stroke curve to calculate the QS elastic modulus .....	28
2.7 Measurement of volume ratio for 3D printed specimens.....	30
<b>Chapter 3 Characterization of mechanical behaviour of extruded and 3D printed PETG specimens .....</b>	<b>33</b>
3.1 Test results for [90°] 3D printed specimens.....	33
3.1.1 MR test results .....	33
3.1.2 Monotonic tensile test results.....	35
3.2 Analysis and discussion of MR test results between [0°] and extruded PETG specimens ..	36
3.3 Analysis and discussion of MR test results for 3D printed PETG specimens of [0°], [±30°]s, and [±45°]s .....	38
3.4 Relationship among QS stress, applied stress, and fitting parameters for the extruded specimens .....	40
3.5 Comparison of QS stress, applied stress and relaxation parameters among specimens of different types.....	43
3.5.1 Applied stress and QS stress versus stroke curves .....	44
3.5.2 Applied stress and $\sigma r(0)$ .....	45
3.5.3 Applied stress and $\sigma_0$ versus stroke curve .....	46

3.5.4 Applied stress and $\tau$ .....	48
<b>Chapter 4 Analysis of test results using the classical laminate theory .....</b>	<b>50</b>
4.1 Review of classical laminate theory and literature review.....	50
4.1.1 Analytical equations from CLT for FDM parts .....	50
4.1.2 Literature review .....	53
4.2 Approach of applying CLT .....	55
4.2.1 Applying analytical equations from CLT to 3D printed specimens .....	55
4.2.2 Determining E1 and E2 .....	55
4.2.3 Prediction of the elastic constants .....	59
4.2.4 Prediction QS elastic modulus $E_x$ using CLT .....	66
4.3 Modified CLT using effective $E_m$ to predict $E_x$ .....	68
4.3.1 Difference of interlaminar contact area among specimens of different raster angle configurations .....	69
4.3.2 Prediction of QS elastic modulus $E_x$ using modified CLT .....	70
<b>Chapter 5 Summary and future works.....</b>	<b>73</b>
5.1 Summary of current work .....	73
5.2 Future work .....	74
<b>APPENDIX .....</b>	<b>76</b>
Appendix A Detail calculations of applying CLT equations to 3D printed specimen.....	76
Appendix B MATLAB code for solving the system of equations from elasticity model approach.....	79
Appendix C Detail calculations of the prediction of QS elastic modulus for $[\pm\theta^\circ]_s$ 3D printed specimen .....	80
Appendix D MATLAB code for solving the system of equations with adjusted $E_m$ for elasticity model approach .....	81



**Bibliography.....83**

## Lists of Tables

Table 2-1 Printing parameters of 3D printed specimens.....	7
Table 4-1 Elastic constants for $[0^\circ]$ 3D printed specimen using two prediction approaches with four combinations of E1 and E2, grey cells are the data known and white cells are predicted data. ....	66
Table 4-2 Predicted results using CLT for $[\pm 30^\circ]$ s and $[\pm 45^\circ]$ s specimens, grey cells are the average values of the results for the four E1 and E2 combinations and Max/Min predicted values. ....	67
Table 4-3 Predicted elastic constants for prediction of $E_x$ , based on adjusted $E_m$ and original $E_f$ , grey cells are the data known and white cells are predicted data. ....	70
Table 4-4 Prediction of results using modified CLT for $[\pm 30^\circ]$ s and $[\pm 45^\circ]$ s specimens, grey cells are the average values of the results for the four E1 and E2 combinations and Max/Min predicted values. ....	71

## Lists of Figures

Figure 2-1 Clear extruded PETG sheet (with a nominal thickness of 1/8”)	5
Figure 2-2 Schematic description of the dog-bone specimen (with holes)	6
Figure 2-3 Sample water jetted PETG dog-bone specimen (with holes)	6
Figure 2-4 Schematic description of 3D printed PETG plate, (a)dimension, (b) Isometric view	7
Figure 2-5 Definition of raster angle $\alpha^\circ$ (a) and schematic description of layer configurations for four types of 3D printed specimens: $[0^\circ]$ (b), $[\pm 30^\circ]$ s (c), $[\pm 45^\circ]$ s (d), and $[90^\circ]$ (e)	9
Figure 2-6 Typical MR test results: (a) engineering stress vs. stroke (b) engineering stress vs. time	10
Figure 2-7 Experimental set up (method one)	11
Figure 2-8 Schematic diagram for method one with the gripping region in blue	11
Figure 2-9 Extruded PETG dog-bone specimens after MR tests (method one): (a) with holes, (b) without holes	12
Figure 2-10 Experiment set up (method two)	13
Figure 2-11 Schematic diagram for gripping method two with the gripping region in blue	13
Figure 2-12 Gripping method two for extruded PETG dog-bone specimens with holes after the MR tests	13
Figure 2-13 Schematic diagram of the standard, viscoelastic model used for the analysis of MR test results	14
Figure 2-14 Example of stress drop occurring in the MR tests as a function of time at the relaxation stroke of 1.54mm and the best fitting curve generated based on Equation 2-8 using the following values for the fitting parameters: $\sigma_0 = 6\text{MPa}$ , $\sigma_r(0)=13.2\text{MPa}$ , and $\tau_r = 8000\text{s}$ : (a) linear time scale and (b) logarithmic time scale.	16
Figure 2-15 Experimental data (in blue, same as in Figure 2-14) and the best fitting curve (in red, $\sigma_0 = 6\text{MPa}$ , $\sigma_r(0)=13.2\text{MPa}$ , and $\tau_r = 8000\text{s}$ ); the rest of the curves are generated based on the following changes of fitting parameters using equation (8): $\sigma_0 = 5\text{MPa}$ (in green), $\sigma_r(0)=12.2\text{MPa}$ (in black), or $\tau_r = 5500\text{s}$ (in orange).	17
Figure 2-16 Examples of stress drop occurred in the MR tests as a function of time at certain strokes in the logarithmic scale and the best fitting curve generated based on Equation 2-8 using the following values for the fitting parameters,(a) stroke=0.1mm, $\sigma_0 = 0.05\text{MPa}$ ,	

$\sigma_r(0)=0.39\text{MPa}$ , and  $\tau_r = 2200\text{s}$ , (b) stroke=1.1mm,  $\sigma_0 = 1.5\text{MPa}$ ,  $\sigma_r(0)=6.2\text{MPa}$ , and  $\tau_r = 12000\text{s}$ , (c) stroke=2.1mm,  $\sigma_0 = 5.4\text{MPa}$ ,  $\sigma_r(0)=8.4\text{MPa}$ , and  $\tau_r = 5500\text{s}$ .....18

Figure 2-17 Comparison of parameters analyzed from the MR test results for an extruded specimen: (a)  $\sigma_{st}$ , (b) $\sigma_0$ , (c) $\sigma_r0$ , and (d) $\tau_r$  .....21

Figure 2-18  $[0^\circ]$  3D printed PETG specimens after MR tests (a) with holes using gripping method one, (b) with holes using gripping method two, (c) no holes using gripping method one. ....22

Figure 2-19 Comparison of parameters analyzed from the MR test results for a  $[0^\circ]$  specimen: (a)  $\sigma_{st}$ , (b) $\sigma_0$ , (c) $\sigma_r0$ , and (d) $\tau_r$ .....23

Figure 2-20  $[\pm 30^\circ]$ s 3D printed PETG specimens after MR tests (a) with holes using gripping method one, (b) with holes using gripping method two, (c) no holes using gripping method one .....24

Figure 2-21 Comparison of parameters analyzed from the MR test results for  $[\pm 30^\circ]$ s 3D printed specimen, plotted as a function of stroke: (a)  $\sigma_{st}$ , (b) $\sigma_0$ , (c) $\sigma_r0$ , and (d)  $\tau_r$  .....25

Figure 2-22  $[\pm 45^\circ]$ s 3D printed PETG specimens after MR tests (a) with holes using gripping method one, (b) with holes using gripping method two, (c) no holes using gripping method one. ....26

Figure 2-23 Comparison of analyzed MR test parameters vs. stroke for  $[\pm 45^\circ]$ s 3D printed specimens with different combinations of specimen types and gripping methods, (a)  $\sigma_{st}$ , (b) $\sigma_0$ , (c) $\sigma_r0$ , (d)  $\tau_r$  .....27

Figure 2-24 (a) The meshed model for FE simulation, and (b) a typical contour plot after small deformation.....29

Figure 2-25 Zeiss ZEISS Xradia Versa 620 X-Ray Microscope used to scan 3D printed specimens, (a), whole X-ray Microscope, (b), detail view.....30

Figure 2-26 3D scanned area of the 3D printed specimens (a)  $[0^\circ]$ , (b)  $[\pm 30^\circ]$ s and (c)  $[\pm 45^\circ]$ s .....31

Figure 2-27 Determining the volume fractions of filament and voids in the selected region using Dragonfly: (a) Front view, (b) Sectional view of the blacked region in (a), and (c) 3D view of blackened region in (a).....32

Figure 2-28 Reconstructed 3D model after segmentation: (a) reconstructed 3D model for segmented filament only, (b) reconstructed 3D model for segmented voids only and (c) reconstructed 3D model including segmented filament and voids. ....	32
Figure 3-1 MR test results for a [90°] specimen: (a) QS stress and applied stress, (b) $\sigma_0$ , (c) $\sigma_r(0)$ , and (d) $\tau_r$ .....	34
Figure 3-2 [90°] 3D printed PETG specimen with holes after MR tests using gripping method one.....	35
Figure 3-3 Engineering stress vs. stroke for [90°] 3D printed specimens from monotonic tensile test.....	36
Figure 3-4 Comparison of MR test results vs. stroke between extruded and [0°] 3D printed PETG specimens, circles stand for the maximum stress of each type of specimen. (a) QS stress (b) Applied stress (c) $\sigma_r(0)$ (d) the ratio of quasi-static stress/applied stress.....	37
Figure 3-5 Comparison of MR test results between three different types of 3D printed PETG specimens, circles stand for the maximum stress of each type of specimen, (a) Quasi-static stress vs. stroke, (b) Applied stress vs. stroke, (c) $\sigma_r(0)$ vs. stroke, (d) The ratio of quasi-static stress/applied stress vs. stroke. ....	40
Figure 3-6 MR test results as a function of stroke for an extruded PETG specimen, with three dashed black circles standing for three transition points on the applied stress curve,:(a) QS stress and applied stress, blue circles stand for the transition points of the QS stress curve (b) $\sigma_r(0)$ and applied stress trend curve. (c) $\sigma_0$ and applied stress trend curve, and (d) $\tau_r$ and applied stress trend curve. ....	43
Figure 3-7 QS stress and applied stress versus stroke curves for different types of 3D printed specimens, blue circles stand for the transition points of the QS stress curve, black open circles stand for three transition points of applied stress curve, (a) [0°], (b) [ $\pm 30^\circ$ ]s, (c) [ $\pm 45^\circ$ ]s .....	45
Figure 3-8 Applied stress and $\sigma_r(0)$ versus stroke curves for different types of 3D printed specimens, black open circles stand for three transition points of applied stress curve, (a) [0°], (b) [ $\pm 30^\circ$ ]s, (c) [ $\pm 45^\circ$ ]s .....	46
Figure 3-9 Applied stress and $\sigma_0$ versus stroke curves for different types of 3D printed specimens, black open circles stand for three transition points of applied stress curve, (a) [0°], (b) [ $\pm 30^\circ$ ]s, (c) [ $\pm 45^\circ$ ]s .....	48

Figure 3-10 Applied stress and  $\tau_r$  versus stroke curves for different types of 3D printed specimens, black open circles stand for three transition points of applied stress curve, (a)  $[0^\circ]$ , (b)  $[\pm 30^\circ]$ s, (c)  $[\pm 45^\circ]$ s .....49

Figure 4-1 Schematic of an angle lamina showing local 1-2 and global x-y coordinate systems. 51

Figure 4-2 Schematic description of an n-layered laminate .....52

Figure 4-3 Curve fittings for MR test results of a  $[0^\circ]$  3D printed specimen vs. stroke: (a) Linear curve fitting for the initial applied stress, with circles to indicate the overshooting of applied engineering stress at the onset of the relaxation stages,(b) Polynomial curve fitting for the first three points of  $\sigma_r(0)$ .....57

Figure 4-4 Linear fitting of QS stress vs. stroke quadratic function based on experimental data with FEM simulation results for a  $[0^\circ]$  3D printed specimen, using QS elastic modulus of  $E_1=1800\text{MPa}$  .....57

Figure 4-5 The initial slopes of engineering stress vs. stroke curves for  $[90^\circ]$  3D printed specimens using MR test and monotonic tensile test.....58

Figure 4-6 Segment processing of scanned 3D printed specimens in which five different stages (darkened area) were chosen for a 3D printed specimen: (a)  $[0^\circ]$ , (b)  $[\pm 30^\circ]$ s, (c) imperfections in the  $[\pm 30^\circ]$ s at the right side, (d) imperfections in the  $[\pm 30^\circ]$ s at the left side, and (e)  $[\pm 45^\circ]$ s .....60

Figure 4-7 Plot of filament volume ratio  $V_f$ , in % of total volume, vs. raster angle ( $^\circ$ ) with error bar of 1% for three different types of 3D printed specimens. Five stages were chosen for each type of specimens.....61

Figure 4-8 Cross section view of representative volume element (RVE) of a unidirectional lamina based on mechanics of materials approach, blue area is filament and white area is matrix. ....63

Figure 4-9 RVE of a unidirectional lamina based on CCA model(left), front view 1-2 axis(middle) and top view 2-3 axis (right). .....64

Figure 4-10 Predicted  $E_x$  using CLT with two approaches to predict  $G_{12}$  and FEM simulation of experiment results for 3D printed specimens with different angles. ....68

Figure 4-11 Schematic description of difference of interlaminar area (blue area) among different raster angle configurations using  $1\text{mm}^2$  unit cell: (a)  $[0^\circ]$  interlaminar area of  $0.88\text{mm}^2$ , (b)  $[\pm 30^\circ]$ s interlaminar area of  $0.73\text{mm}^2$ , and (c)  $[\pm 45^\circ]$ s interlaminar area is  $0.73\text{mm}^2$ .....69

Figure 4-12 Predicted  $E_x$  using modified CLT with adjusted  $E_m$  equals to 83% of original  $E_m$ , the original CLT prediction results using two prediction elastic constants approaches, and FEM simulation of experimental  $E_x$  results. ....72

## Lists of Symbols

AM	Additive manufacturing
3D printing	Three-dimensional printing
FDM	Fused deposition modelling
SLA	Stereolithography
SLS	Selective laser sintering
PLA	Polylactic Acid
ABS	Acrylonitrile Butadiene Styrene
PETG	Polyethylene terephthalate glycol
PET	Polyethylene Terephthalate
GTH	Generalized Time Hardening
PE	Polyethylene
MR	Multi-relaxation
CLT	Classical laminate theory
XCT	X-ray computed tomography
FE	Finite element
$\sigma_A$	Applied stress
QS	Quasi-static
$\sigma_r$	Viscous stress
$\sigma_{st}$	Quasi-static stress
$\tau_r$	Relaxation time
$\sigma_0$	Reference stress
E	Elastic modulus
$\bar{Q}_{ij_{\pm\theta}}$	Stiffness matrix for the $\pm[\theta]_s$ 3D printed specimen
$\bar{Q}_{ij_{\pm\theta}}^*$	Compliance matrix for $\pm[\theta]_s$ 3D printed specimen
$E_1$	Quasi-static elastic modulus in the filament direction
$E_2$	Quasi-static elastic modulus in the transverse direction
$G_{12}$	In-plane shear modulus
$\nu_{12}$	Major Poisson's ratio
$\nu_{21}$	Minor Poisson's ratio
$E_x$	Quasi-static elastic modulus in x-direction
$E_f$	Filament quasi-static elastic modulus
$E_m$	Average matrix quasi-static elastic modulus $E_m$



# Chapter 1 Introduction

## 1.1 Background and motivation

Additive manufacturing (AM), also known as three-dimensional printing (3D printing), has become one of the most popular and advanced manufacturing technologies [1][2]. There are three well established 3D printing methodologies, namely, fused deposition modelling (FDM), stereolithography (SLA), and selective laser sintering (SLS) [3][4][5][6]. Fused deposition modelling (FDM) is the most commonly used AM process. In FDM, the selected thermoplastic polymer is melted and then extruded to build a three-dimensional object in a pre-determined path layer by layer [3][4]. FDM can be widely used in many manufacturing fields including aerospace, biomedical, prototyping, automotive, and many others [7][8][9][10]. The main advantage of FDM technology is the ability to directly produce parts with complex shapes in a short time with low cost and reduced material waste. The most commonly used 3D printed thermoplastic materials are PLA and ABS [3][4]. Recently, many other materials are increasingly used as well, each having its advantage. Polyethylene terephthalate glycol (PETG) is one of the materials due to its ease of printing, good layer adhesion, and odourless [11].

PETG is a variation of a popular plastic polyethylene terephthalate (PET). PET is commonly used in food containers and water bottles. A glycol-modified version of PET is formed by adding glycol during the polymerization process, known as PETG. PETG is more durable, less brittle, clearer, and easier to use than PET. PETG is an amorphous material with melting temperature of 260°C and glass transition temperature of 80°C [54], PETG has also been widely used as drink bottles, food containers, and medical fields due to its excellent durability, good adhesion, resistance to water and chemicals, food safety, and odourless [11][12] and hence becomes one of the popular 3D printing materials.

FDM are known to cause decrease in the material performance, compared with the conventional extrusion process, due to voids and weak bonding between filaments and between layers. In addition, printing parameters, such as raster angle, printing speed, layer thickness, etc., are also known to affect mechanical properties for FDM parts [13][14]. Therefore, it is desired to compare performance of PETG prepared using different manufacturing methods and printed using different printing parameters.

## 1.2 Review of literature on 3D printed PETG and multi-relaxation test

Several researchers already investigated the influence of processing parameters on the quality of FDM PETG parts. For example, Barrios et al. [15] investigate the effect of layer height, extruding temperature, flow rate, print acceleration and printing speed on the surface characteristics of the PETG specimens (such as surface roughness, sliding angle, and contact angle) using the Taguchi method and ANOVA (Analysis of Variance) [16] [17]. The results showed that flow rate and print acceleration have the strongest influence on the surface quality of FDM PETG parts. Guessasma et al. [18] investigated the effect of nozzle temperature on the tensile strength of PETG, and showed that the PETG filament must be printed at the temperature over 230°C. However, when the nozzle temperature is set at 250°C, the porosity increases. In addition, the FDM process reduces tensile strength and stiffness by up to 40%, compared to the values for the raw PETG.

The printing parameter that was focused in my study is the raster angle. Sepahi et al. [19] studied the effects of five different raster angles (0°, 90°, 45°, 0°/90°, +45°/-45°) for ABS, PLA, and PETG FDM parts using the tensile test. For PETG, the results showed that the highest and lowest values for elongation and strength occurred at raster angles of 0° and 90°, respectively, +45°/-45° specimen has higher values than 45° specimen, and values for 0°/90° specimen are between those for +45°/-45° and 45° specimens. Khosravani [20] used uniaxial tensile test to study the fracture behaviour and structure performance of 3D-printed PETG with different raster angles of 0°, 45°, and 90°, raster widths of 0.75mm and 1mm and layer thickness of 0.2mm and 0.5mm. The results show that 0° specimens have the highest stiffness and strength. In addition, the layer thickness of 0.2mm showed a higher fracture load, which is in a good agreement with another study [21].

In the literature, most of the mechanical properties for FDM parts are determined using the monotonic, uniaxial tensile test. Among a few studies that paid attention to relaxation behaviour of FDM parts, Salazar-Martín [22] used stress relaxation to study the time-dependent mechanical properties of polyetherimide (PEI). They found that the applied stress decreased more than 20% in a relaxation time of 300min, and that the generalized time hardening (GTH) model [23] [24] was able to predict the stress relaxation behavior of PEI parts. Tan [25] developed multi-relaxation (MR) test to determine the first critical stroke for polyethylene (PE), the concept of the MR test is similar to that by Hong et al. [26], both using stress relaxation behaviour to characterize the

material state. The main advantage of the MR test is to allow the use of one specimen for all stress relaxation stages to avoid the potential inconsistency among specimens, which is a common problem for 3D printed specimens.

### 1.3 Thesis objective and outline

The main objective of this study is to use MR test to characterize PETG specimens that were produced with two manufacturing methods, i.e., conventional extrusion and 3D printing [25]. The latter considered four different raster angle configurations ( $0^\circ$ ,  $\pm 30^\circ$ ,  $\pm 45^\circ$  and  $90^\circ$ ), but for  $[90^\circ]$  specimen, only the quasi-static (QS) elastic modulus ( $E_x$ ) could be determined, as the material was so brittle that fracture was generated at a very early stage of the test (second relaxation cycle). The first comparison presented here is between the extruded and 3D printed  $[0^\circ]$  PETG, and the second comparison the performance of 3D printed PETG specimens with different raster angle configurations ( $0^\circ$ ,  $\pm 30^\circ$  and  $\pm 45^\circ$ ). This study also checked whether the classical laminate theory (CLT), calibrated using  $E_x$  values measured from unidirectional specimens of  $0^\circ$  and  $90^\circ$ , could predict  $E_x$  for 3D printed specimens of  $[\pm 30^\circ]_s$  and  $[\pm 45^\circ]_s$ .

Chapter 2 illustrates the preparation of extruded and 3D printed PETG specimens, introduces details of the testing method and analysis approach, and describes three different test conditions used for MR test, among which the best condition was used for the testing and analysis, in chapter 3. Chapter 2 also illustrates the technical details for measuring the volume ratio of filament in the 3D printed specimens and the analysis to determine  $E_x$  of PETG specimens, based on MR test results during the initial loading stage or monotonic tensile test for  $[90^\circ]$  specimens. In addition, this chapter describes the finite element modelling (FEM) procedure to obtain QS elastic modulus of PETG specimens after calibration based on the experimental QS stress-stroke curves.

Chapter 3 demonstrates first the MR test results and monotonic tensile test results for  $[90^\circ]$  specimens to determine the QS stress-stroke relationship. Then, the chapter is focused on the use of MR tests on specimens without holes and gripping method one, as described in chapter 2, to characterize different types of PETG specimens, which includes (i) comparison of the MR tests results between conventional extruded PETG and 3D printed PETG  $[0^\circ]$  specimen, (ii) comparison among three types of 3D printed specimens of different raster angle configurations. The last section is focus on the analysis of QS stress, applied stress and fitting parameters (including  $\sigma_0$ ,  $\sigma_r(0)$  and  $\tau_r$ ) as a function of stroke.

Chapter 4 introduces firstly the concept of CLT and reviews some studies done by other researchers, and then illustrates the approach for applying CLT to prediction of  $E_x$  for  $[\pm 30^\circ]_s$  and  $[\pm 45^\circ]_s$  3D printed PETG specimens, validated by comparison with the experimental data. The last part of Chapter 4 introduces modifications of CLT that considers the effect of the voids content to different types of 3D printed specimens.

Chapter 5 summarizes findings from this study and provides some suggestions and ideas that can be used in the future study.

## Chapter 2 Test methods and test conditions used to characterize PETG

### 2.1 Specimen dimensions and preparation

#### 2.1.1 Extruded PETG dog-bone specimens

The extruded PETG dog-bone specimens were obtained from water-jetting the commercial clear PETG sheet, with a nominal thickness of 1/8", as shown in Figure 2-1.

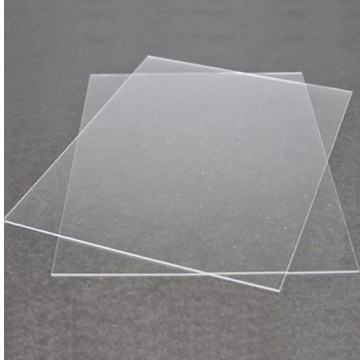


*Figure 2-1 Clear extruded PETG sheet (with a nominal thickness of 1/8")*

Dimensions of PETG specimens with holes in the tab region are shown in Figure 2-2, Figure 2-3 is a sample of water-jetted extruded PETG dog-bone specimen with holes.

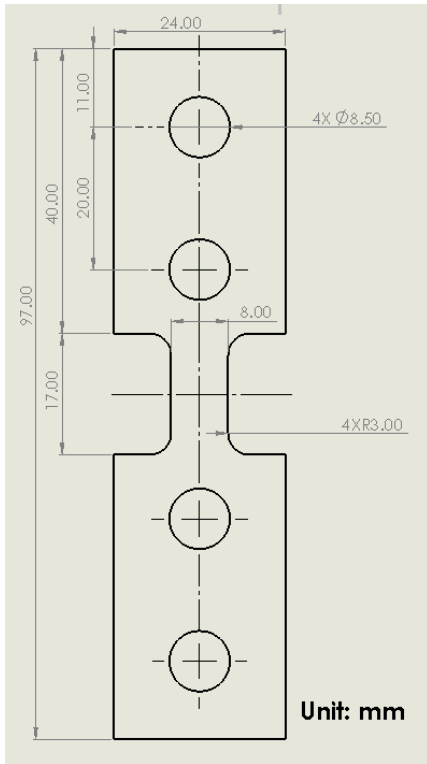


Figure 2-2 Schematic description of the dog-bone specimen (with holes)



Figure 2-3 Sample water jetted PETG dog-bone specimen (with holes)

The holes in the tab region were designed for a special rig that is used to study the effect of the test environment on mechanical properties for plastics. PETG dog-bone specimens without holes in the tab region were also prepared, which have the same dimensions as those specimens with holes but removing the holes in the tab region.

#### 2.1.2 3D printed dog-bone specimens

The 3D printed PETG plates were fabricated using DREMEL 3D45 3D printer (FDM technique) with PETG filament, Dimensions of 3D printed PETG plate are illustrated in Figure 2-4. Each plate was used to manufacture one 3D printed dog-bone specimen using water-jet cutting. 3D printed dog-bone specimens have the same dimensions as the extruded dog-bone specimens, but the former has a nominal thickness of 3.2mm, while the extruded specimens 1/8" (3.175mm). Details of the printing parameters for each type of 3D printed specimen are given in Table 2-1. Basically, different types of 3D printed specimens had different raster angle configurations, but identical for all other printing parameters.

Rather than 3D printing the final dimensions of the specimens, 3D printing PETG plates and then water-jet cutting the dog-bone specimens has several advantages. Firstly, a dog-bone specimen has a relatively complex shape, compared to a plate. The former may cause local inconsistency in the specimen. Secondly, due to the thermal effect introduced in the 3D printing process, residual stress exists in the 3D printed specimens [27]. If the dog-bone specimens were produced by 3D printing directly, residual stress at the ends of the gauge section and around the holes could be different from the other areas, and the difference may vary among specimens with different raster angles. 3D printing plates first and then water-jet cutting the dog-bone specimens from the plates could avoid the above uncontrollable inconsistency.

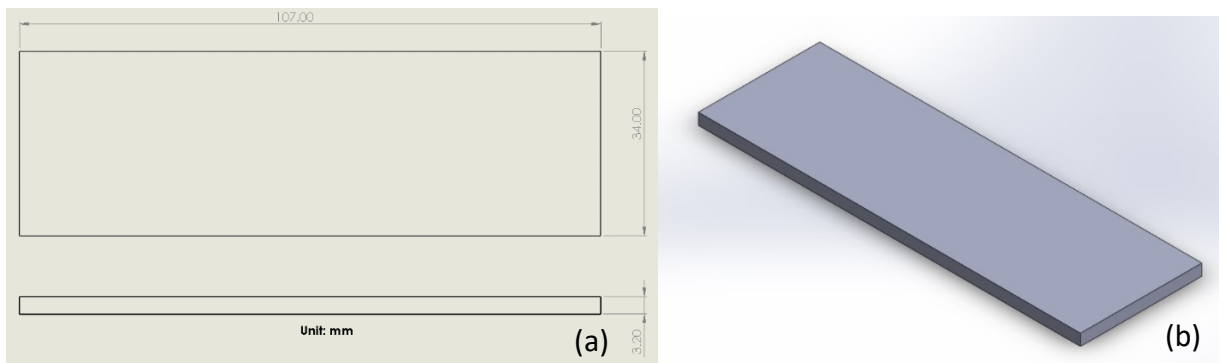


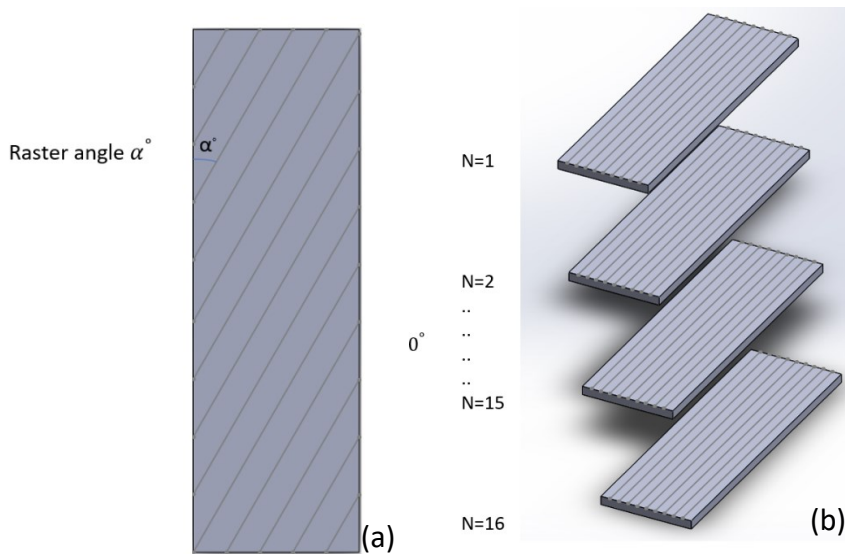
Figure 2-4 Schematic description of 3D printed PETG plate, (a)dimension, (b) Isometric view

Table 2-1 Printing parameters of 3D printed specimens

	[0°]	[±30°] <sub>s</sub>	[±45°] <sub>s</sub>	[90°]
Layer thickness	0.2 mm	0.2 mm	0.2mm	0.2mm
Filament diameter	1.75 mm	1.75 mm	1.75 mm	1.75 mm
Nozzle diameter	0.4 mm	0.4mm	0.4 mm	0.4 mm
Nozzle temperature	250°C	250°C	250°C	250°C
Bed temperature	80°C	80°C	80°C	80°C
Infill percentage	100%	100%	100%	100%
Print speed	60 mm/s	60 mm/s	60 mm/s	60 mm/s
Raster angle	0°	±30°	±45°	90°

Figure 2-5 (a) gives definition of raster angle, i.e., the angle between the printing direction and the long edge the specimen. Figure 2-5 (b) describes the layer configuration for [0°] specimens, in which filaments in all layers were printed in the direction that is parallel to the long edge and is parallel to the loading direction in the test. Figure 2-5(c) describes the layer configuration for

$[\pm 30^\circ]_s$  specimens, 0.2mm thick for each layer with the total thickness of 3.2mm, i.e., 16 layers for each specimen. The plane of symmetry in the specimens is between layer numbers 8 and 9. That is, printing layers have raster angle of  $+30^\circ$  and  $-30^\circ$  alternatively till layer number 8, and then  $-30^\circ$  and  $+30^\circ$  alternatively from numbers 9 to 16 so that the raster angles are symmetric about the middle plane.  $[\pm 45^\circ]_s$  specimens were printed using same layer configuration as  $[\pm 30^\circ]_s$  specimens but using raster angle of  $\pm 45^\circ$  instead of  $\pm 30^\circ$ , as shown in Figure 2-5 (d). While for  $[90^\circ]$  specimens, filaments in all layers were printed in the transverse direction, i.e., perpendicular to the loading direction, as shown in Figure 2-5 (e).





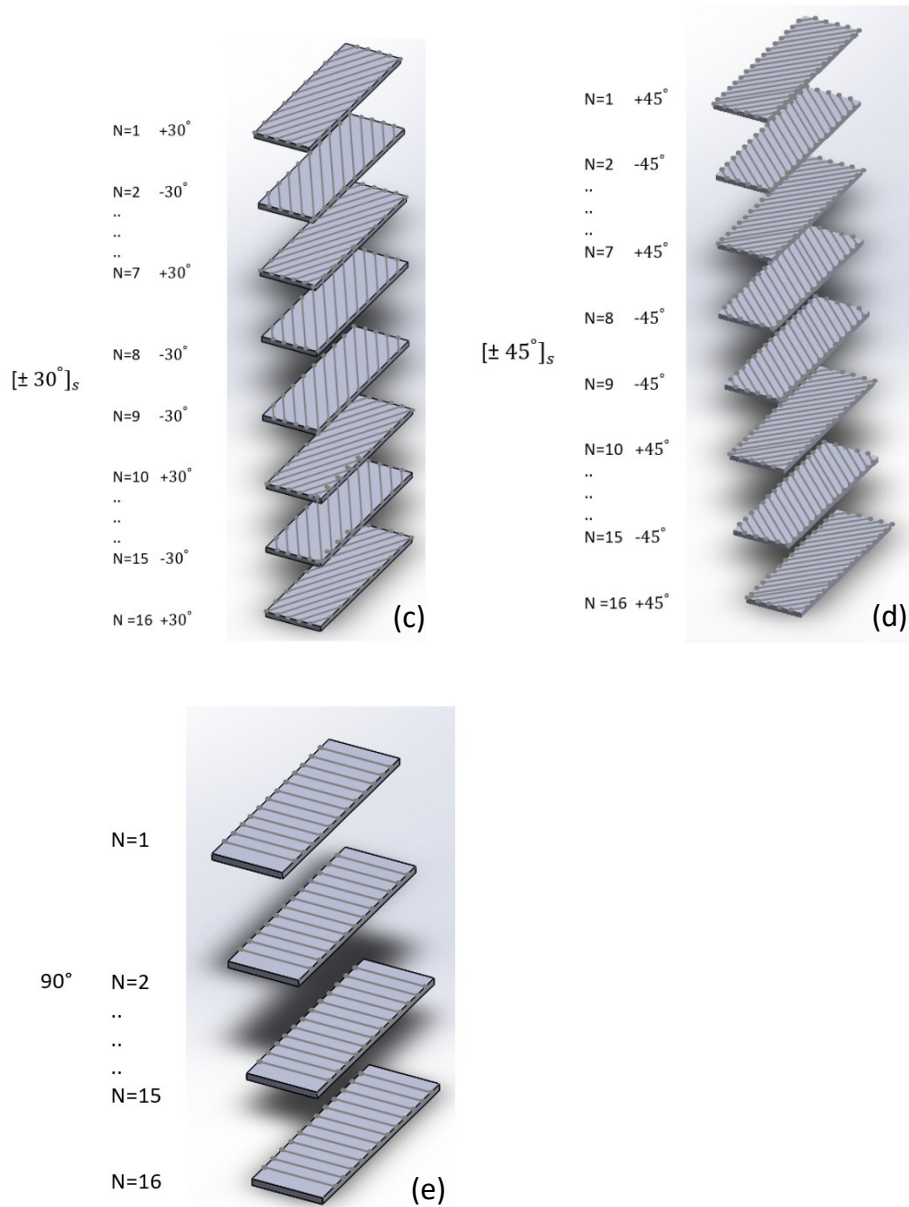


Figure 2-5 Definition of raster angle  $\alpha^\circ$  (a) and schematic description of layer configurations for four types of 3D printed specimens:  $[0^\circ]$  (b),  $[\pm 30^\circ]_s$  (c),  $[\pm 45^\circ]_s$  (d), and  $[90^\circ]$  (e)

## 2.2 Test method: Multi-Relaxation (MR) test

The main test method used to characterize the PETG specimens was the MR test [25]. The MR tests were conducted using a universal test machine (Qualitest Quasar 100, Lauderdale, FL, USA), with the crosshead speed of 5mm/min during the loading stage, with stroke increment of about

0.15mm, after each loading stage followed by a relaxation stage at a fixed stroke. Each relaxation stage is for a period of 10,000 seconds. Each test was stopped either after 24 loading and relaxation stages or when the specimen fractured, whichever happened first. Load, time, and stroke were recorded for the whole test. Thickness and width for the gauge section were measured for each specimen before the test.

Engineering stress was calculated based on the recorded load and the original cross-sectional area using Equation 2-1 below:

$$\sigma_{Eng} = \frac{P}{Wt} \quad \text{Equation 2-1}$$

where  $\sigma_{Eng}$  is engineering stress, P is load recorded during the test, W specimen width and t thickness of the gauge section all of which were measured before the test.

Figure 2-6 (a) shows a typical curve of engineering stress vs. stroke using an extruded PETG specimen. Note that drop of the engineering stress during the relaxation stage was insignificant at strokes before 0.75 mm. The stress drop increased before the engineering stress reached the peak value, at the stroke about 1.25 mm in Figure 2-6 (a). After the peak engineering stress, the engineering stress dropped and eventually reached a plateau region. Figure 2-6 (b) shows the corresponding curve of engineering stress vs. time from the same test, showing that during each relaxation stage, stress drop is not a linear function of time. Rather, the stress dropped fast at the beginning of the relaxation stage and then slowed down with the further increase of time.

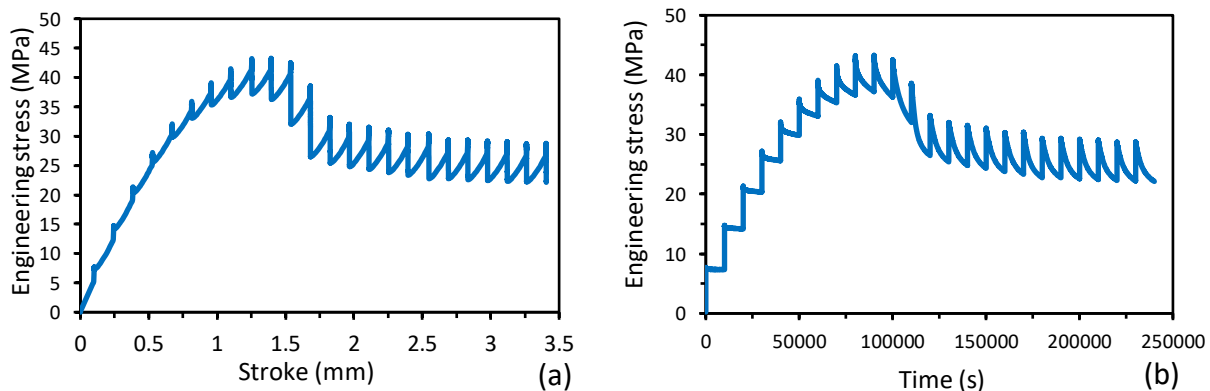


Figure 2-6 Typical MR test results: (a) engineering stress vs. stroke (b) engineering stress vs. time

### 2.3 Test condition

In this section, three test conditions are introduced for the MR test. Two test conditions are for specimens with holes and without holes using the same gripping method, named gripping method one below. The other test condition is by using gripping method two for specimens with holes. The holes in 3D printed specimens are filled with LePage Epoxy 5-Minute Syringe to strength the region around the holes.

#### 2.3.1 Gripping method one

The gripping method one was used for both ‘with holes’ and ‘without holes’ specimens, which is shown in Figure 2-7. Using gripping method one, edges of the specimen gauge section were aligned with the edge of two steel blocks. This is the gripping method originally intended for the test. In this case, the gripping region is shown in Figure 2-8, which as shown in the dark blue area, is 10 mm away from the edge of the specimen tab.

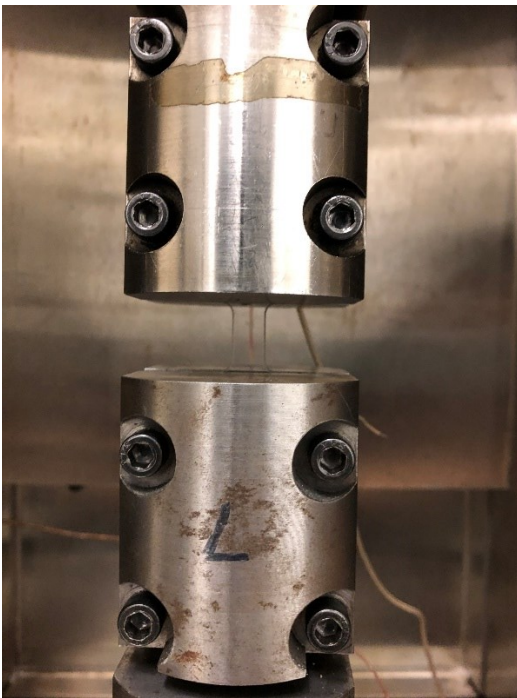


Figure 2-7 Experimental set up (method one)

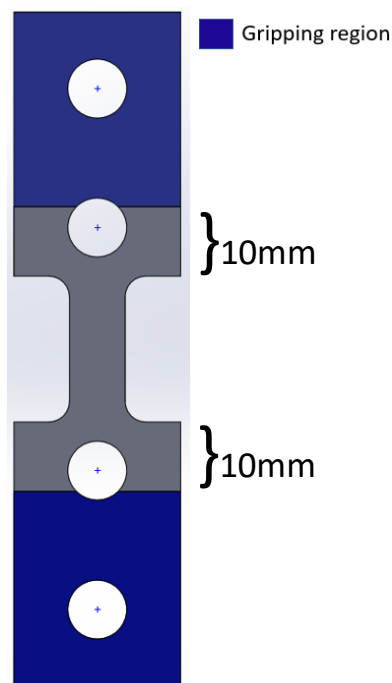
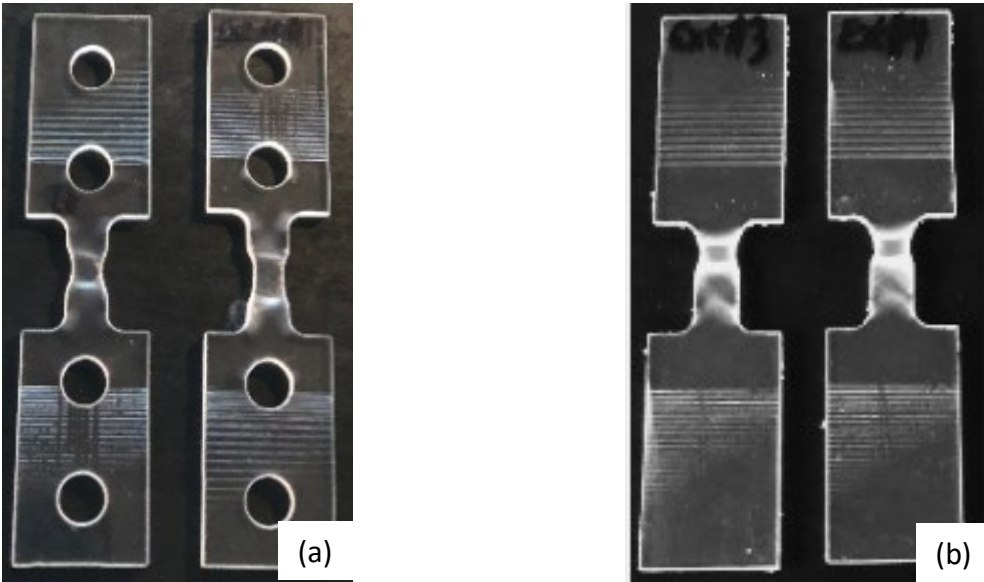


Figure 2-8 Schematic diagram for method one with the gripping region in blue

Figure 2-9 (a) and (b) shows the extruded PETG specimens after MR tests under two different test conditions, i.e., with holes and without holes using gripping method one. They both showed no fracture at the end of the tests. The regions with indent lines are the gripping regions.



*Figure 2-9 Extruded PETG dog-bone specimens after MR tests (method one): (a) with holes, (b) without holes*

As shown in Figure 2-9 (a), for specimens with holes using gripping method one, only half of the hole close to the gauge section was gripped, this could potentially initiate fracture from the hole for the 3D printed specimens. Therefore, another gripping method was introduced, as discussed in the next section.

### 2.3.2 Gripping method two

The gripping method two is used only for specimens with holes, as shown in Figure 2-10, edges of the gauge section are 15mm away from the edges of the blocks. In this case, the total length of the true gauge section would be increased. As shown in Figure 2-11, the gripping regions would be 15 mm away from the edge of the gauge section so the region with the holes near the gauge section caused increase of the specimen compliance. Figure 2-12 shows the extruded PETG specimens after MR tests using gripping method two, the marked lines on the specimens show the gripping region.

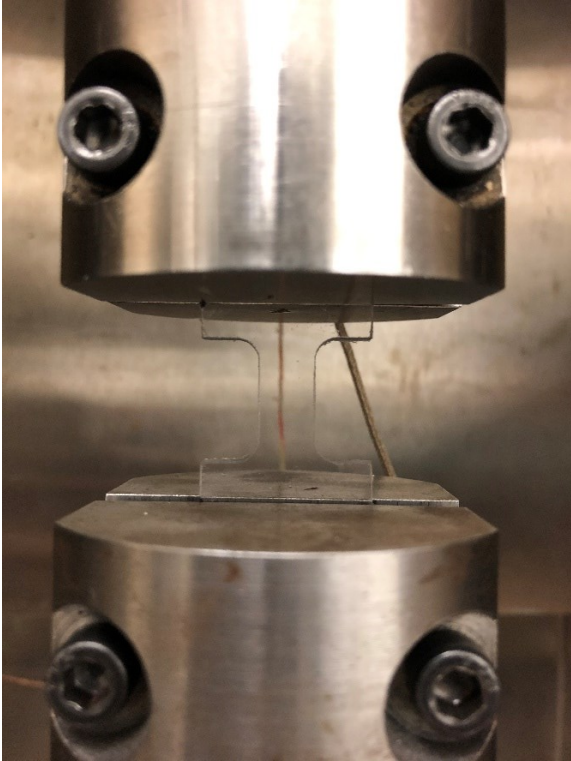


Figure 2-10 Experiment set up (method two)

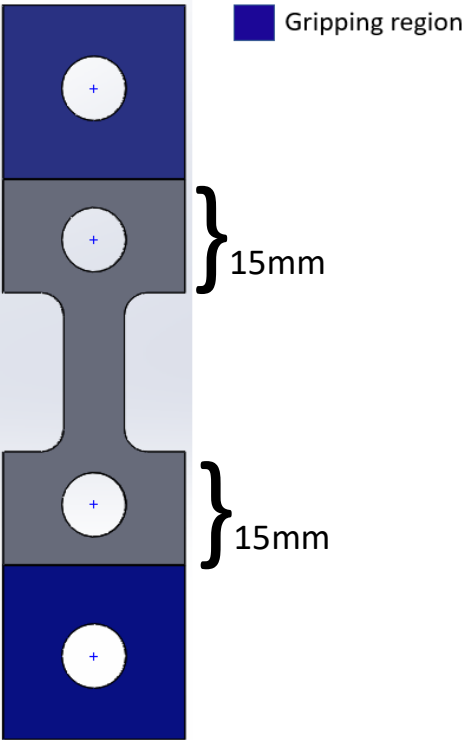


Figure 2-11 Schematic diagram for gripping method two with the gripping region in blue



Figure 2-12 Gripping method two for extruded PETG dog-bone specimens with holes after the MR tests

## 2.4 Analysis of the MR test results

### 2.4.1 Model and equations

Analysis of the MR test results was based on a standard, viscoelastic model as shown in Figure 2-13 in which the upper branch represents the time-dependent viscous stress response, consisting of a spring with modulus  $E_r$  and a damper with strain rate  $\dot{\epsilon}_D$ . The lower branch represents the time-independent quasi-static (QS) stress response and consists of only one spring with modulus  $E_{st}$  [25]. The applied stress,  $\sigma_A$ , is the summation of viscous stress  $\sigma_r(t)$  component and QS stress ( $\sigma_{st}$ ) component, as shown in Equation 2-2 below [25]:

$$\sigma_A(t) = \sigma_r(t) + \sigma_{st} \quad \text{Equation 2-2}$$

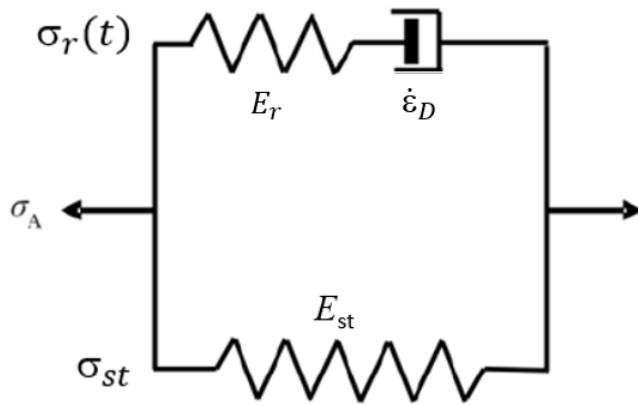


*Figure 2-13 Schematic diagram of the standard, viscoelastic model used for the analysis of MR test results*

The stress decay  $\Delta\sigma_r$  during the stress relaxation can be expressed using Equation 2-3 below:

$$\Delta\sigma_r = \sigma_r(0) - \sigma_r(t) = \sigma_A(0) - \sigma_A(t) \quad \text{Equation 2-3}$$

where  $t$  is the time measured from the beginning of each relaxation stage.

By adopting Eyring's law of viscosity [28-30], the stress response to deformation of the damper in the viscous branch is [26]:

$$\frac{\sigma_r}{\sigma_0} = \sinh^{-1}\left(\frac{\dot{\epsilon}_D}{\dot{\epsilon}_0}\right) \quad \text{Equation 2-4}$$

Where  $\sigma_r$  is the stress applied to the damper,  $\sigma_0$  and  $\dot{\epsilon}_0$  two parameters in Eyring law of viscosity,  $\dot{\epsilon}_0$  the reference strain rate and  $\sigma_0$  the reference stress [25].

The total strain in the viscous branch has two parts, one for elastic strain with modulus  $E_r$ , and another one for viscous deformation with Eyring parameters  $\sigma_0$  and  $\dot{\epsilon}_0$ , Therefore, the following equation can be obtained for stress relaxation at a constant total strain:

$$\dot{\epsilon}_0 \sinh(\sigma_r/\sigma_0) + \dot{\sigma}_r/E_r = 0 \quad \text{Equation 2-5}$$

With  $\sigma_0$  being constant, this expression can also be written as:

$$\frac{d}{dt} \left( \frac{\sigma_r}{\sigma_0} \right) = \left( -\frac{1}{\tau_r} \right) \sinh \left( \frac{\sigma_r}{\sigma_0} \right) \quad \text{Equation 2-6}$$

where  $\tau_r$  is the relaxation time, defined as:

$$\tau_r^{-1} = \dot{\epsilon}_0 E_r / \sigma_0 \quad \text{Equation 2-7}$$

Expression for the stress decay  $\Delta\sigma_r$  during the relaxation stage can then be derived [26], as given below:

$$\Delta\sigma_r = \sigma_r(0) - 2\sigma_0 \tanh^{-1} \left[ \tanh \left( \frac{\sigma_r(0)}{2\sigma_0} \right) \exp \left( -\frac{t}{\tau_r} \right) \right] \quad \text{Equation 2-8}$$

Equation 2-8 shows that the stress decay  $\Delta\sigma_r$  can be expressed as a function of time  $t$ . By curve fitting the experimental curves of  $\Delta\sigma_r$  vs.  $t$  from MR test using Equation 2-8, the values of parameter  $\sigma_r(0)$ ,  $\sigma_0$ , and  $\tau_r$  can be determined, and thus the  $\sigma_{st}$  value using Equation 2-2 at  $t = 0$ , where  $\sigma_A(0)$  and  $\sigma_r(0)$  are the applied stress and viscous stress at the beginning of the stress relaxation.

#### 2.4.2 Curving fitting of the relaxation behavior

Figure 2-14 presents an example of the best curve fitting based on Equation 2-8 for the stress drop vs. time from the MR test, at the stroke 1.54 mm. Time in Figure 2-14 (a) is in the linear scale while 2-14 (b) in the logarithmic scale. The curve fitting was focused on the time above 1000 seconds, since the curve of  $\Delta\sigma_r$  vs.  $t$  in the larger timeframe were used to determine  $\sigma_{st}$ . As a result, data for time less than 1000 seconds was ignored in the curve fitting.

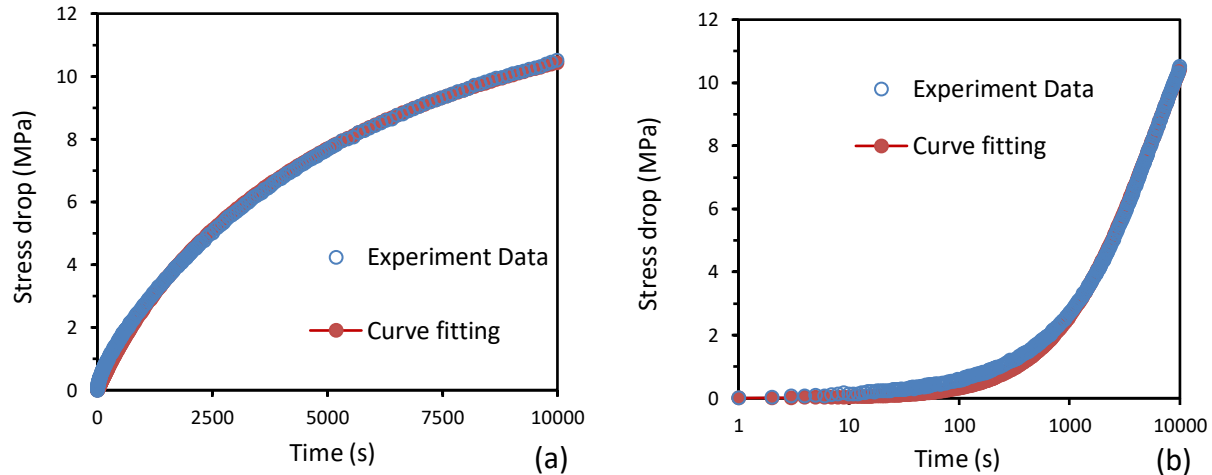


Figure 2-14 Example of stress drop occurring in the MR tests as a function of time at the relaxation stroke of 1.54mm and the best fitting curve generated based on Equation 2-8 using the following values for the fitting parameters:  $\sigma_0 = 6\text{MPa}$ ,  $\sigma_r(0) = 13.2\text{MPa}$ , and  $\tau_r = 8000\text{s}$ : (a) linear time scale and (b) logarithmic time scale.

Figure 2-15 shows how each fitting parameter affects shape of the fitting curve. The experimental data and best fitting curve, same as Figure 2-14, are presented in logarithmic scale. If  $\sigma_0$  is changed from 6MPa to 5MPa, as shown in the green curve, the curve becomes flatter, especially in the time range from 500 to 4000s. If  $\sigma_r(0)$  is changed from 13.2 MPa to 12.2 MPa, as shown in the black curve, the whole curve would move downwards. If  $\tau_r$  is decreased from 8000s to 5500s, as shown in the orange curve, the curve in the larger time range, especially for the time greater than 4000s, is affected. In general,  $\sigma_0$  is mainly to control the slope of the curve,  $\sigma_r(0)$  the absolute level of the curve and  $\tau_r$  the trend of the curve in the longer time range. Combination of the effects from these three fitting parameters would help find the best fitting curve for the given experimental curve from the MR test.



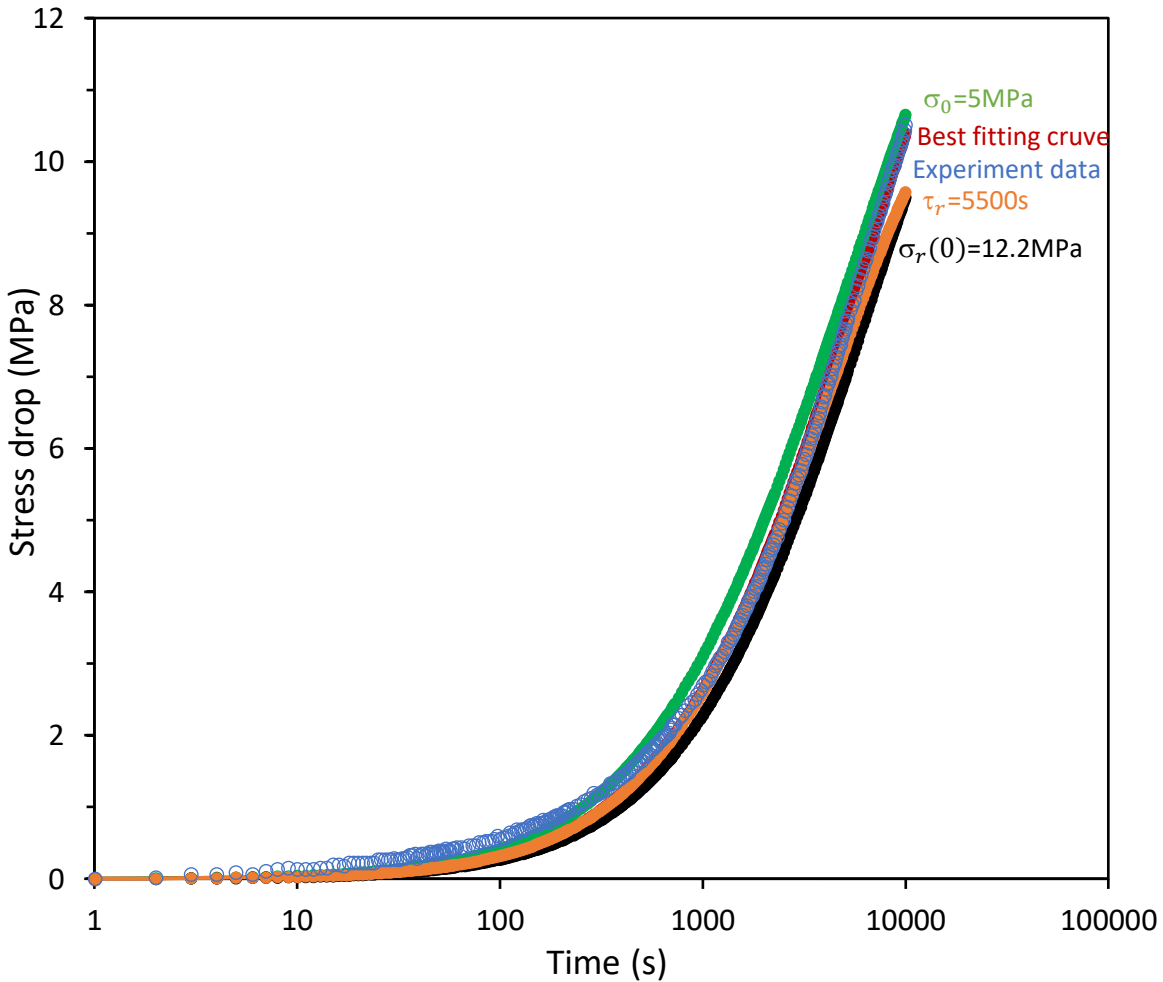


Figure 2-15 Experimental data (in blue, same as in Figure 2-14) and the best fitting curve (in red,  $\sigma_0 = 6\text{MPa}$ ,  $\sigma_r(0)=13.2\text{MPa}$ , and  $\tau_r = 8000\text{s}$ ); the rest of the curves are generated based on the following changes of fitting parameters using equation (8):  $\sigma_0 = 5\text{MPa}$  (in green),  $\sigma_r(0)=12.2\text{MPa}$  (in black), or  $\tau_r = 5500\text{s}$  (in orange).

Figure 2-16 shows three fitting examples using Equation 2-8 for  $\Delta\sigma_r$  vs.  $t$  obtained from the MR test. Figure 2-16 (a) is for the stroke of 0.1mm, which is at the beginning of the test. Due to the resolution of the data acquisition system, the load resolution is not sufficient to detect the small stress drop at this stroke. Therefore, the experimental data do not form a continuous curve. As a result, data point at the shortest time among the data points of the same stress drop was chosen for the curve fitting. This criterion is applied to all MR tests results at small strokes.

Figure 2-16 (b) is for the stroke at 1.1mm, which is around the yield point based on the applied engineering stress. Since the trend of change of the experimental curve at a large time scale is sharply increased, a larger  $\tau_r$  value of 12000s was needed to fit the curve. In this case, it was found that only the time frame greater than 1000s could be well fitted, based on which values for  $\sigma_r(0)$  and  $\sigma_0$  were determined. Figure 2-16 (c) is for the stroke of 2.1mm, in which the applied engineering stress reached the plateau region. Since the trend of change of the experimental curve at the large time scale (greater than 6000s) is different from the one shown in Figure 2-16 (b), a smaller  $\tau_r$  value of 5500s was needed to fit the curve.

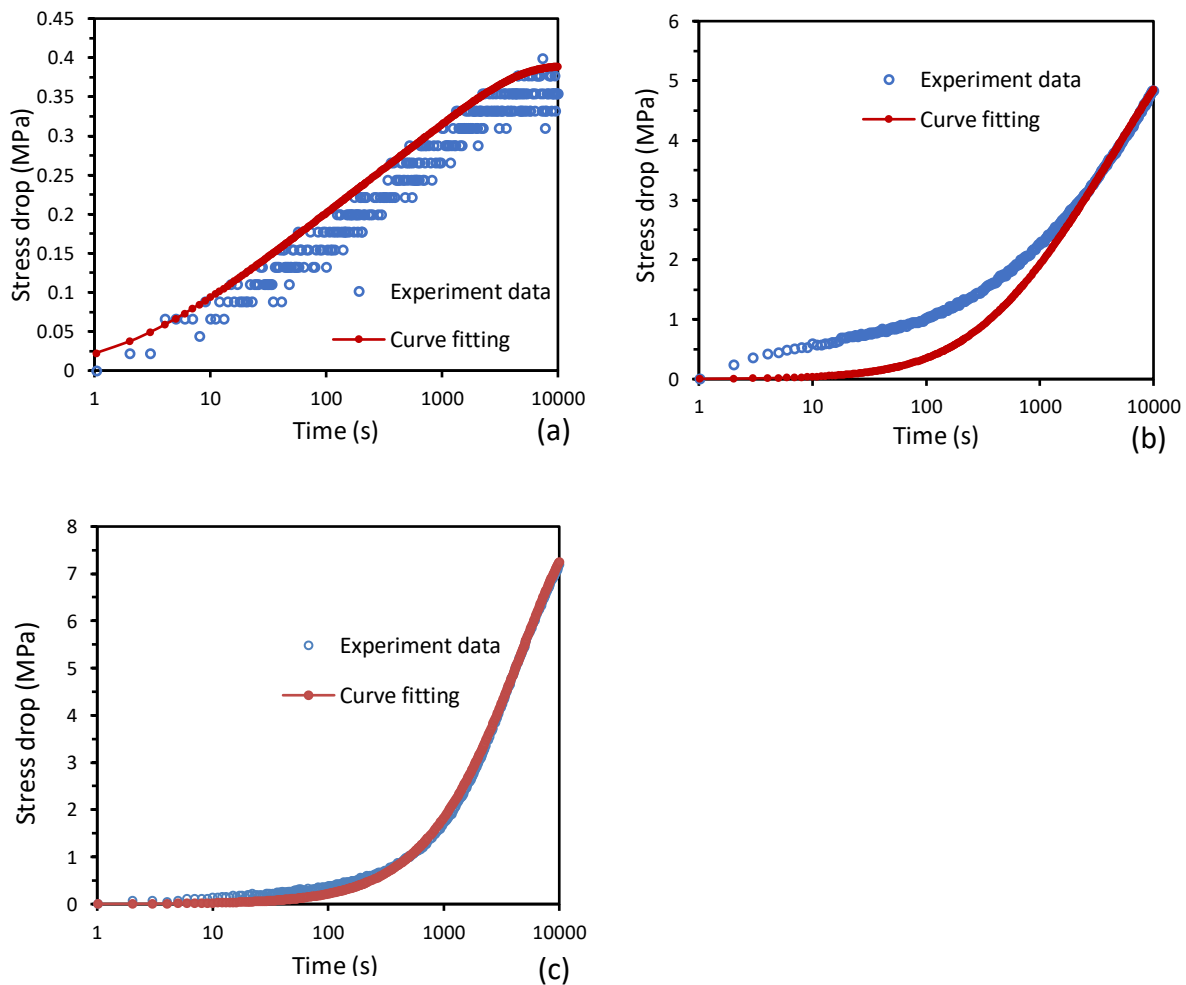


Figure 2-16 Examples of stress drop occurred in the MR tests as a function of time at certain strokes in the logarithmic scale and the best fitting curve generated based on Equation 2-8 using the following values for the fitting parameters, (a) stroke=0.1mm,  $\sigma_0 = 0.05\text{MPa}$ ,

$\sigma_r(0)=0.39MPa$ , and  $\tau_r = 2200s$ , (b) *stroke*=1.1mm,  $\sigma_0 = 1.5MPa$ ,  $\sigma_r(0)=6.2MPa$ , and  $\tau_r = 12000s$ , (c) *stroke*=2.1mm,  $\sigma_0 = 5.4MPa$ ,  $\sigma_r(0)=8.4MPa$ , and  $\tau_r = 5500s$

## 2.5 Determining the best test condition to be used for characterizing PETG specimens

After finalizing the approach for analyzing MR test results, fitting parameters  $\sigma_0$ ,  $\sigma_r(0)$ , and  $\tau_r$ , QS stress ( $\sigma_{st}$ ) can then be plotted as functions of stroke. MR tests were conducted on four types of PETG specimens, i.e., conventionally extruded, and 3D printed  $[0^\circ]$ ,  $[\pm 30^\circ]_s$  and  $[\pm 45^\circ]_s$  specimens. Three combinations of specimen types and gripping methods were used, i.e., specimens with holes using either gripping method one or gripping method two, and specimens without holes using gripping method one. For each combination, at least two duplicate tests were conducted to ensure repeatability of the test results, since the results from two duplicate tests are very similar. For the convenience of comparison, only one of the two duplicate test results will be shown in this section. The best combinations were used for the comparison and the analysis. Below is the summary of MR test results for each type of PETG specimens under three different combinations.

### 2.5.1 Extruded PETG specimens

Figure 2-17 (a) shows the  $\sigma_{st}$  vs. stroke for different combinations of specimen type and gripping method in which specimens without holes using gripping method one showed the highest stiffness before it reached the yield point, and specimens with holes had higher stiffness using gripping method than using gripping method two. The latter is expected as the gripping method two provided a relatively long effective gauge length. Specimen without holes using gripping method one reached the yield point at about 0.8mm, specimens with holes using gripping method one at about 1.2mm, and specimens with holes using gripping method two at about 1.5mm.

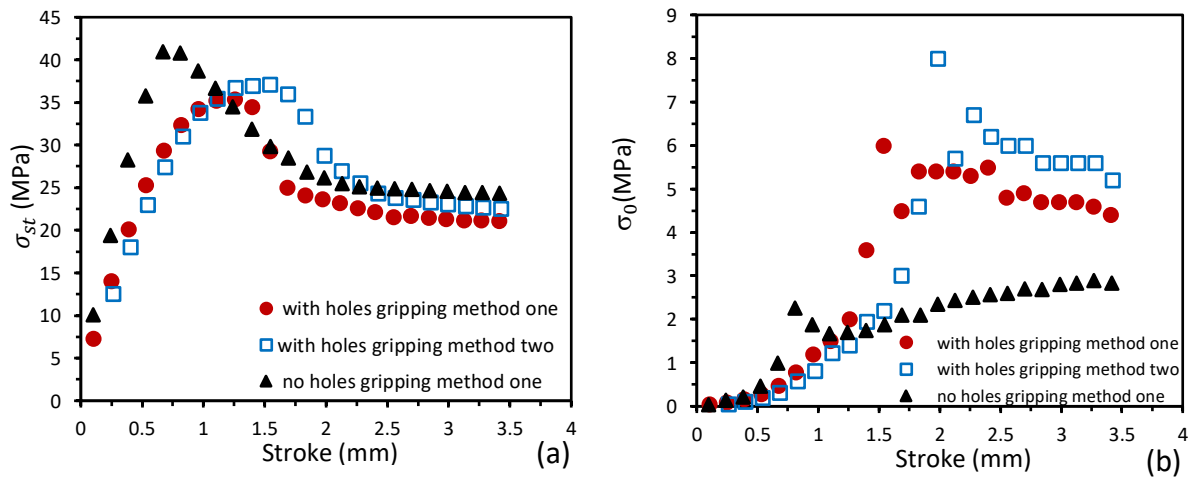
It is worth pointing out that the stroke distance from the yield point to the end of the post-yield sharp decrease is 1mm for specimens without holes, 0.5mm for specimen with holes using gripping method one, and 0.5mm for specimen with holes using gripping method two. This suggests that specimens with holes have a relative short stroke range for neck development and thus reach the plateau region relatively fast, compared to specimens without holes.

Figure 2-17 (b) shows  $\sigma_0$  vs. stroke for all the above combinations. The curve reaches the maximum  $\sigma_0$  value at the stroke of 0.8mm for specimens without holes using gripping method one, and 1.5mm for specimens with holes using gripping method one and 2mm using gripping method two. This suggests that the order of stroke difference for the maximum  $\sigma_0$  is same as that for QS

yield stress. Also, it is noted that after the maximum point, specimens with holes have significantly larger maximum  $\sigma_0$  value than specimen without holes, possibly caused by the presence of the holes.

Figure 2-17 (c) shows variation of  $\sigma_r(0)$  vs. stroke in different test conditions. The maximum  $\sigma_r(0)$  values occur at about the same stroke for all curves, around 1.7mm, but for specimens without holes the  $\sigma_r(0)$  value increased faster than specimens with holes, as shown in the figure, in the stroke range from 0.7 to 1.7mm. The  $\sigma_r(0)$  value at the post-yield plateau region is the highest for specimens without holes, and about the same level for specimens with holes using the two gripping methods.

Figure 2-17 (d) shows  $\tau_r$  vs. stroke for different combinations of specimen types and gripping methods. Three to four  $\tau_r$  values were used for covering the whole stroke range covered in the MR test. Since  $\tau_r$  is the least sensitive parameter for the curve fitting, it was not possible to determine the exact  $\tau_r$  value for its variation with the increase of stroke. Nevertheless, change of the  $\tau_r$  values are still an indication of the difference in the specimen state during the MR test. Note that in general, a small  $\tau_r$  value of 2000s was used only at the first relaxation stage. The largest  $\tau_r$  value, 12000s was used in the stroke range from the second relaxation stage till the beginning of plateau regions of the stress. During the plateau region,  $\tau_r$  values decreased to either 6500s or 5500s depending on the curve fitting requirement.



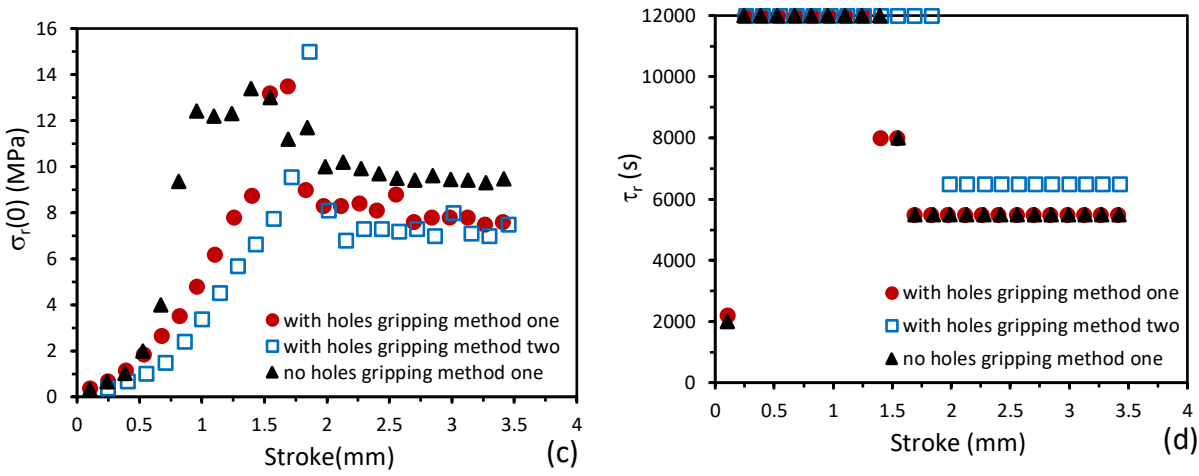


Figure 2-17 Comparison of parameters analyzed from the MR test results for an extruded specimen: (a)  $\sigma_{st}$ , (b)  $\sigma_0$ , (c)  $\sigma_r(0)$ , and (d)  $\tau_r$

In conclusion, the four graphs in Figure 2-17 suggest that specimens with holes have lower stiffness than specimens without holes, but the former require a shorter stroke to initiate the necking, possibly because of the stress concentration introduced by the presence of the holes. Also, curves for specimens without holes reach their maximum points at the shortest stroke, while for curves for specimens with holes, gripping method two generated their maximum points at a longer stroke. All those three test conditions can give the desired results. Although three types of test conditions are suitable for the extruded PETG specimens, the results suggest that gripping method two does not have any obvious advantage over gripping method one. This finding is further investigated using 3D printed PETG specimens.

### 2.5.2 [0°] specimens

Figure 2-18 presents the typical post-tested [0°] 3D printed PETG specimens, in the three combinations of specimen types and gripping methods. Figures 2-18 (a) and (b) are specimens with holes, using gripping methods one and two, respectively, which show that fracture was initiated from the holes. For specimen without holes, Figure 2-18 (c), fracture was not generated at the end of the test, at the stroke of 3.5mm, and the deformation was confined to the gauge section.

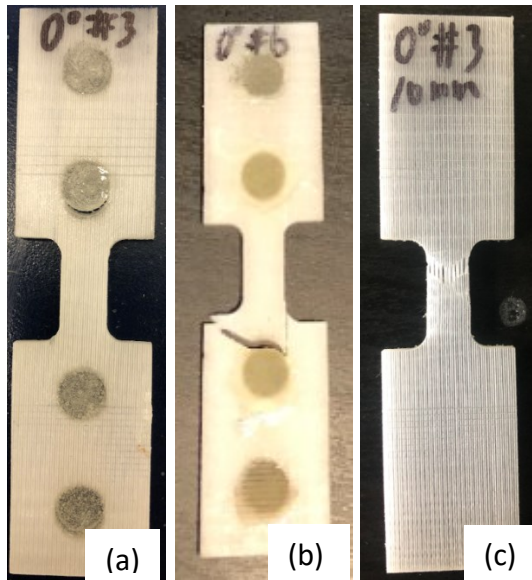


Figure 2-18 [0°] 3D printed PETG specimens after MR tests (a) with holes using gripping method one, (b) with holes using gripping method two, (c) no holes using gripping method one.

Figure 2-19 summarizes the typical MR test results for [0°] PETG specimens, as a function of stroke for different combinations of specimen type and gripping method. Specimens with holes using gripping method one only lasted three relaxation stages before fracture but using gripping method two the specimen lasted for six relaxation stages and fractured during the seventh relaxation stage. On the other hand, specimens without holes survived till the end of the test, as indicated in Figure 2-19. Figure 2-19 (a) indicates that curves for specimens without holes are stiffer than the specimens with holes. The curve for specimen without holes using gripping method one reached the maximum stress at the stroke of about 0.8mm. However, the maximum stress for the specimens with holes cannot be determined, as fracture was initiated before the peak could be reached. Figures 2-19 (b) and (c) shows that  $\sigma_0$  and  $\sigma_r(0)$  values are higher for specimens with holes than those without holes, but again yield points in the curves for specimens with holes were not reached. Figure 2-19 (d) shows  $\tau_r$  values used for [0°] specimens, which do not show much sensitivity to the specimen type or gripping method.

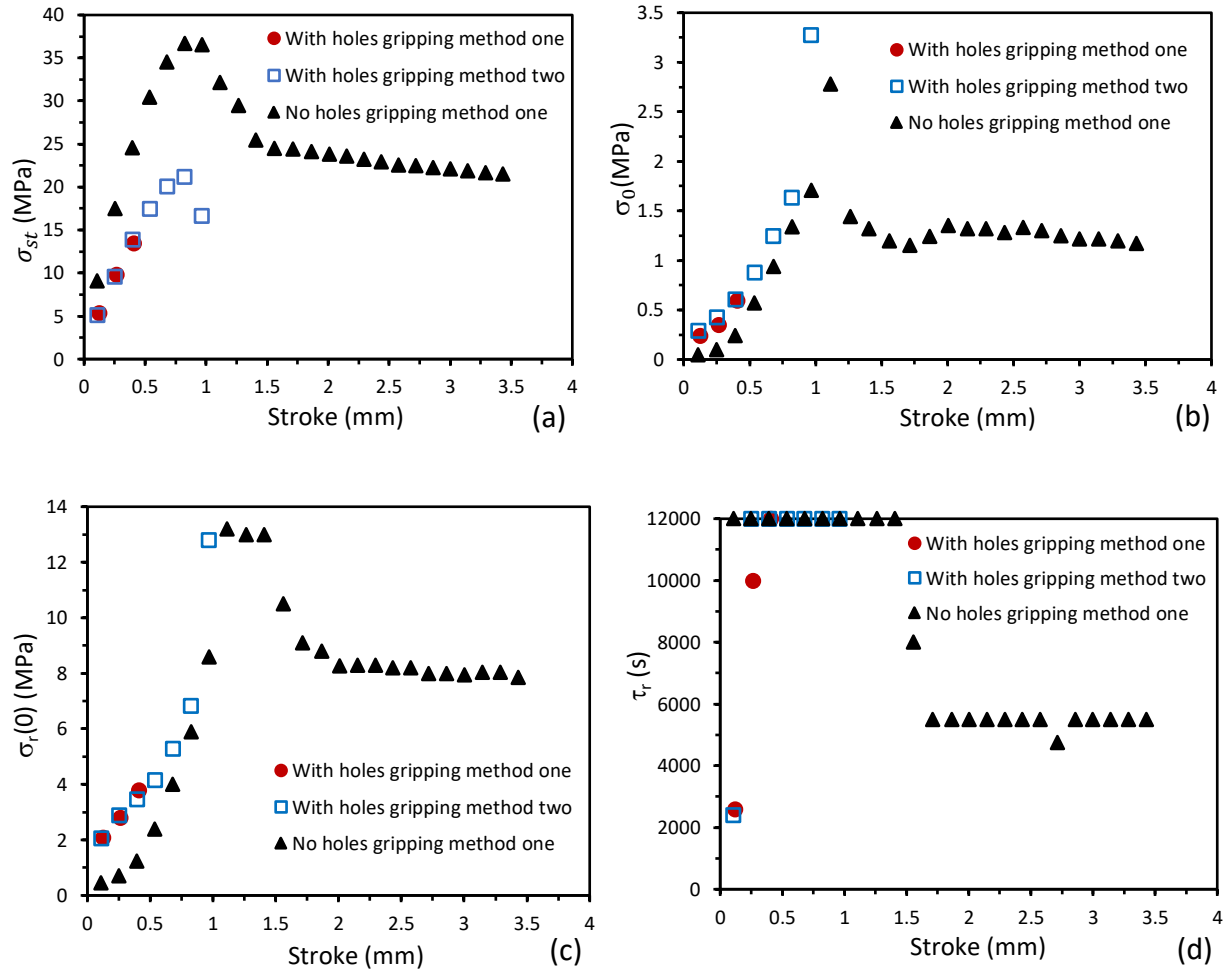


Figure 2-19 Comparison of parameters analyzed from the MR test results for a  $[0^\circ]$  specimen: (a)  $\sigma_{st}$ , (b)  $\sigma_0$ , (c)  $\sigma_r(0)$ , and (d)  $\tau_r$

The results in Figure 2-19 suggest that introducing holes to  $[0^\circ]$  specimens have made the area around holes susceptible to crack initiation and using gripping method two has increased specimen compliance. Therefore, the specimen without holes using gripping method one seems to be the best choice for the  $[0^\circ]$  specimen.

### 2.5.3 $[\pm 30^\circ]_s$ specimens

Figure 2-20 presents typical  $[\pm 30^\circ]_s$  3D printed PETG specimens after MR results using three different combinations of specimen types and gripping methods Figure 2-20 (a) and (b) are for specimens with holes, where the fracture locations are around the holes and the edges at the end of the gauge section, but for specimens without holes, as shown in Figure 2-20 (c), the fracture location is within the gauge section.

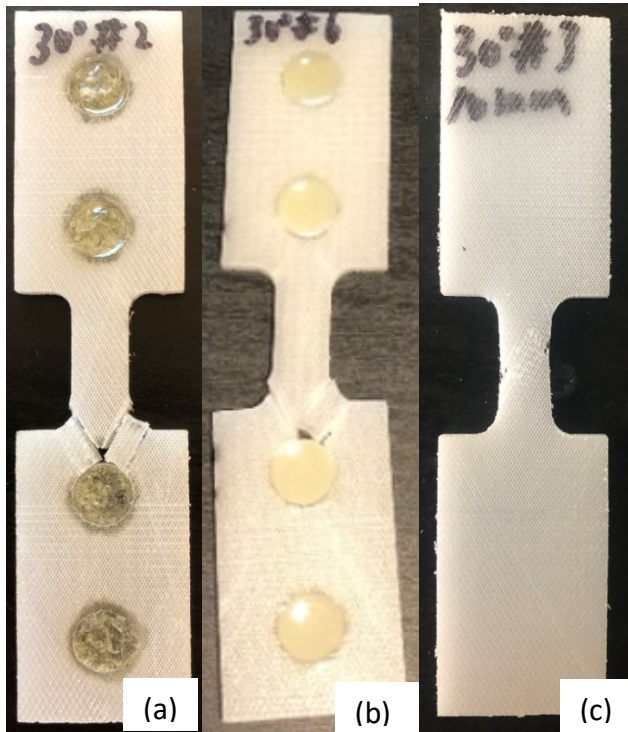


Figure 2-20  $[\pm 30^\circ]_s$  3D printed PETG specimens after MR tests (a) with holes using gripping method one, (b) with holes using gripping method two, (c) no holes using gripping method one

Figure 2-21 shows parameters from the analysis of MR test results for  $[\pm 30^\circ]_s$  specimens. Figure 2-21 (a) shows that curves for specimens under all three combinations reached their yield points, where the curve for the specimen without holes showed the highest stiffness and stroke for the yield point is 0.75mm, while the curve for specimen with holes using gripping method one shows a sudden decrease right after the yield point which led to fracture. The curve for the specimen with holes using gripping method two, on the other hand, decreases slowly after the yield point with fracture occurring at a stroke larger than that for the specimen without holes.

Figures 2-21 (b) and (c) summarize curves for specimens with holes using either gripping methods one or two and for a specimen without holes using gripping method one, all of which show a clear trend of increase at first and then remain relatively steady after their yield points. The curves for a specimen with holes using the gripping method one show some trend changes after the yield point, possibly due to the early initiation of fracture around the hole. Figure 2-21 (d) shows  $\tau_r$  which has values of 12000s and 8000s for all specimens, other than the  $\tau_r$  values for the first relaxation stage and before the fracture. That is, a smaller  $\tau_r$  value (5000s-6000s) is needed for the first relaxation



stage for specimens with holes. For the specimen with holes and using gripping method one,  $\tau_r$  for the last two relaxation stages before fracture was 5500s. This was possibly caused by the fracture onset of the specimen.

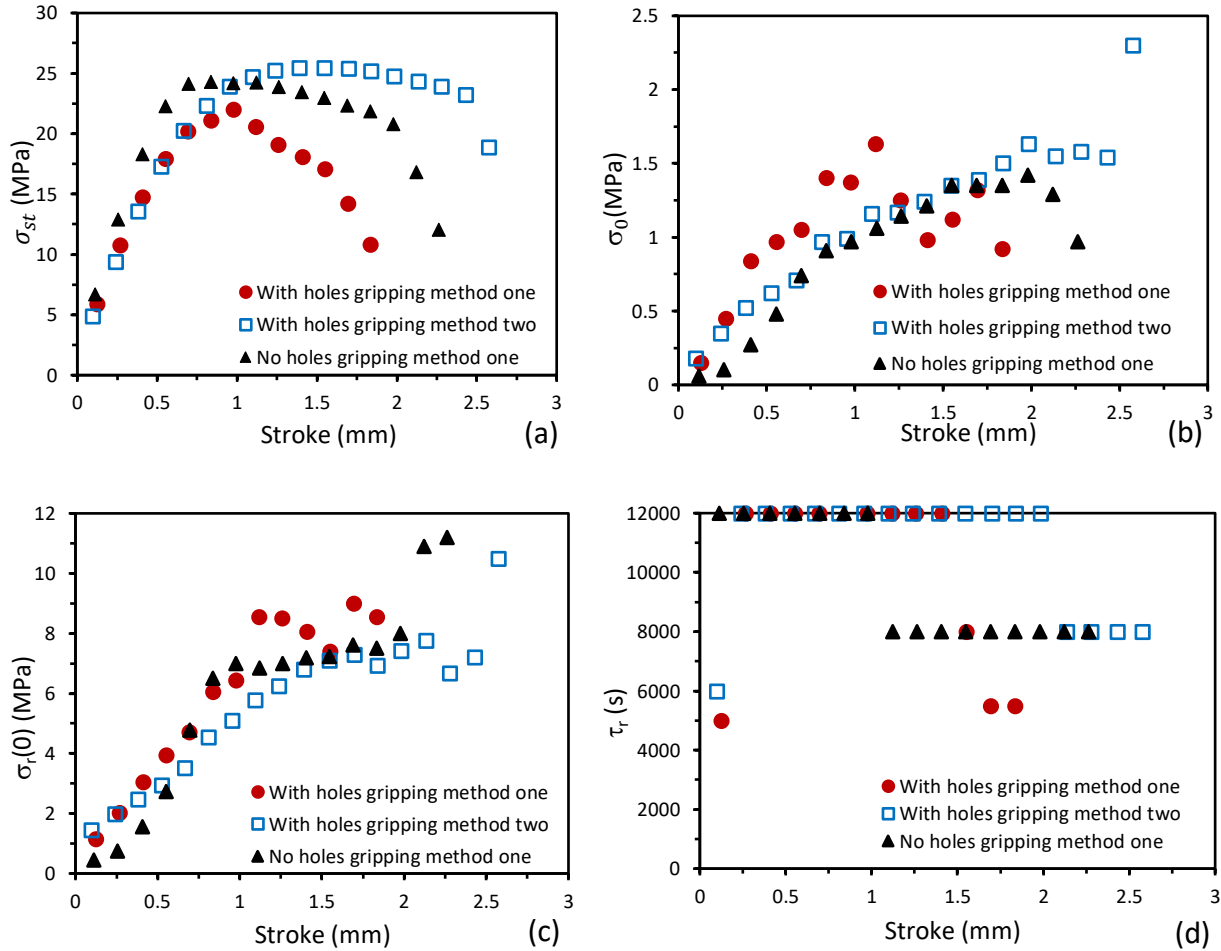
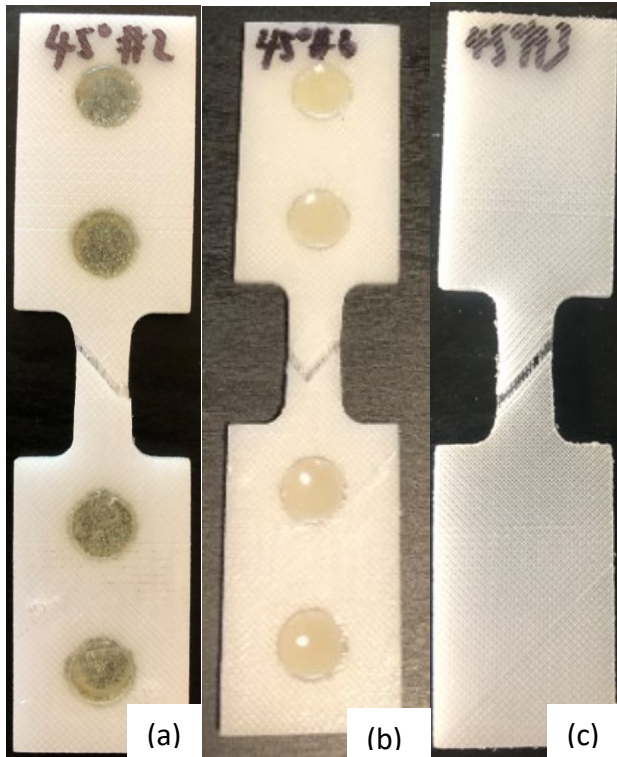


Figure 2-21 Comparison of parameters analyzed from the MR test results for  $[\pm 30^\circ]_s$  3D printed specimen, plotted as a function of stroke: (a)  $\sigma_{st}$ , (b)  $\sigma_0$ , (c)  $\sigma_r(0)$ , and (d)  $\tau_r$

The above comparison suggests that specimens with holes using gripping method two and specimens without holes using gripping method one could have a few more stages after the yield point than the specimens with holes using gripping method one. But the specimens with holes using gripping method two showed fracture at a location nearby the holes. Therefore, the specimen without holes using gripping method one should be the best combination for testing of  $[\pm 30^\circ]_s$  PETG specimens.

#### 2.5.4 $[\pm 45^\circ]_s$ specimens

Figure 2-22 presents typical post-test  $[\pm 45^\circ]_s$  3D printed PETG specimens after MR tests under three different combinations of specimen types and gripping methods. All fracture locations are within their gauge sections.



*Figure 2-22  $[\pm 45^\circ]_s$  3D printed PETG specimens after MR tests (a) with holes using gripping method one, (b) with holes using gripping method two, (c) no holes using gripping method one.*

Figure 2-23 shows MR test parameters for  $[\pm 45^\circ]_s$  PETG specimens. Figure 2-23 (a) indicates that the curve for specimens without holes reached the maximum point at the smallest stroke, and its maximum QS stress is much lower than those for specimens with holes. The former curve also shows a plateau region before the fracture, while the latter two curves, for specimens with holes, decreased continuously after their yield points till the onset of fracture. With holes and without holes specimens have different trends of  $\sigma_0$  curves and  $\sigma_r(0)$  curves after the stroke of 1.6mm until they are totally fractured: Figure 2-23 (b) indicates that the  $\sigma_0$  curves for with holes specimens are continuously decreased and the curve for without hole specimen is reached the plateau, Figure 2-23 (c) shows that the  $\sigma_r(0)$  curve for without hole specimen is reached the plateau but the curves for with holes specimens are scattering. Figure 2-23 (d) shows that at the

first relaxation stage, small  $\tau_r$  values is needed for the curve fitting. For the rest of the relaxation stages, on the other hand, three  $\tau_r$  values of, 12000s, 8000s and 5500s are sufficient to cover all MR test results. Note that  $\tau_r$  with 12000s was used for the regions around the yielding, which changed to 8000s followed by 5500s after the yielding.

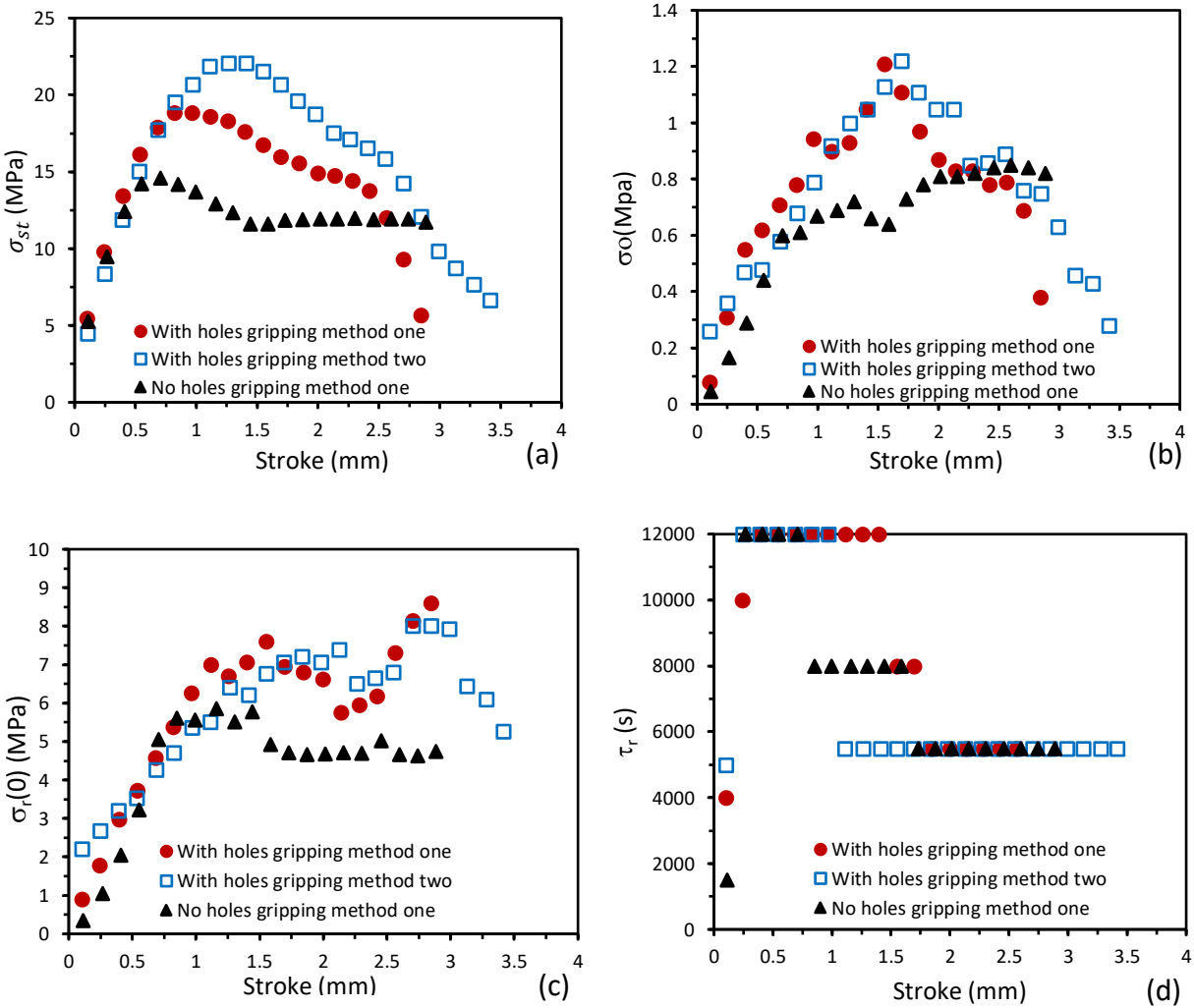


Figure 2-23 Comparison of analyzed MR test parameters vs. stroke for  $[\pm 45^\circ]_s$  3D printed specimens with different combinations of specimen types and gripping methods, (a)  $\sigma_{st}$ , (b)  $\sigma_o$ , (c)  $\sigma_r(0)$ , (d)  $\tau_r$

The above results suggest that all three combinations of specimen types and gripping methods can be used to characterize  $[\pm 45^\circ]_s$  specimens, since they all fractured after a stroke of at least 3 mm and their fracture locations were all in the gauge section. However, since specimens without holes are the best choice for  $[0^\circ]$  and  $[\pm 30^\circ]_s$  specimens, and for both extruded and  $[\pm 45^\circ]_s$  specimens

using specimens with holes do not provide additional information, MR test results from specimens without holes, using gripping method one, is chosen to compare relaxation behaviours among different types of PETG specimens, as to be shown in the next chapter.

## 2.6 Methods used to obtain QS elastic modulus

In this study, the QS elastic modulus for all types of PETG specimens were determined from the experimental results, as summarized below.

### 2.6.1 Using MR test to obtain the QS stress-stroke relationship for PETG specimens

The QS stress-stroke relationship during the initial loading stage (stroke less than 0.1mm) were determined for extruded,  $[0^\circ]$ ,  $[\pm 30^\circ]_s$ , and  $[\pm 45^\circ]_s$  specimens from the MR test results. For 3D printed  $[90^\circ]$  specimens, both monotonic and MR tests were conducted using gripping method one, on specimens with holes, with the same testing parameters and procedures as other PETG specimens.

### 2.6.2 Monotonic tensile test

This testing method was used only for 3D printed  $[90^\circ]$  specimens to obtain the force-elongation relationship. Monotonic tensile test was conducted using the same universal test machine as MR test (Qualitest Quasar 100, Lauderdale, FL, USA) and at the same crosshead speed of 5mm/min. Each test was stopped either after the stroke of 3mm or when the specimen was fractured, whichever happened first. Load, time, and stroke were recorded for the whole test. Thickness and width for the gauge section were measured for each specimen before the test. Engineering stress was calculated based on the recorded load and the original cross-sectional area using Equation 2-1.

### 2.6.3 Finite element simulation of QS stress-stroke curve to calculate the QS elastic modulus

Finite element (FE) modelling to simulate the QS stress-elongation relationship for the stroke range of less than 0.1mm, was used to determine the QS elastic modulus of the specimens. The FE model was built based on the nominal dimensions of the dog-bone specimen in ABAQUS, due to the geometric symmetry of the specimens, length, width, and thickness of the FE model were half of their values for the specimen. Therefore, as shown in Figure 2-24 (a), a 3D dog-bone model with size 1/8 of the specimen was developed, using 8-node linear brick (C3D8) with 35,000 nodes and 29,000 elements. The simulation is based on the plane-stress condition and in the displacement

control, so that variables  $F_2$  (force in the y direction) and  $U_2$  (displacement in the y direction) could be output from the FE model. The gripping region, as shown by the blue area in Figure 2-24 (b), is 10mm above the edge of the gauge section.

Using the FE model with the simulated gripping conditions, QS elastic modulus E for the specimen was determined so the experimental QS stress-stroke curve could be regenerated using the FE model.

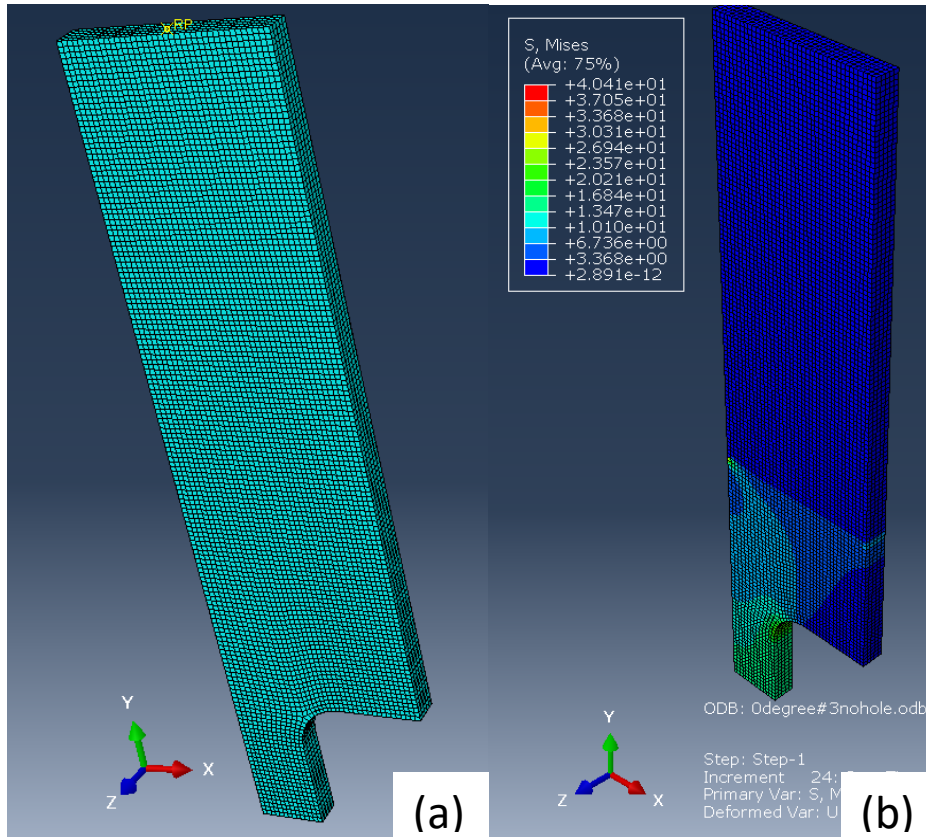
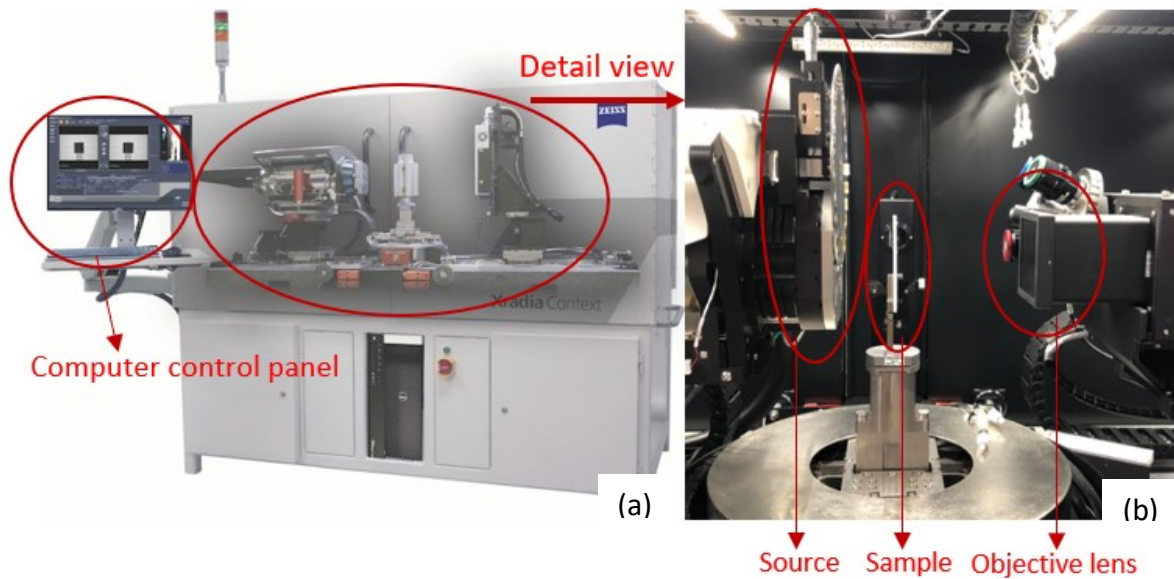


Figure 2-24 (a) The meshed model for FE simulation, and (b) a typical contour plot after small deformation

## 2.7 Measurement of volume ratio for 3D printed specimens

Many researchers have investigated void content and distribution in 3D printed samples. Among the studies, X-ray computed tomography (XCT) is the most common and effective technique [27] [31-32], which has been widely used as a non-destructive method to characterize features that are initiated internally in the samples, including void distribution, size, density, and shape. In this study, XCT has helped determine the voids and PETG filament distribution, as well as their volumetric percentages in the specimens.

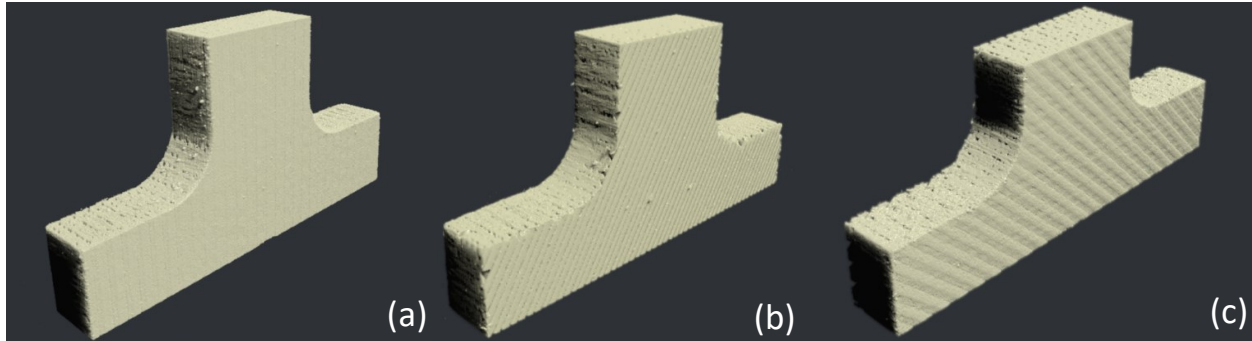
The XCT equipment used in this study was Zeiss Xradia Versa 620 X-Ray Microscope, as shown in Figure 2-25 (a). The equipment contains two parts. One is the computer control panel for setting up the parameters, including the set-up of the scanning area, field mode, voltage, and power of the source. The other part is the X-ray microscope, controlled by the computer panel, with the detailed view shown in Figure 2-25 (b) in which the left side is the X-ray beam source, with the sample in the middle, the objective lens on the right side, and the detector at the back.



*Figure 2-25 Zeiss ZEISS Xradia Versa 620 X-Ray Microscope used to scan 3D printed specimens, (a), whole X-ray Microscope, (b), detail view*

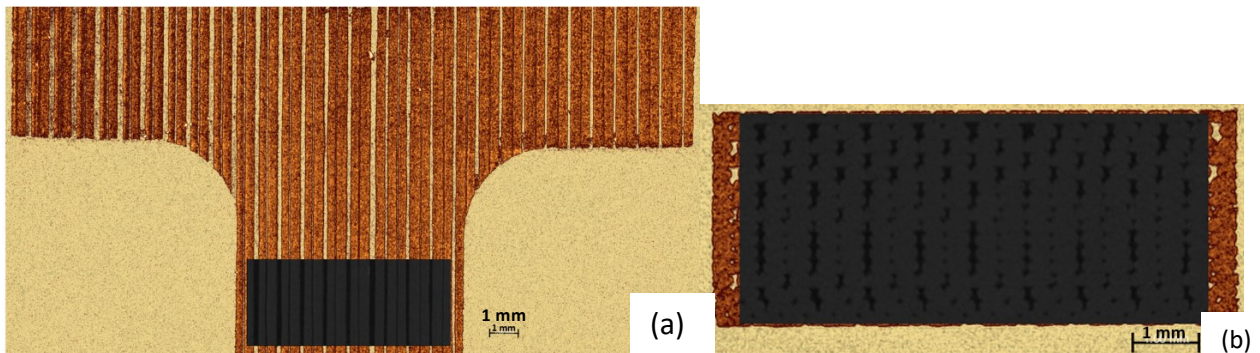
Results from XCT were processed using a software named Dragonfly [33], for image process and analysis. Figure 2-26 shows the reconstructed images using Dragonfly for  $[0^\circ]$ ,  $[\pm 30^\circ]$ , and  $[\pm 45^\circ]$ , 3D printed specimens. Note that the  $[90^\circ]$  specimen was not scanned since it should

have very similar filament volume ratio for the  $[0^\circ]$  specimen. The scanned region was chosen to be part of the original sample, as further increase of the scanned region could cause decrease of the image resolution. In this study, half of the area in the gauge section was scanned for each sample to obtain enough information to characterize the void and the filament distribution in the sample, with the resolution of  $20\mu\text{m}/\text{pixel}$  which is sufficient to detect any meaningful voids in the scanned regions.



*Figure 2-26 3D scanned area of the 3D printed specimens (a)  $[0^\circ]$ , (b)  $[\pm 30^\circ]_s$  and (c)  $[\pm 45^\circ]_s$*

Figure 2-27 (a) shows the front view of the scanned region for  $[0^\circ]$  3D printed sample, the volume ratio of filament to voids in the blackened region was determined. Figure 2-27 (b) shows the sectional view of the blackened region. As a result, the blackened region was extracted as a rectangular box from the original scanned region, as shown in Figure 2-27 (c).



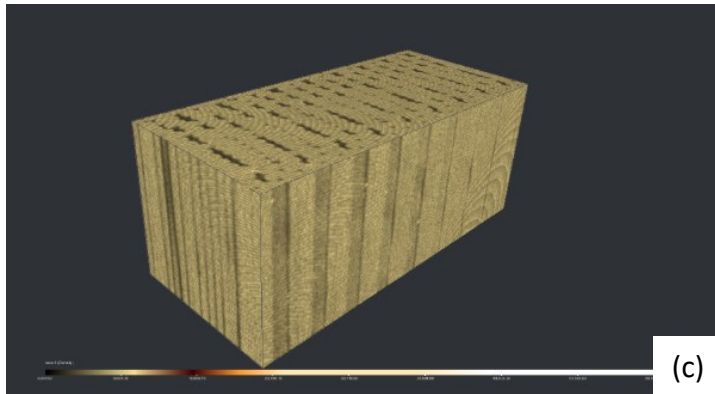


*Figure 2-27 Determining the volume fractions of filament and voids in the selected region using Dragonfly: (a) Front view, (b) Sectional view of the blacked region in (a), and (c) 3D view of blackened region in (a)*

After the box shown in Figure 2-27 (c) was extracted with known dimensions, a function in Dragonfly software, known as segmentation, is used, to allow users to reconstruct different models for the regions of interests. Volume for the reconstructed models and the corresponding filament and void volume fractions, with respect to the total volume of the box, could then be determined. As shown in Figures 2-28 (a) and (b), which are two examples of the reconstructed models for PETG filament and voids, respectively, in the region of interests. Figure 2-28 (c) is the combined view the reconstructed model that contains segmented PETG filaments and voids.

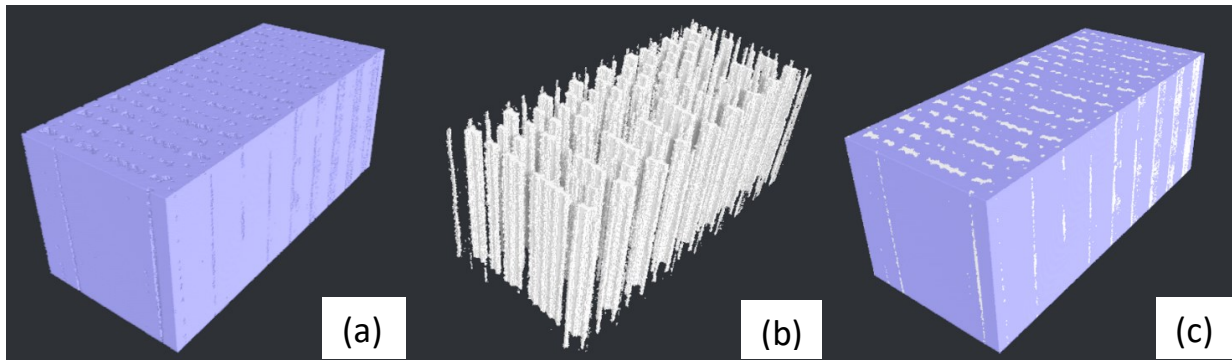


*Figure 2-28 Reconstructed 3D model after segmentation: (a) reconstructed 3D model for segmented filament only, (b) reconstructed 3D model for segmented voids only and (c) reconstructed 3D model including segmented filament and voids.*



## Chapter 3 Characterization of mechanical behaviour of extruded and 3D printed PETG specimens

This chapter focus on the analysis of the MR test results for different types of PETG specimens. The first section demonstrates the MR test and monotonic tensile test results for [90°] specimens which will be used to determine the QS stress-stroke relationship for the [90°] specimen. The rest of the chapter is focused on the use of specimens without holes and gripping method one, as described in chapter 2, to characterize different types of PETG specimens using MR tests. The discussion includes comparison of the analyzed MR tests results between conventional extruded and 3D printed [0°] PETG specimens, and comparison of the analyzed MR test results among three types of 3D printed specimens with different raster angle configurations. The last section is focused on the analysis of curves for QS stress, applied stress and fitting parameters ( $\sigma_0$ ,  $\sigma_r(0)$  and  $\tau_r$ ) as a function of stroke, to examine the relationship among those curves for the same type of specimens and the relationship of these curves among different types of specimens.

### 3.1 Test results for [90°] 3D printed specimens

Test results used to find the QS stress-stroke relationship during the small stroke deformation (stroke less than 0.1mm) are demonstrated below.

#### 3.1.1 MR test results

The MR test was conducted for [90°] specimens to obtain the QS elastic modulus. Below are the summary of the analyzed MR test results.

Figure 3-1 (a) is the total applied stress at the onset of each relaxation stage and QS stress, for 3 and 2 stages, respectively. At the first relaxation stage, the applied stress and QS stress are close to each other, suggesting that only a little stress drop occurred during the relaxation. But the difference increased dramatically at the second relaxation stage, and the specimen fractured during the third relaxation stage. As a result, there are only two points for the plots of fitting parameters as a function of stroke. Figures 3-1 (b), (c) and (d) show the relaxation fitting parameters  $\sigma_r(0)$ ,  $\sigma_0$  and  $\tau_r$  as a function of stroke. Since very limited information could be obtained from the [90°] 3D printed specimen and fracture occurred at a small stroke (about 0.4 mm), results for the [90°] specimens are not included in the analysis and discussion in the rest of this chapter.

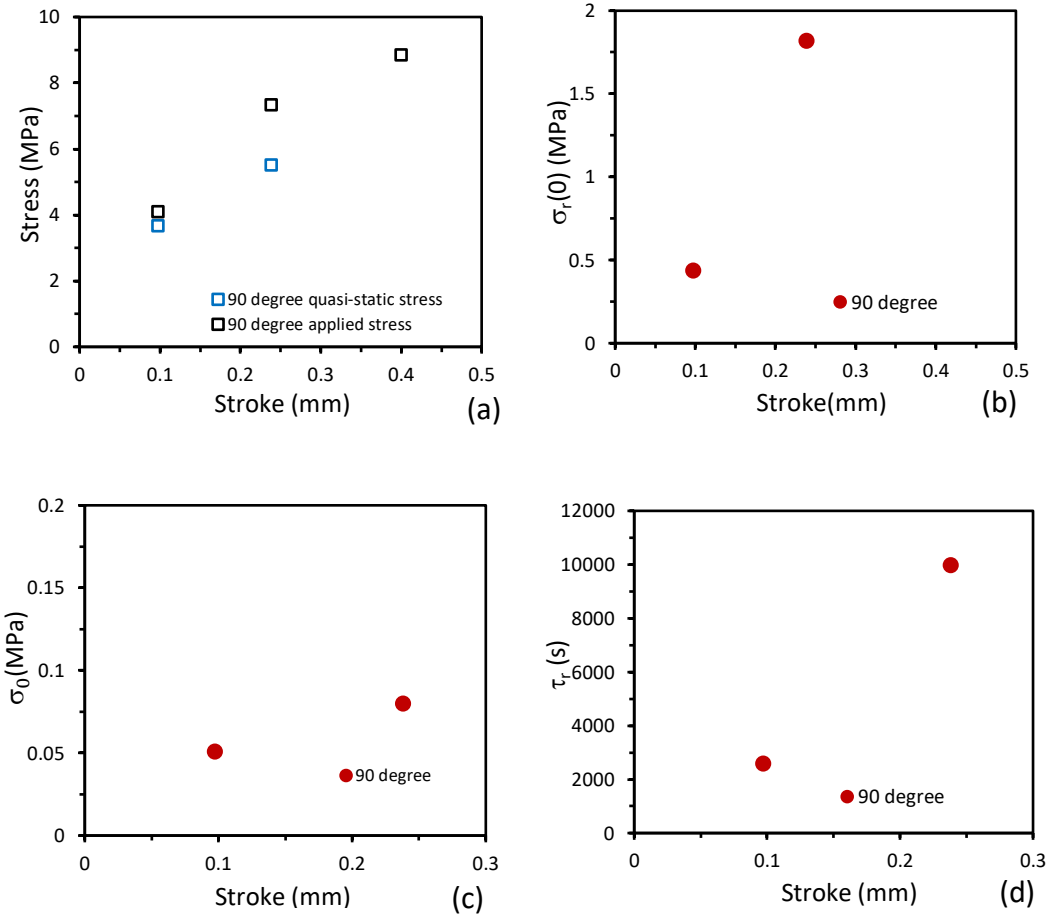


Figure 3-1 MR test results for a [90°] specimen: (a) QS stress and applied stress, (b)  $\sigma_0$ , (c)  $\sigma_T(0)$ , and (d)  $\tau_r$

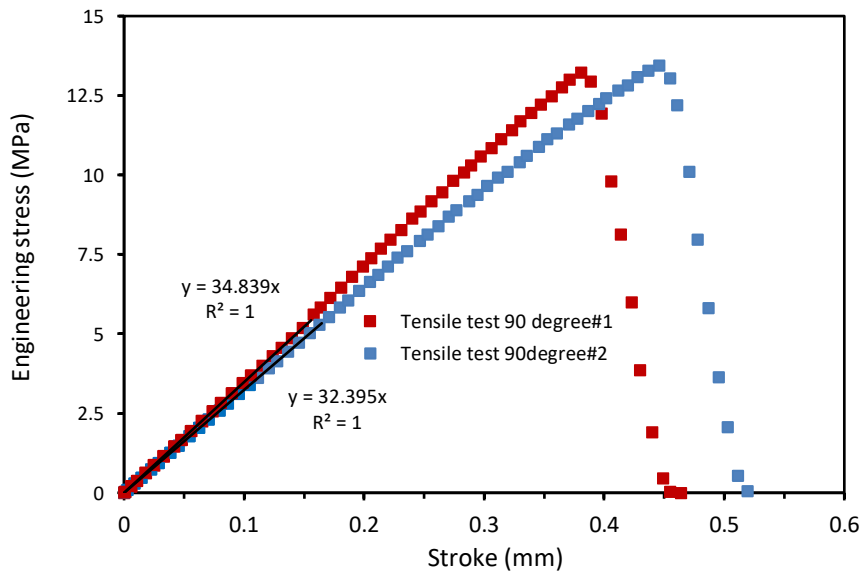
Figure 3-2 shows the [90°] 3D printed specimen after the MR test. The fracture was caused by debonding between the filaments in the gauge section, with little influence by the presence of the holes. In view that limited information can be obtained from the [90°] 3D printed specimens, no more MR tests were conducted on [90°] specimens. Instead, monotonic tensile test was used to obtain the force-elongation relationship for the [90°] specimen, for determining the QS elastic modulus.



Figure 3-2 [90°] 3D printed PETG specimen with holes after MR tests using gripping method one

### 3.1.2 Monotonic tensile test results

Two sets of monotonic tensile test results are shown in Figure 3-2. The specimens were fractured at strokes of 0.38 mm and 0.44 mm, respectively. The two curves start showing some difference at the stroke of around 0.11mm. However, the initial slopes are very close, as shown in the Figure 3-2, with the slope values of 34.8 and 32.4 MPa/mm, respectively.



*Figure 3-3 Engineering stress vs. stroke for [90°] 3D printed specimens from monotonic tensile test*

### 3.2 Analysis and discussion of MR test results between [0°] and extruded PETG specimens

Figure 3-4 presents the comparison of MR tests results between [0°] and extruded PETG specimens. Results from two tests are presented for each type of PETG specimens, showing good repeatability of the test results, especially before the yield point. The comparison between conventionally extruded and 3D printing PETG specimens is focused on the QS stress, applied stress, viscous stress as well as the ratio of QS to applied stresses. Values for  $\tau_r$  and  $\sigma_0$  will be discussed in the latter sections, to explore their relationship with transitions shown by the applied and QS stresses.

Figures 3-4 (a) and (b) are the QS and applied stress-stroke curves, respectively. The extruded specimens have better repeatability compared to the [0°] specimens. The two curves for the extruded specimens are almost identical but for the [0°] specimens some inconsistency is shown especially after the yield point, during the neck development. At the same stroke, extruded specimens have higher QS and applied stresses than [0°] specimens. The maximum applied stress for the extruded specimens is 51.5MPa at the stroke of 1mm, compared with the yield strength of PETG that is determined from tensile tests is from 47.9MPa to 52.9MPa [52], and for [0°] specimen 45.3MPa at the stroke of 1.1mm, as indicated using black circles in Figure 3-4 (b). This suggests that the maximum applied stress for [0°] specimens is 88% of that for the extruded specimens. Similarly, Figure 3-4 (a) suggests that as indicated using black circles, the maximum QS stress for extruded specimens is 41.2MPa, at the stroke of 0.8mm, but for [0°] specimen 36.7MPa at the stroke of 0.8mm. The latter is about 89% of that for the extruded specimen. So, it is clear that the [0°] specimen has lower yield strength and is less stiff than the extruded specimen. This is believed to be mainly caused by the voids in the [0°] specimen, as even with the machine setting of 100% infill rate, the 3D printed specimens still contain voids [34].

Figure 3-4 (c) compares  $\sigma_r(0)$  values between extruded and 3D-printed [0°] specimens. Before the stroke of 0.7mm, the  $\sigma_r(0)$  values between these two types of specimens do not show a clear difference but the  $\sigma_r(0)$  value for the extruded specimens increases dramatically from the stroke of 0.7mm, much higher than that for [0°] specimen. This difference can still be explained by the voids in [0°] specimen. For the ratio of QS stress to the applied stress, as shown in Figure 3-4 (d) which removes the effect of voids, results for the extruded and the 3D-printed [0°] specimens are

consistent, which suggests that despite the difference in the absolute stress values between the different types of specimens, the relaxation performance in terms of the ratio of QS stress to the applied stress as a function of stroke does not show any significant difference.

In conclusion, the main effect of the different relaxation performance between conventionally extruded and 3D printed [0°] PETG specimens is the voids in the 3D printed specimens. Results from the 3D printing are more inconsistent than those from the conventional extrusion.

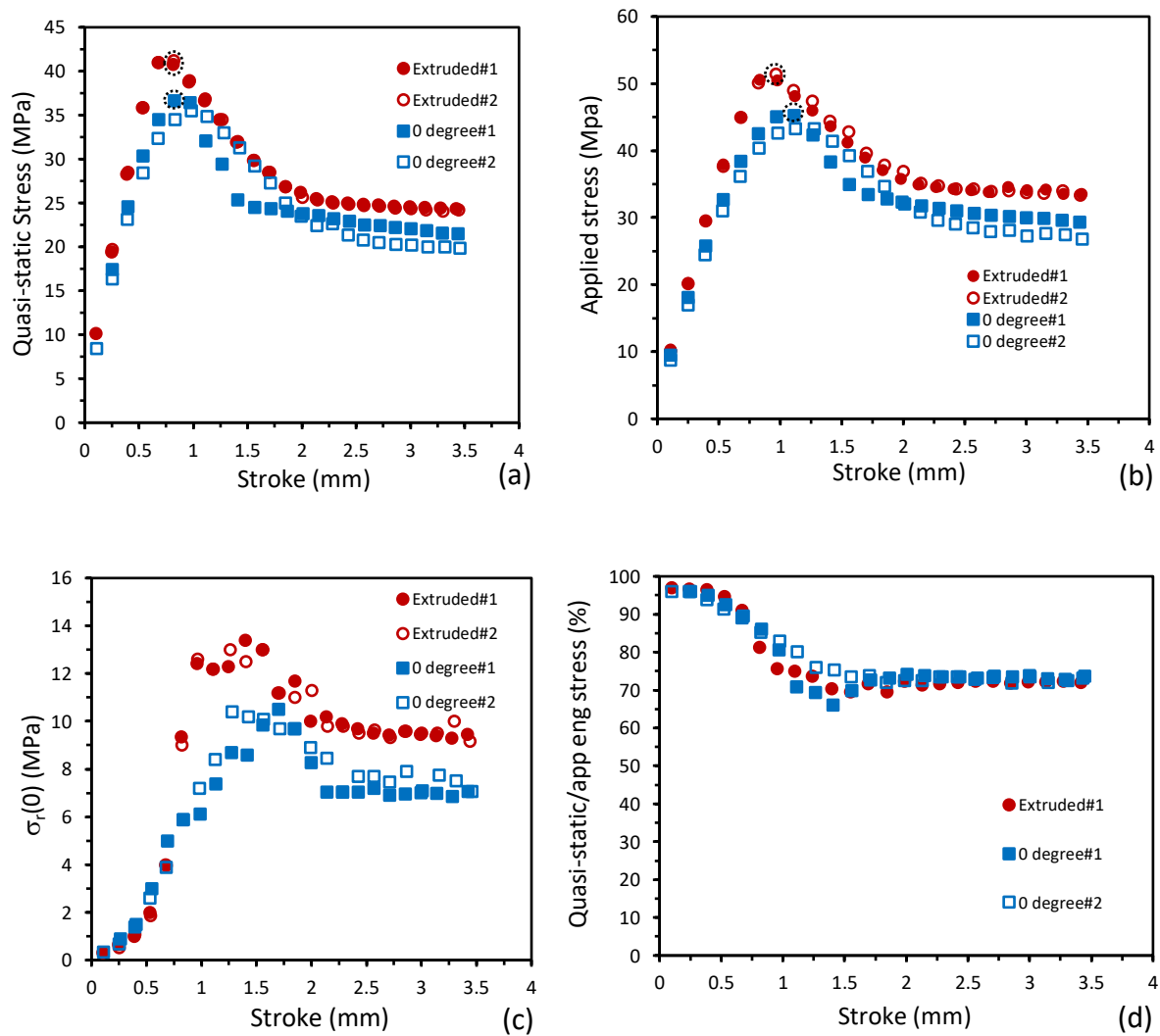


Figure 3-4 Comparison of MR test results vs. stroke between extruded and [0°] 3D printed PETG specimens, circles stand for the maximum stress of each type of specimen. (a) QS stress (b) Applied stress (c)  $\sigma_r(0)$  (d) the ratio of quasi-static stress/applied stress

### 3.3 Analysis and discussion of MR test results for 3D printed PETG specimens of $[0^\circ]$ , $[\pm 30^\circ]_s$ , and $[\pm 45^\circ]_s$

Figure 3-5 presents the comparison of MR tests results between three different types of 3D printed PETG specimens, to investigate the effect of raster angles on the relaxation performance. Two repeated tests were conducted for each type of PETG specimens. QS stress, applied stress, viscous stress as well as the ratio of QS/applied stress as functions of stroke are presented, same as those in the previous section between extruded and  $[0^\circ]$  specimens.

Figures 3-5 (a) and (b) are curves of QS and applied stress vs. stroke, respectively. The three types of specimens show some degree of inconsistency, but their values and the trend lines between the two tests still show some similarities. Note that one of the  $[\pm 30^\circ]_s$  specimens, 30 degree#2, did not fracture during the test, but the fracture process started at the stroke of 2.5mm. Another  $[\pm 30^\circ]_s$  specimen, 30degree#1, and all  $[\pm 45^\circ]_s$  specimens fractured during the tests. The 30degree#1 specimen started fracturing at the stroke of 2mm and fractured at the stroke of 2.3mm, and the two  $[\pm 45^\circ]_s$  specimens, fractured at the strokes of 2.9 and 2.4mm. These curves clearly show that at a given stroke, the applied and QS stresses are in the order of:  $[0^\circ] > [\pm 30^\circ]_s > [\pm 45^\circ]_s$ , but when at the plateau regions, stress curves for  $[0^\circ]$  specimens are closer to the stress curves for  $[\pm 30^\circ]_s$  specimens. The maximum applied stress for  $[0^\circ]$  specimens is 45.3MPa at the stroke of 1.1mm, for  $[\pm 30^\circ]_s$  specimens is 31.2MPa at the stroke of 1mm, for  $[\pm 45^\circ]_s$  specimens is 19.8MPa at the stroke of 0.9mm, as indicated using black circles in Figure 3-6 (b). The ratio for the maximum applied stress for  $[\pm 30^\circ]_s$  and  $[\pm 45^\circ]_s$  specimens to  $[0^\circ]$  specimen is 68.8% and 43.7%, respectively. The maximum QS stress for  $[0^\circ]$  specimens is 36.7MPa at the stroke of 0.8mm, for  $[\pm 30^\circ]_s$  specimens 24.3MPa at the stroke of 0.8mm, and for  $[\pm 45^\circ]_s$  specimens 14.6MPa at the stroke of 0.7mm, as indicated using black circles in Figure 3-6 (a). The ratio of the maximum QS stress for  $[\pm 30^\circ]_s$  and  $[\pm 45^\circ]_s$  specimens to that for  $[0^\circ]$  specimen is 66.2% and 39.8%, respectively.

Figure 3-5 (c) is the comparison of  $\sigma_r(0)$  values among 3D printed specimens. The figure shows that during the small deformation, with the stroke less than 0.8mm,  $\sigma_r(0)$  values are similar with no clear difference. But for  $[\pm 45^\circ]_s$  and  $[\pm 30^\circ]_s$  specimens  $\sigma_r(0)$  values stopped increasing at the stroke of 0.9mm and 1.1mm, respectively, though for the  $[0^\circ]$  specimens  $\sigma_r(0)$  values continue increasing till the stroke reached around 1.6 mm. They start showing the difference at the stroke

of 1mm, with the  $\sigma_r(0)$  values for  $[0^\circ]$  and  $[\pm 30^\circ]_s$  specimens larger than those for  $[\pm 45^\circ]_s$  specimens.  $\sigma_r(0)$  values for  $[0^\circ]$  specimens are higher in the necking region (from 1mm to 2.3mm), compared to those for  $[\pm 30^\circ]_s$  specimens, though when the plateau region was reached, there was no clear difference between curves for  $[\pm 30^\circ]_s$  and  $[\pm 45^\circ]_s$  specimens. The difference in relaxation performances among these specimens may come from two parts. One is the different porosities between different types of 3D printed specimens, and the other is the effect of the raster angles. Figure 3-5 (d) compares the ratio of QS stress to the applied stress, which removes the effect of the voids. Since two tests from same types of specimens show similar trends, for the convenience of comparison, only one of the two repeated tests is shown in Figure 3-5 (d) for each type of specimens. The figure suggests that when the curves reached the plateau region, all types of specimens should have the same QS/applied stress ratio, but when they approaching to their maximum applied stress level, the stress ratio for  $[\pm 45^\circ]_s$  specimen showed the steepest drop and that for  $[\pm 30^\circ]_s$  specimen the second steepest.

In conclusion, the raster angles have significant effects on the mechanical performance of 3D printed specimens. Stiffness of the 3D printed specimens is in the order of  $[0^\circ] > [\pm 30^\circ]_s > [\pm 45^\circ]_s$ .  $[0^\circ]$  specimens survived at the end of the test, but  $[\pm 30^\circ]_s$  and  $[\pm 45^\circ]_s$  specimens started fracturing during the tests. Despite the possible difference of void content and distribution among these specimens, the ratio of QS/applied stress ratio still shows some difference. The ratio for  $[\pm 45^\circ]_s$  specimens dropped fastest to their plateau while  $[0^\circ]$  specimens dropped slowest, and eventually when they all reach their plateau, the ratio becomes close to each other.

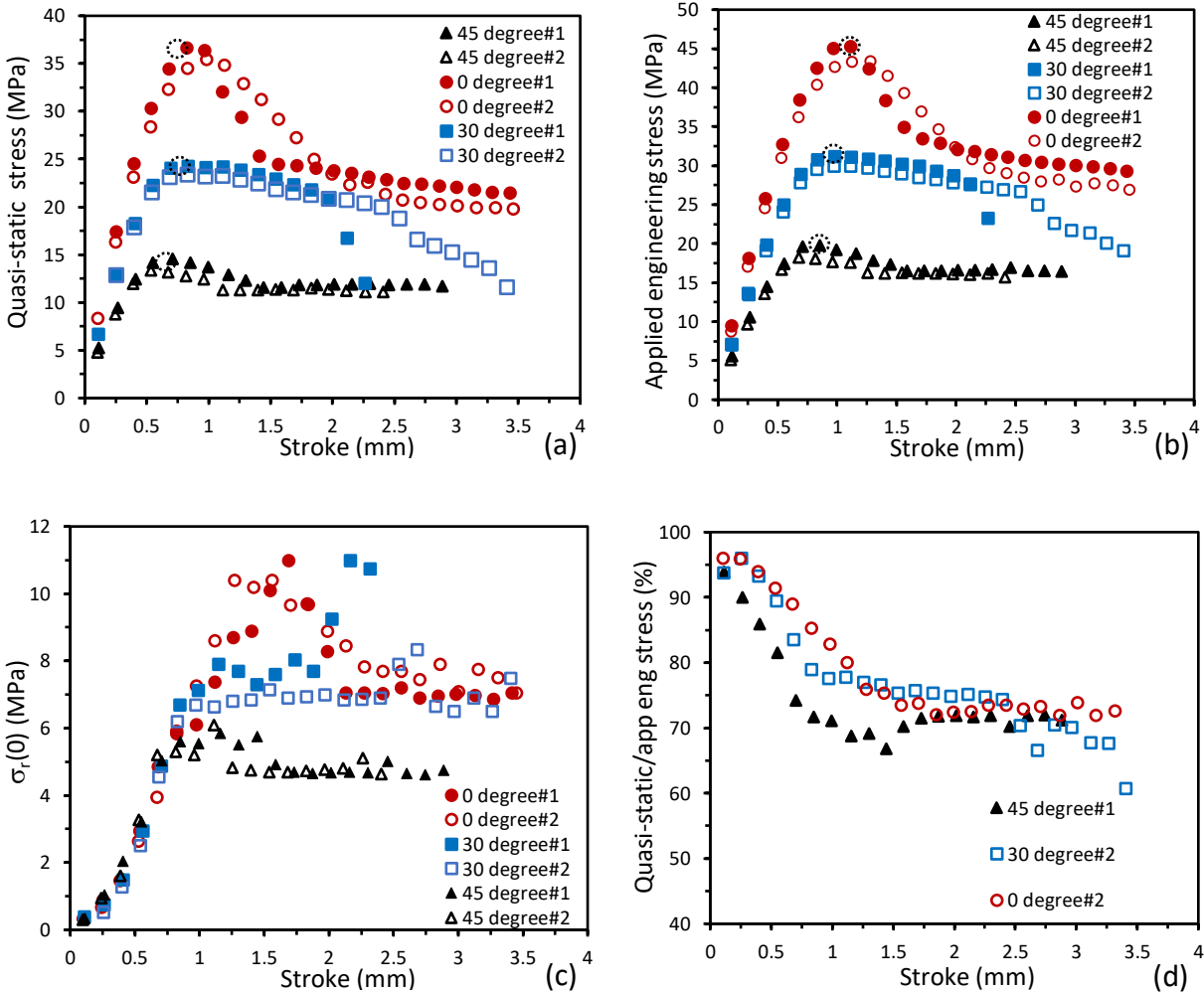


Figure 3-5 Comparison of MR test results between three different types of 3D printed PETG specimens, circles stand for the maximum stress of each type of specimen, (a) Quasi-static stress vs. stroke, (b) Applied stress vs. stroke, (c)  $\sigma_r(0)$  vs. stroke, (d) The ratio of quasi-static stress/applied stress vs. stroke.

### 3.4 Relationship among QS stress, applied stress, and fitting parameters for the extruded specimens

This section is focused on the analysis of curves for QS stress, applied stress and fitting parameters ( $\sigma_0$ ,  $\sigma_r(0)$  and  $\tau_r$ ) as functions of stroke, to examine the relationship among those curves for the extruded PETG specimens from the MR test. Since MR test results for extruded specimens are pretty consistent, as shown in section 3.2, for clarity only results from one specimen is used to represent data for the extruded specimens.



Figure 3-6 presents MR test results for an extruded PETG specimen. Figure 3-6 (a) shows applied stress and QS stress as functions of stroke. The former is the stress applied at the beginning of each relaxation stage, and the latter determined by removing viscous stress component,  $\sigma_r(0)$ , from the applied stress at the beginning of the relaxation stage. The figure suggests that the deformation process contains three noticeable transitions, with critical strokes for the transitions determined using the change of the curve trend line, as indicated using dashed circles in the figure.

The first transition is at the point where the stress-stroke curve changes from a linear curve to a non-linear one. Note that since both curves in Figure 3-6 (a) have the first transition at the same stroke, and these two curves are very close at the first transition point, for convenience, only one dashed circle is used to represent the transition and is on the applied stress curve. Trend line for the linear relationship is established using the first two data points in the curve, as shown on the applied stress curve in Figure 3-6 (a). Note that the same trend line can also be applied to the QS stress curve since the two curves at this stage are very close to each other, suggesting that viscous stress takes a very small component of the applied stress at this stage. Since the fourth data point in the curves of Figure 3-6 (a) does not fall onto the trend line, transition must have occurred between the third and the fourth data points, as indicated using a dashed circle. Figure 3-6 (a) also suggests that the two curves start showing a clear difference at the fourth data point, suggesting that viscous stress is significant enough at this deformation level.

The second transition is at the peak of the two curves in Figure 3-6 (a), which occurs at a smaller stroke for QS stress (about 0.7mm) than that for the applied stress (about 1mm). The difference is believed to be caused by the continuous increase of  $\sigma_r(0)$  at this stroke range, as indicated in Figure 3-6 (b), which resulted in the continuous increase of the applied stress, even though the QS stress started decreasing at the stroke of 0.7mm.

The third transition is for the start of a plateau region on the two curves in Figure 3-6 (a), which is from the stroke about 2mm for the applied stress and 1.8mm for the QS stress. For the  $\sigma_r(0)$  curve, as shown in Figure 3-6 (b), the plateau started at a stroke about 2mm. Figure 3-6 (b) also contains a dashed line to represent the applied stress curve, as a reference for the comparison. Same dashed line is also included in Figures 3-6 (c) and (d). The three transition points identified on the applied stress curve in Figure 3-6 (a) are also included in the dash line in Figures 3-6 (b), (c) and (d).

For the  $\sigma_r(0)$  curve in Figure 3-6 (b), the first three data points follow a linear relationship, as indicated by the black trend line. Clearly, the fourth data point at the stroke of 0.5mm follows a different trend line, and the stroke for the transition is similar to the stroke for the change from linear to non-linear stress-stroke relationship which is the first transition point on the applied stress curve, as indicated by the dashed circle. Therefore, the first transition is also detectable using the  $\sigma_r(0)$ -stroke curve. After the first transition,  $\sigma_r(0)$  shows a sharp increase till the stroke of 1mm where the  $\sigma_r(0)$  value becomes relatively constant. As discussed earlier, the second transition point in the applied stress curve occurred at the stroke of 1mm. Therefore, this transition can also be detected using the  $\sigma_r(0)$ -stroke curve. Similarly, the third transition point on the applied stress curve, at the stroke of 2mm, can also be detected in the  $\sigma_r(0)$ -stroke curve.

Figure 3-6 (c) presents  $\sigma_0$ -stroke curve and applied stress vs. stroke trend curve with three transition points as indicated using three open black circles, determined from Figure 3-6 (a). Similarly, the change from linear to onset of non-linearity is between the third and fourth data points, which is about the same stroke with the first transition point of applied stress curve. Then the curve experienced a sharp increase when passing through the stroke of 0.7mm where the maximum QS stress occurred. The second transition point matches with the local maximum  $\sigma_0$  curve at the stroke of 1mm. Then the curve shows a valley in the necking region,  $\sigma_0$  value starts increasing at the stroke of 1.4mm, which suggests that there may be a transition point in the necking region that cannot be detected from other curves. From the stroke of 2mm, which is at the same stroke with the third transition point of applied stress curve, the  $\sigma_0$  curve increases slowly and smoothly, indicating the curve enters a plateau region.

Figure 3-6 (d) presents a  $\tau_r$ -stroke curve, and the corresponding applied stress-stroke curve with three transition points indicated by the dashed circles. As mentioned earlier in Chapter 2,  $\tau_r$  values could remain relatively constant with the change of the stroke. Therefore, it is not surprising to see that little correlation exists between  $\tau_r$  and the three transition points on the applied stress. However,  $\tau_r$  values still need to be adjusted in order to fit all stress relaxation curves from the MR test. For the extruded specimens, as shown in Figure 3-6 (d), a small  $\tau_r$  value of 2000s is needed to fit the first relaxation curve, and then the  $\tau_r$  value needs to be increased to a large value of 12000s for the next relaxation curve. The  $\tau_r$  value remains to be 12000s through the maximum

applied stress, till the stroke of 1.5mm at which  $\tau_r$  starts dropping quickly, eventually to 5500s for the rest of the strokes in the MR test.

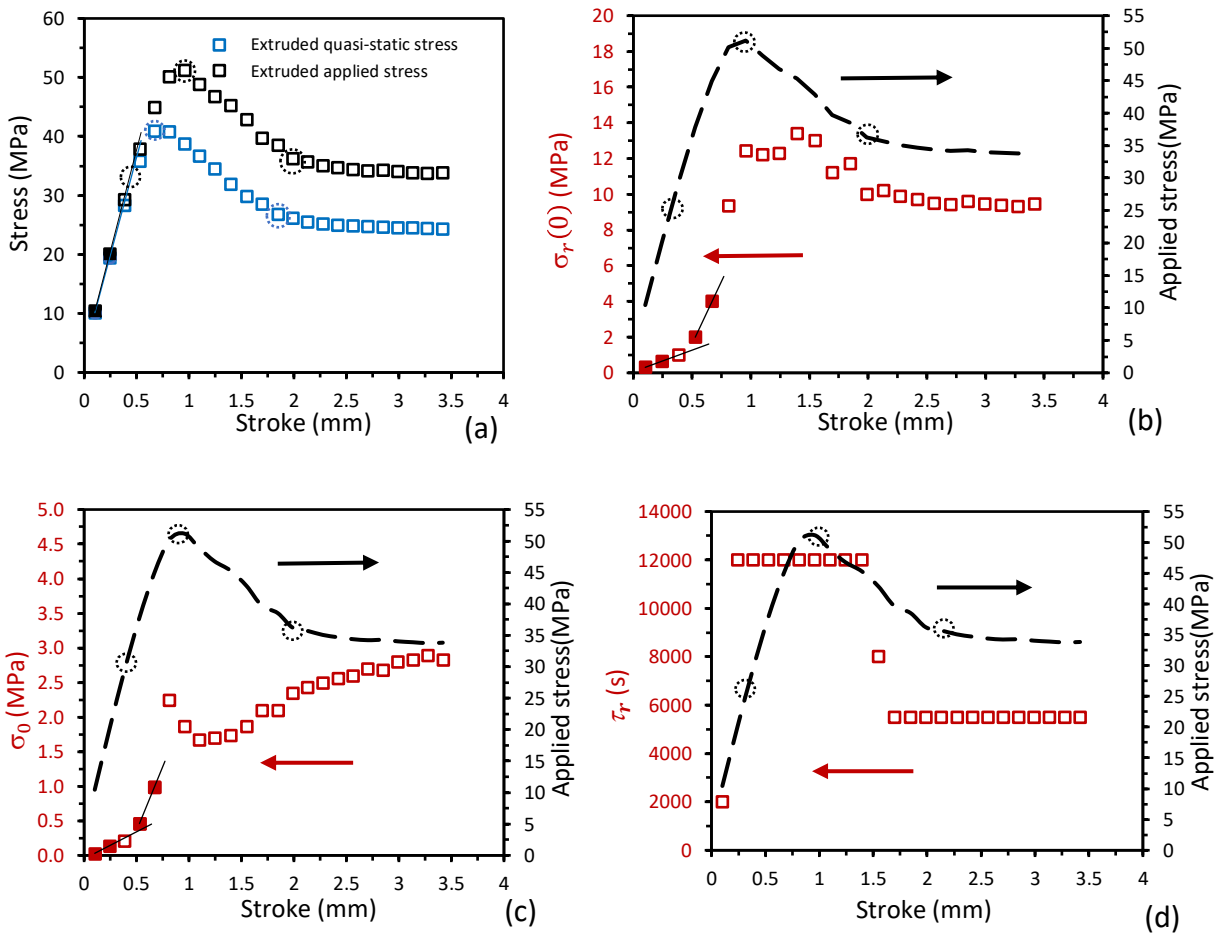


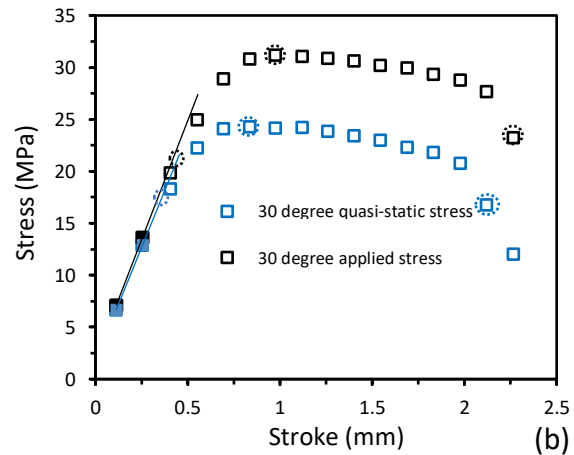
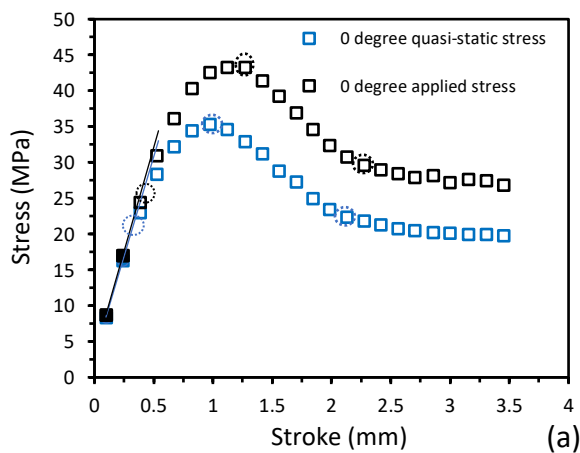
Figure 3-6 MR test results as a function of stroke for an extruded PETG specimen, with three dashed black circles standing for three transition points on the applied stress curve,:(a) QS stress and applied stress, blue circles stand for the transition points of the QS stress curve (b)  $\sigma_r(0)$  and applied stress trend curve. (c)  $\sigma_0$  and applied stress trend curve, and (d)  $\tau_r$  and applied stress trend curve.

### 3.5 Comparison of QS stress, applied stress and relaxation parameters among specimens of different types

After the relationship of QS stress, applied stress and fitting parameters  $\sigma_0$ ,  $\sigma_r(0)$  and  $\tau_r$  as a function of stroke are examined for the extruded specimen, the same approach was used to analyze 3D printed PETG specimens. This section is focused on the comparison of the relationship among different types of PETG specimens for the same types of curves. For clarity, only results from one specimen are used to represent the difference.

### 3.5.1 Applied stress and QS stress versus stroke curves

Figure 3-7 shows the applied stress and QS stress for different types of 3D printed specimens. Curves for  $[0^\circ]$  and  $[\pm 45^\circ]_s$  specimens, as shown in Figure 3-7 (a) and (c), respectively, have similar trends, each of which includes three transition points for applied stress and QS stress. The trend lines in the curves for the  $[\pm 45^\circ]_s$  specimen is clearly different, suggesting that from the second relaxation stage, viscous stress takes a significant component of the applied stress, but for the curve of  $[0^\circ]$  specimens, viscous stress is still negligible at the second relaxation stage. For the stress curves of the  $[\pm 30^\circ]_s$  specimen, as shown in Figure 3-7 (b), the first and second transition points can be identified using the same approach, but viscous stress is still a small component of the applied stress at the second relaxation stage. After the second transition point, the curves for the  $[\pm 30^\circ]_s$  specimen decreased slowly to generate fractured which is different from any other PETG specimens. Therefore, the third transition point for the  $[\pm 30^\circ]_s$  specimen can be considered as the point at which the curve start dropping. This transition is at the stroke of 2.3mm for the applied stress, and the  $[\pm 30^\circ]_s$  specimen soon fractured after this point. For the QS stress curve, the third transition point for the  $[\pm 30^\circ]_s$  specimen is at the stroke of 2.1mm, one stage earlier than that for the applied stress curve. This suggests that fracture started in the  $[\pm 30^\circ]_s$  specimen during the stress relaxation at the stroke of 2.1mm.



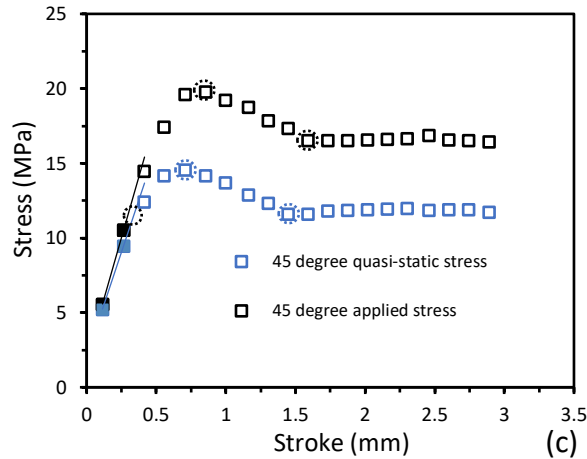


Figure 3-7 QS stress and applied stress versus stroke curves for different types of 3D printed specimens, blue circles stand for the transition points of the QS stress curve, black open circles stand for three transition points of applied stress curve, (a)  $[0^\circ]$ , (b)  $[\pm 30^\circ]_s$ , (c)  $[\pm 45^\circ]_s$

### 3.5.2 Applied stress and $\sigma_r(0)$

Figure 3-8 shows the applied stress trend curves with three transition points as indicated using black dashed circles and  $\sigma_r(0)$  curves for different types of the 3D printed specimens. With the same analysis approach that was used for the extruded specimen, the first and second transition points of applied stress curves can be detected using the  $\sigma_r(0)$  curves for all types of PETG specimens and these relationships are similar among all types of PETG specimens. After the second transition point of the applied stress curves, the  $\sigma_r(0)$  curves for  $[0^\circ]$  and  $[\pm 45^\circ]_s$  specimens decreased slightly, as shown in Figure 3-8 (a) and (c), to reach a plateau. The third transition point of the applied stress curves can also be detected using the  $\sigma_r(0)$ -stroke curves for  $[0^\circ]$  and  $[\pm 45^\circ]_s$  specimens, but for the  $[\pm 30^\circ]_s$  specimen, as shown in Figure 3-8 (b), the  $\sigma_r(0)$  curve reaches a relatively stable section after the second transition point, but at the stroke of 2.1mm, the  $\sigma_r(0)$  curve increase dramatically, indicating that the specimen starts fracturing. Note that this is not corresponding to the third transition point of the applied stress curve, as the fracture was occurred during the relaxation at the stroke of 2.1mm, so the applied stress curve cannot detect this change at the beginning of the relaxation at the stroke of 2.1mm but show this change at the beginning of the next relaxation stage.

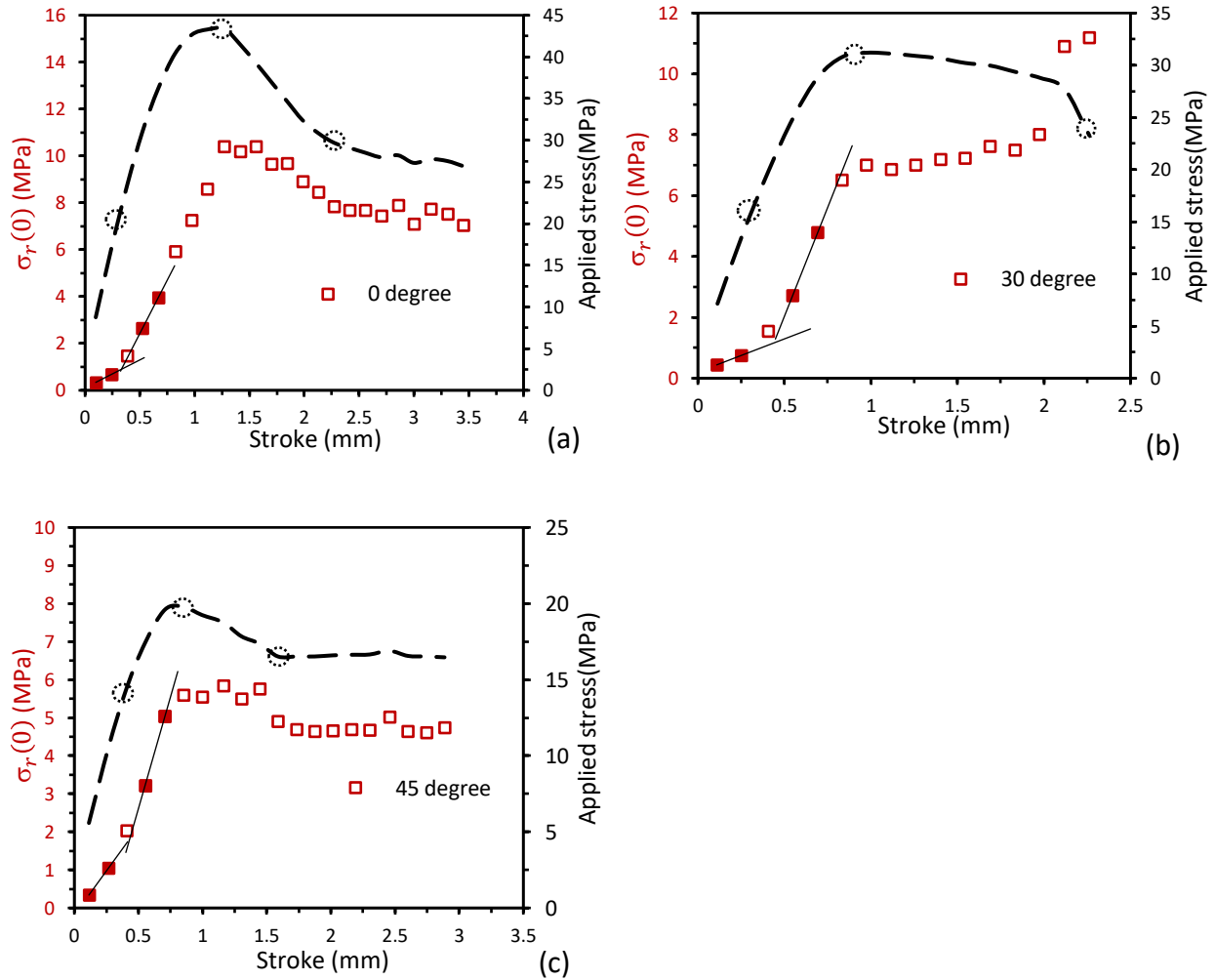


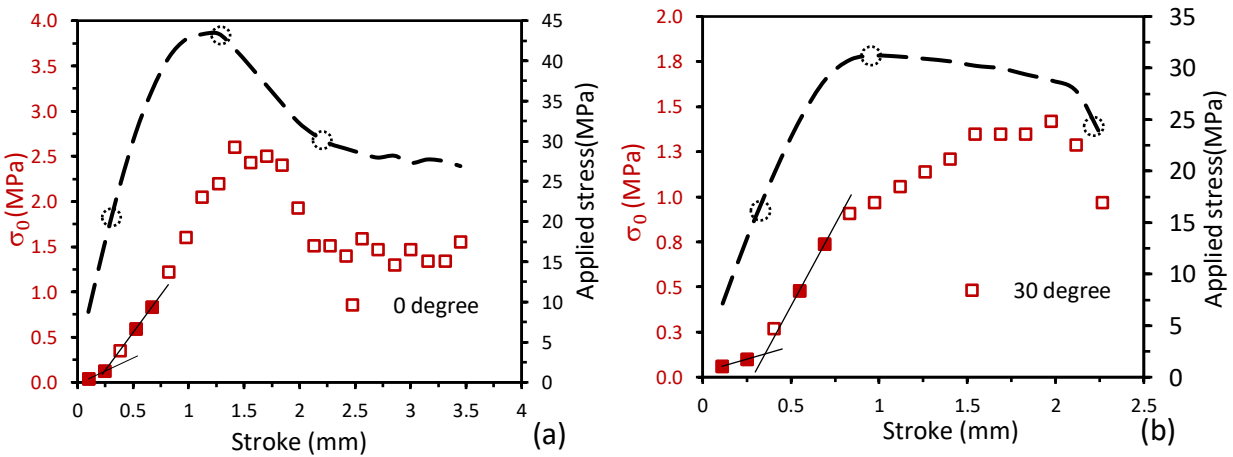
Figure 3-8 Applied stress and  $\sigma_r(0)$  versus stroke curves for different types of 3D printed specimens, black open circles stand for three transition points of applied stress curve, (a)  $[0^\circ]$ , (b)  $[\pm 30^\circ]_s$ , (c)  $[\pm 45^\circ]_s$

### 3.5.3 Applied stress and $\sigma_0$ versus stroke curve

Figure 3-9 shows trend curves of applied stress with three transition points indicated using black dashed circles and  $\sigma_0$  curves for different types of the 3D printed specimens. For the  $[0^\circ]$  specimen, as shown in Figure 3-9 (a), the point where the trend line change is at the different stroke compared with the first transition of the applied stress curve, as shown in Figure 3-9 (b) for  $[\pm 30^\circ]_s$  specimen. The first transition of the applied stress curve can be detected using the change of the trend line from the  $\sigma_0$  curve for  $[\pm 45^\circ]_s$  specimen, as shown in Figure 3-9 (c) in which the  $\sigma_0$  curve increases linearly until the stroke of 0.7mm, which suggests that the first transition point of the applied stress curve cannot be clearly detected in the  $\sigma_0$  curve. Therefore,  $\sigma_0$  may not always be

able to indicate the first transition of applied stress curves for all types of PETG specimens. The second transition point of applied stress matches with the trend of change of the  $\sigma_0$  curves for all types of specimens. For  $[0^\circ]$  and  $[\pm 45^\circ]_s$  specimens, the third transition points of applied stress can be indicated using the  $\sigma_0$  curves. For the  $[\pm 30^\circ]_s$  specimen, however, the  $\sigma_0$  curve starts dropping at the stroke of 2.1mm, which is the point at which the specimen started fracture. Therefore, the third transition point of applied stress curve cannot be detected using the  $\sigma_0$  curve as fracture occurred during the relaxation stage at this stroke.

Similar to the extruded specimen  $\sigma_0$  curve, for all types of 3D printed specimens'  $\sigma_0$  curves, seems like every  $\sigma_0$  curves also show a transition point between the second and the third transition points that cannot be detected by other types of curves and the  $\sigma_0$  curves for different specimens seems show different trends during this region. For the 3D printed  $[0^\circ]$  specimen, the  $\sigma_0$  curve keep constant and decreases in the neck forming stage, and there may have a transition point around the region when the curve starts decreasing, around the stroke of 1.8mm. For the  $[\pm 30^\circ]_s$  specimen, the  $\sigma_0$  curve keep increasing and then reach a steady state, and there may have a transition point around the region when the curve stops increasing, around the stroke of 1.5mm. For the  $[\pm 45^\circ]_s$  specimen, the  $\sigma_0$  curve keeps increasing and then decreasing in the necking region, and there may have a transition point around the region where the curve stops increasing and start decreasing, around the stroke of 1.3mm. However, due to scattering of the data and the limit experiment data obtained, the conclusion cannot be derived at this stage.



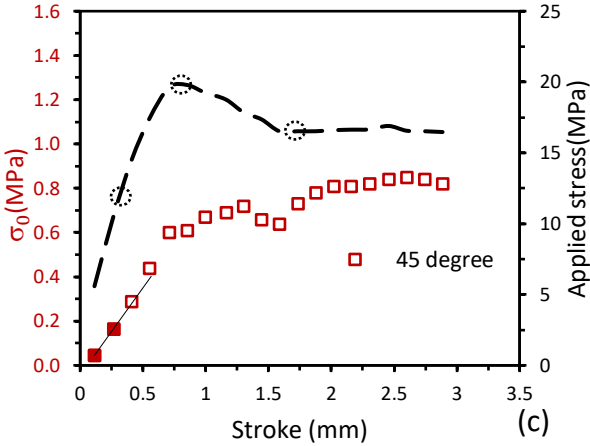


Figure 3-9 Applied stress and  $\sigma_0$  versus stroke curves for different types of 3D printed specimens, black open circles stand for three transition points of applied stress curve, (a)  $[0^\circ]$ , (b)  $[\pm 30^\circ]_s$ , (c)  $[\pm 45^\circ]_s$

#### 3.5.4 Applied stress and $\tau_r$

Figure 3-10 shows the applied stress curves with three transition points as indicated using black dashed circles, and  $\tau_r$  curves for different types of the 3D printed specimens. Similarly, to the extruded specimens,  $\tau_r$  values show little correlation with the transition of the applied stress curves. However, different  $\tau_r$  values would be needed for different regions. For example, a small  $\tau_r$  value of around 2000s-3000s would be used for the first relaxation stage, except for the  $[\pm 30^\circ]_s$  specimen. Start from the next relaxation stage till the region around the maximum applied stress, a large  $\tau_r$  value of 12000s would be needed. During the necking region of  $[0^\circ]$  specimens,  $\tau_r$  value could decrease to 8000s, and when the applied stress curve approach to the plateau region, the  $\tau_r$  value would further decrease to 5500s and remain constant for the entire plateau region. For the  $[\pm 45^\circ]_s$  specimens,  $\tau_r$  value of 8000s needs to be used during the necking region, and when the applied stress curve reaches the plateau region, the  $\tau_r$  value would decrease to 5500s. For the  $[\pm 30^\circ]_s$  specimen,  $\tau_r$  value of 8000s would be used after the maximum applied stress.



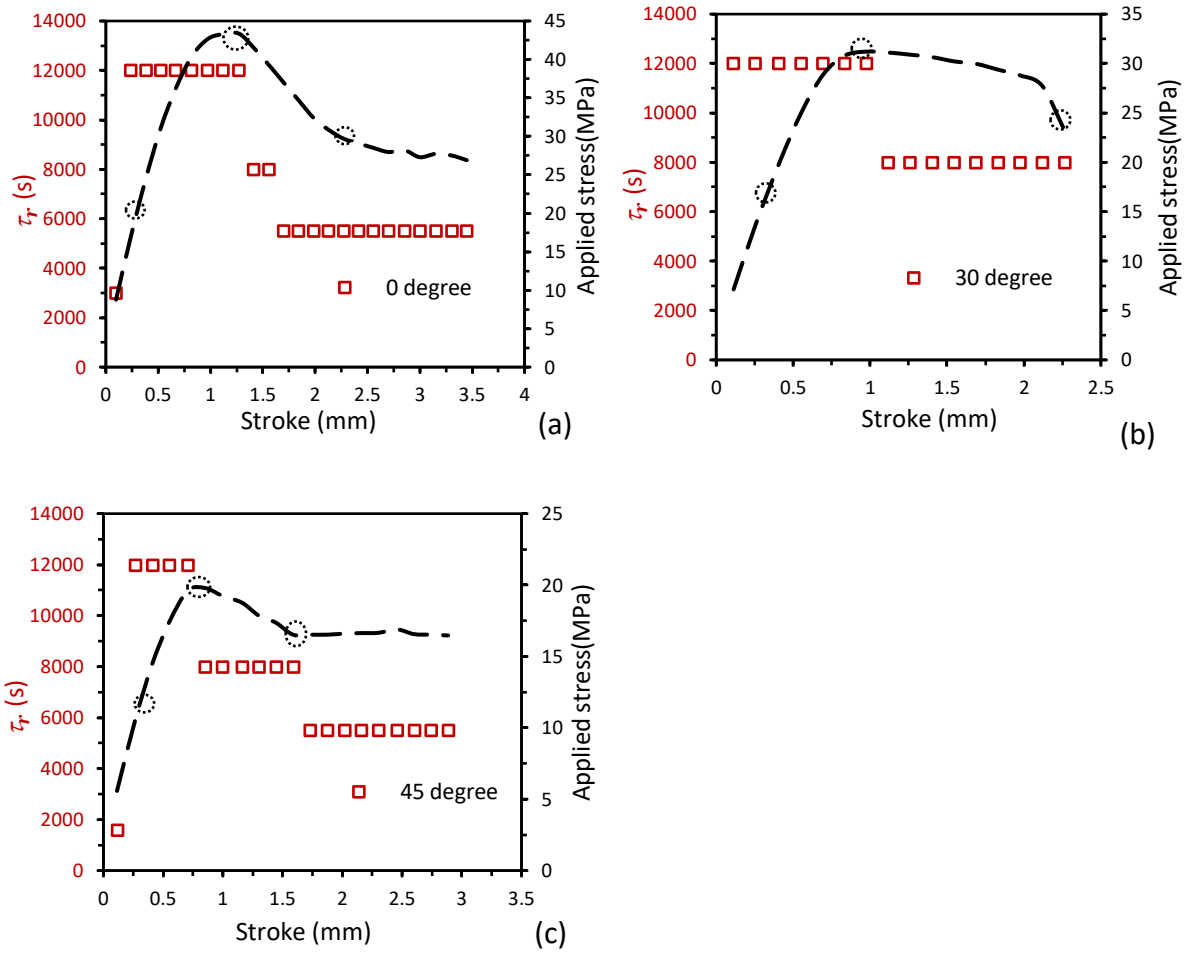


Figure 3-10 Applied stress and  $\tau_r$  versus stroke curves for different types of 3D printed specimens, black open circles stand for three transition points of applied stress curve, (a)  $[0^\circ]$ , (b)  $[\pm 30^\circ]_s$ , (c)  $[\pm 45^\circ]_s$

## Chapter 4 Analysis of test results using the classical laminate theory

In chapter 3, the effects of the raster angles are presented and show that specimen stiffness are in the order of:  $[0^\circ]_s > [\pm 30^\circ]_s > [\pm 45^\circ]_s$ . By considering each layer of a 3D printed specimens as a lamina with filament as fiber in certain directions, the whole 3D printed specimens can be considered as a laminate. Therefore, a question is raised on the possibility of applying classical laminate theory (CLT) to prediction of mechanical properties for 3D printed specimens. The aim of this chapter is to examine applicability of describing the mechanical behaviour of 3D printed specimens with different raster angle configurations by using CLT and to compare the results with experimental results. Finally, since voids affect different types of 3D printed specimens in different ways, and CLT does not consider those effects, some modifications to CLT are suggested to consider the void effect.

### 4.1 Review of classical laminate theory and literature review

This section introduces analytical equations from CLT and summarizes previous works about using CLT to describe mechanical properties of FDM parts.

#### 4.1.1 Analytical equations from CLT for FDM parts

CLT is to use mechanical properties of a unidirectional lamina with orthotropic properties ( $E_1$ ,  $E_2$ ,  $\nu_{12}$  and  $G_{12}$ ) to describe the elastic behaviour of a laminate that is formed by compiling a number of laminae together with specific orientation. This section introduces the constitutive equations derived from CLT.

The laminate is a thin plate subjected to a plane-stress loading condition. Each lamina has orthotropic elastic properties. The stress-strain relationship for a unidirectional lamina is given by:

$$\begin{Bmatrix} \sigma_1 \\ \sigma_2 \\ \tau_{12} \end{Bmatrix} = \begin{bmatrix} Q_{11} & Q_{12} & 0 \\ Q_{12} & Q_{22} & 0 \\ 0 & 0 & Q_{66} \end{bmatrix} \begin{Bmatrix} \varepsilon_1 \\ \varepsilon_2 \\ \gamma_{12} \end{Bmatrix} \quad \text{Equation 4-1}$$

where subscripts 1 and 2 are the filament and transverse directions, respectively,  $\sigma$  normal stress,  $\tau$  in-plane shear stress,  $\varepsilon$  normal strain,  $\gamma$  in-plane shear strain, and  $Q_{ij}$  the reduced stiffness which is expressed as a function of mechanical property constants of the unidirectional lamina, as shown below:

$$Q_{11} = \frac{E_1}{1-\nu_{12}\nu_{21}}, Q_{12} = \frac{\nu_{12}E_2}{1-\nu_{12}\nu_{21}}, Q_{22} = \frac{E_2}{1-\nu_{12}\nu_{21}}, Q_{66} = G_{12} \text{ and } \frac{\nu_{12}}{E_1} = \frac{\nu_{21}}{E_2} \quad \text{Equation 4-2}$$

In the above equations, there are four independent material constants and one dependent material constant:

$E_1$ : elastic modulus in the filament direction

$E_2$ : elastic modulus in the transverse direction

$G_{12}$ : in-plane shear modulus

$\nu_{12}$ : major Poisson's ratio

$\nu_{21}$ : minor Poisson's ratio which is a dependent constant

The stress-strain relation for an angle lamina, as shown in Figure 4-1, can be described using two coordinate systems, a local coordinate system which is the one used for unidirectional lamina with axis 1 in the fiber direction and axis 2 the transverse direction, and a global coordinate system with x- and y-axes being the loading and transverse directions, respectively. Figure 4-1 presents the two coordinate systems, with the loading in the vertical direction. Angle between x-axis and 1-axis is denoted as  $\theta$ .

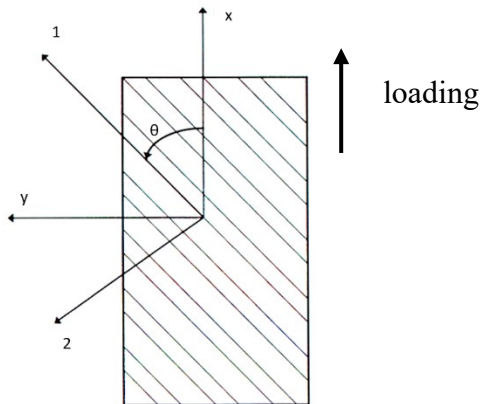


*Figure 4-1 Schematic of an angle lamina showing local 1-2 and global x-y coordinate systems.*

The stress-strain relation for a unidirectional lamina in the global x-y coordinate system can be expressed as:

$$\begin{bmatrix} \sigma_x \\ \sigma_y \\ \tau_{xy} \end{bmatrix} = \begin{bmatrix} \bar{Q}_{11} & \bar{Q}_{12} & \bar{Q}_{16} \\ \bar{Q}_{12} & \bar{Q}_{22} & \bar{Q}_{26} \\ \bar{Q}_{26} & \bar{Q}_{26} & \bar{Q}_{66} \end{bmatrix} \begin{bmatrix} \varepsilon_x \\ \varepsilon_y \\ \gamma_{xy} \end{bmatrix} \quad \text{Equation 4-3}$$

$[\bar{Q}_{ij}]$  is the reduced stiffness matrix in in the global x-y coordinate system. Each element in  $[\bar{Q}_{ij}]$  is related to the reduced stiffness matrix in the local 1-2 coordinate system, with  $Q_{ij}$  and  $\theta$  expressed using expressions below in which  $c=\cos\theta$  and  $s=\sin\theta$ :

$$\begin{aligned} \bar{Q}_{11} &= Q_{11}c^4 + Q_{22}s^4 + 2(Q_{12} + 2Q_{66})s^2c^2 \\ \bar{Q}_{12} &= (Q_{11} + Q_{22} - 4Q_{66})s^2c^2 + Q_{12}(c^4 + s^4) \\ \bar{Q}_{22} &= Q_{11}s^4 + Q_{22}c^4 + 2(Q_{12} + 2Q_{66})s^2c^2 \\ \bar{Q}_{16} &= (Q_{11} - Q_{12} - 2Q_{66})c^3s - (Q_{22} - Q_{12} - 2Q_{66})s^3c \\ \bar{Q}_{26} &= (Q_{11} - Q_{12} - 2Q_{66})s^3c - (Q_{22} - Q_{12} - 2Q_{66})c^3s \\ \bar{Q}_{66} &= (Q_{11} + Q_{22} - 2Q_{12} - 2Q_{66})s^2c^2 + Q_{66}(c^4 + s^4) \end{aligned} \quad \text{Equation 4-4}$$

With Equation 4-4, the reduced stiffness matrix for laminae of different  $\theta$  values can be determined.

By stacking n laminae together in a designed sequence, a laminate is formed as shown in Figure 4-2, in which the mid-plane is x-y plane with z-axis in the upward direction. Thickness for layer k is expressed as  $h_k-h_{k-1}$ .

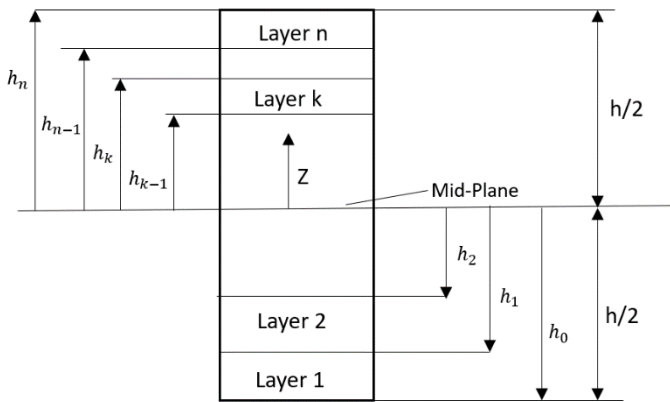


Figure 4-2 Schematic description of an n-layered laminate

Based on the CLT concept, the resultant normal and shear forces of the laminate,  $N_x$ ,  $N_y$  and  $N_{xy}$ , are related to the mid-plane strains,  $\varepsilon_x^0$ ,  $\varepsilon_y^0$  and  $\gamma_{xy}^0$ , and mid-plane curvatures,  $\kappa_x$ ,  $\kappa_y$  and  $\kappa_{xy}$  where  $\kappa_{xy}$  represents the twist curvature of the middle plane. This expression is given below:

$$\begin{bmatrix} N_x \\ N_y \\ N_{xy} \end{bmatrix} = \begin{bmatrix} A_{11} & A_{12} & A_{16} \\ A_{12} & A_{22} & A_{26} \\ A_{16} & A_{26} & A_{66} \end{bmatrix} \begin{bmatrix} \varepsilon_x^0 \\ \varepsilon_y^0 \\ \gamma_{xy}^0 \end{bmatrix} + \begin{bmatrix} B_{11} & B_{12} & B_{16} \\ B_{12} & B_{22} & B_{26} \\ B_{16} & B_{26} & B_{66} \end{bmatrix} \begin{bmatrix} \kappa_x \\ \kappa_y \\ \kappa_{xy} \end{bmatrix} \quad \text{Equation 4-5}$$

Similarly, the resultant bending and twisting moments of the laminate,  $M_x$ ,  $M_y$  and  $M_{xy}$ , are also related to the mid-plane strains and curvatures, as shown in the equation below:

$$\begin{bmatrix} M_x \\ M_y \\ M_{xy} \end{bmatrix} = \begin{bmatrix} B_{11} & B_{12} & B_{16} \\ B_{12} & B_{22} & B_{26} \\ B_{16} & B_{26} & B_{66} \end{bmatrix} \begin{bmatrix} \varepsilon_x^0 \\ \varepsilon_y^0 \\ \gamma_{xy}^0 \end{bmatrix} + \begin{bmatrix} D_{11} & D_{12} & D_{16} \\ D_{12} & D_{22} & D_{26} \\ D_{16} & D_{26} & D_{66} \end{bmatrix} \begin{bmatrix} \kappa_x \\ \kappa_y \\ \kappa_{xy} \end{bmatrix} \quad \text{Equation 4-6}$$

The matrices A, B, and D above are defined as:

$$\begin{aligned} A_{ij} &= \sum_{k=1}^n (\bar{Q}_{ij})_k (h_k - h_{k-1}) \\ B_{ij} &= \frac{1}{2} \sum_{k=1}^n (\bar{Q}_{ij})_k (h_k^2 - h_{k-1}^2) \\ D_{ij} &= \frac{1}{3} \sum_{k=1}^n (\bar{Q}_{ij})_k (h_k^3 - h_{k-1}^3) \end{aligned} \quad \text{Equation 4-7}$$

The resultant forces and moments for FDM parts can be determined using Equations 4-5 and 4-6 as functions of  $\bar{Q}_{ij}$  and thickness for each lamina, denoted as  $(\bar{Q}_{ij})_k$  and  $h_k-h_{k-1}$ , respectively, for the  $k^{\text{th}}$  lamina [35] [36].

#### 4.1.2 Literature review

Some researchers have already used CLT to describe the mechanical behaviour of the FDM parts. Casavola et al. [37] determined experimentally the Young's modulus for ABS and PLA with the stack sequence of [+30/-30/0/-30/+30]. They also used CLT to describe the mechanical behaviour of FDM parts by firstly determining  $E_1$  and  $E_2$  experimentally using single layer of FDM parts with raster angles of  $0^\circ$  and  $90^\circ$ . Value for  $\nu_{12}$  was determined by using strain gauges to measure experimentally the longitudinal and transverse deformations of  $0^\circ$  specimens, and  $G_{12}$  by (Give the generic nature of the measurement), following ASTM D3518-94. The results show that CLT can predict well the elastic modulus for FDM parts of ABS and PLA laminates of

[+30/−30/0/−30/+30] with errors of 1.07% and 5.37%, respectively. Mishra et al. [38] used CLT to predict the in-plane stiffness of polylactic acid (PLA), polylactic acid carbon black (PLA CB) and PLA/PLA CB biomaterial structures in three laminate configurations ( $0^\circ$ ,  $0^\circ/90^\circ$  and  $\pm 45^\circ$ ), using the same approach as Casavola et al. [37], to determine  $E_1$ ,  $E_2$ ,  $\nu_{12}$  and  $G_{12}$ . The results show that accuracy of the prediction is varied by the laminate configuration and material types. For example,  $[\pm 45^\circ]$  PLA/PLA CB composite specimen has the highest deviation of 19.75% compared to the experimental data, while the deviations for  $[\pm 45^\circ]$  PLA and PLA CB specimens were 0.94% and 0.3%, respectively.

Alaimo et al. [39] also used CLT to predict FDM specimens of ABS with raster angles of  $20^\circ$  and  $70^\circ$ . Similarly, they used  $0^\circ$  specimens to determine  $E_1$  and  $\nu_{12}$ , and  $90^\circ$  specimen to determine  $E_2$ . For  $G_{12}$ , they measured the elastic modulus of  $45^\circ$  specimen experimentally, based on which  $G_{12}$  value was determined [40][41]. The results show that some of the experimental data had good consistency with the estimation based on CLT, but CLT overestimated other experimental data. Magalhaes et al. [42] used CLT to predict elastic modulus of ABS specimens of  $[\pm 15^\circ]_s$  and  $[\pm 75^\circ]_s$ , and found that the prediction was close to the experimental values but still have some noticeable deviations. They suggested that this is because CLT does not consider voids, and in their study the void distribution and shape (triangular, diamond or rectangular) showed variation among laminates of different configurations.

All of the above studies applied experimentally determined elastic properties ( $E_1$ ,  $E_2$ ,  $\nu_{12}$  and  $G_{12}$ ) of uni-directional lamina to CLT directly without considering the possible effects of voids. Although some their predictions are in the acceptable range of deviations from the experimental results, other results still show the possibility of significant deviations which could be reconciled by considering the presence of voids, but such an idea was never verified. In addition, none of the studies has ever considered the viscous, time-dependent deformation behaviour of polymers, which should not be included in the use of CLT to predict mechanical properties. Therefore, the aim of this part of the study is to predict the mechanical behaviour of 3D printed specimens, with the consideration of volumetric content of voids and removal of the viscous contribution to the mechanical properties. In the end, possible modification of CLT to improve prediction of mechanical properties for 3D printed specimens is discussed.

## 4.2 Approach of applying CLT

### 4.2.1 Applying analytical equations from CLT to 3D printed specimens

This section describes the application of CLT to  $[\pm\theta]_s$  3D printed specimens, The stress-strain relation is given below, with the detailed derivations provided in Appendix A.

$$\begin{bmatrix} \sigma_x \\ 0 \\ 0 \end{bmatrix} = \begin{bmatrix} \bar{Q}_{11+\theta} & \bar{Q}_{12+\theta} & 0 \\ \bar{Q}_{12+\theta} & \bar{Q}_{22+\theta} & 0 \\ 0 & 0 & \bar{Q}_{66+\theta} \end{bmatrix} \begin{bmatrix} \varepsilon_x^0 \\ \varepsilon_y^0 \\ \gamma_{xy}^0 \end{bmatrix} \quad \text{Equation 4-8}$$

where  $\bar{Q}_{ij\pm\theta}$  is the stiffness for the  $[\pm\theta]_s$  3D printed specimen, for which the strains are expressed as:

$$\begin{bmatrix} \varepsilon_x^0 \\ \varepsilon_y^0 \\ \gamma_{xy}^0 \end{bmatrix} = \begin{bmatrix} \bar{Q}_{11+\theta} & \bar{Q}_{12+\theta} & 0 \\ \bar{Q}_{12+\theta} & \bar{Q}_{22+\theta} & 0 \\ 0 & 0 & \bar{Q}_{66+\theta} \end{bmatrix}^{-1} \begin{bmatrix} \sigma_x \\ 0 \\ 0 \end{bmatrix} \quad \text{Equation 4-9}$$

The inverse matrix of  $\bar{Q}_{ij\pm\theta}$  is denoted  $\bar{Q}_{ij\pm\theta}^*$ , i.e., the compliance matrix for the  $[\pm\theta]_s$  3D printed specimen. Then, the elastic modulus in the x-direction for  $[\pm\theta]_s$  3D printed specimen is:

$$E_x = \frac{1}{\bar{Q}_{11\pm\theta}^*} \quad \text{Equation 4-10}$$

where  $\bar{Q}_{11\pm\theta}^*$  is the element 11 in the  $\bar{Q}_{ij\pm\theta}^*$ . Thus, the elastic constants  $E_1, E_2, \nu_{12}$  and  $G_{12}$  for a unidirectional lamina need to be determined to predict the elastic modulus.

### 4.2.2 Determining $E_1$ and $E_2$

The first step of applying CLT is to find the reduced stiffness matrix  $Q_{ij}$  which requires determination of the elastic constants of the unidirectional lamina  $E_1, E_2, \nu_{12}$  and  $G_{12}$ .  $\nu_{12}$  is chosen to be 0.33 for both FEM simulation and CLT analysis [43]. This section focuses on the determination of elastic constants  $E_1$  and  $E_2$  based on FEM simulation of the experimental results.

The stress-strain relation for a  $[0^\circ]$  3D printed specimen is:

$$\begin{bmatrix} \sigma_1 \\ 0 \\ 0 \end{bmatrix} = \begin{bmatrix} Q_{11} & Q_{12} & 0 \\ Q_{12} & Q_{22} & 0 \\ 0 & 0 & Q_{66} \end{bmatrix} \begin{bmatrix} \varepsilon_1^0 \\ \varepsilon_2^0 \\ \gamma_{12}^0 \end{bmatrix} \quad \text{Equation 4-11}$$

This is based on Equation 4-8 with zero values for  $\sigma_2$  and  $\tau_{12}$  due to the experimental set up, exactly same as the Equation 4-1 for the unidirectional lamina. Thus, the elastic constants for unidirectional lamina can be represented by using the elastic constants of  $[0^\circ]$  3D printed specimen.

Since stresses considered in CLT are all independent of time, the analysis should use the time-independent QS stress components, determined from the MR test, rather than the total applied stress which also contains time-dependent viscous stress. In this study, the QS stress vs. stroke curve during the initial loading stage for the stroke less than 0.1mm was used to determine the QS elastic modulus for the specimens. Figure 4-3 (a) presents the curve of applied stress vs. stroke for a  $[0^\circ]$  specimen. The curve shows a linear increase during the initial loading stage with the slope of 64.486 till the first stress relaxation. However, the specimen experienced a sudden stress increase at the onset of the stress relaxation. Causes for such a sudden stress increase are unknown at this stage, but is suspected to be related to the driving system of the machine which includes a rubber belt. As shown in Figure 4-3 (a), the applied stress increased suddenly from 5.87MPa to 8.76MPa at the onset of stress relaxation, resulting in a stress overshooting of 49%.

The recorded  $\sigma_r(0)$  at the beginning of the first relaxation stage is 0.34MPa. Therefore, based on the proportionality between applied and QS stresses, the actual  $\sigma_r(0)$  before the overshooting should be:

$$\sigma_r(0) \text{ before overshooting} = \frac{\sigma_r(0) \text{ after overshooting}}{1 + \text{overshooting \%}} = \frac{0.34MPa}{149\%} = 0.23MPa$$

With the same concept the overshooting at the second relaxation stage is 20% and the  $\sigma_r(0)$  before the overshooting 0.59 MPa. Figure 4-3 (b) presents  $\sigma_r(0)$  before the overshooting as a function of stroke for the first two relaxation, which can be fitted using a quadratic function. And the corresponding function for QS stress during the initial loading stage can be determined as:

$$\begin{aligned} f(QS) &= f(\sigma_A) - f(\sigma_r(0) \text{ before overshooting}) \\ &= 64.486x - (0.7985x^2 + 2.2718x) = -2.2718x^2 + 62.21x \end{aligned}$$



The above function is plotted in Figure 4-4, based on which the FEM simulation was used to find the QS elastic modulus ( $E_1$ ) through reproducing the fitting curve for the data shown in Figure 4-4 (with stroke up to 0.1mm). The  $E_1$  value determined from the FEM simulation is  $1800MPa$ .

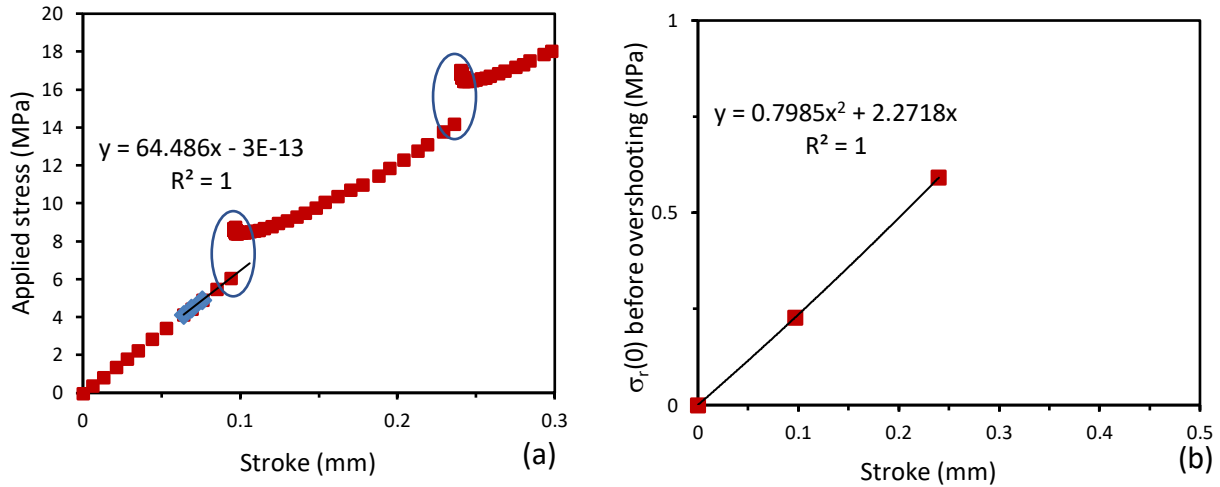


Figure 4-3 Curve fittings for MR test results of a  $[0^\circ]$  3D printed specimen vs. stroke: (a) Linear curve fitting for the initial applied stress, with circles to indicate the overshooting of applied engineering stress at the onset of the relaxation stages, (b) Polynomial curve fitting for the first three points of  $\sigma_r(0)$ .

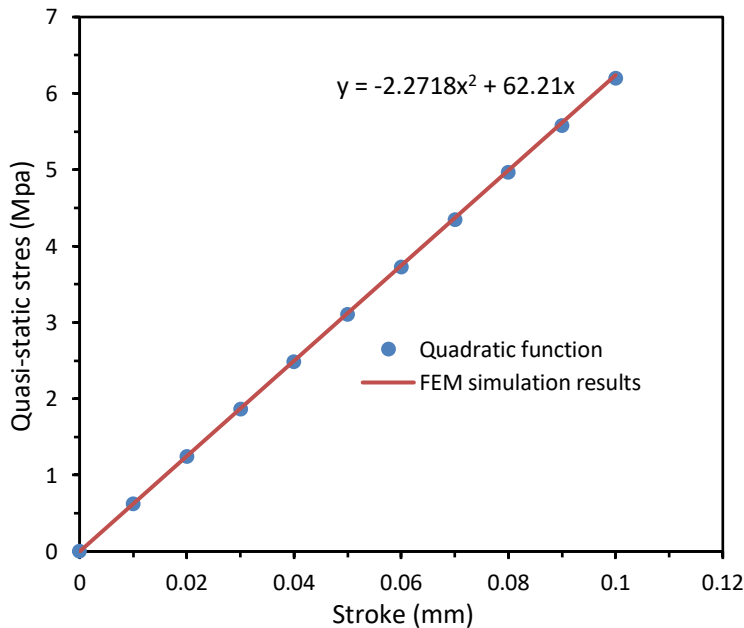


Figure 4-4 Linear fitting of QS stress vs. stroke quadratic function based on experimental data with FEM simulation results for a  $[0^\circ]$  3D printed specimen, using QS elastic modulus of  $E_1 = 1800MPa$

The QS elastic modulus may vary for the same type of 3D printed specimens due to data scattering, at least one more  $E_1$  value is needed to evaluate possible variation for the  $E_1$  values. Since the  $\sigma_r(0)$  values from two duplicate MR tests suppose to be very close to each other during the early relaxation stages, thus the same  $\sigma_r(0)$  function as shown in Figure 4-3 (b) will be used for another set of MR test for a  $[0^\circ]$  3D printed specimen, the experimental applied stress slope for another  $[0^\circ]$  specimen is 61.03, thus  $E_1 = 1700 \text{ MPa}$  is determined.

The same analysis approach is used for  $[90^\circ]$  3D printed specimen, for which axis 2 is the loading direction. Comparison of the initial slope of engineering stress vs. stroke from the MR test and monotonic tensile test is shown in Figure 4-5 (a) below, with using the same  $\sigma_r(0)$  function before overshooting determined from MR test for  $[90^\circ]$  specimen, as shown in the Figure 4-5 (b). The results of  $E_2$  are 900MPa, 840MPa and 800MPa. For the comparison, only the largest and the smallest  $E_2$  values were chosen to evaluate the variability of the prediction based on CLT, i.e., using  $E_2 = 800$  and 900 MPa.

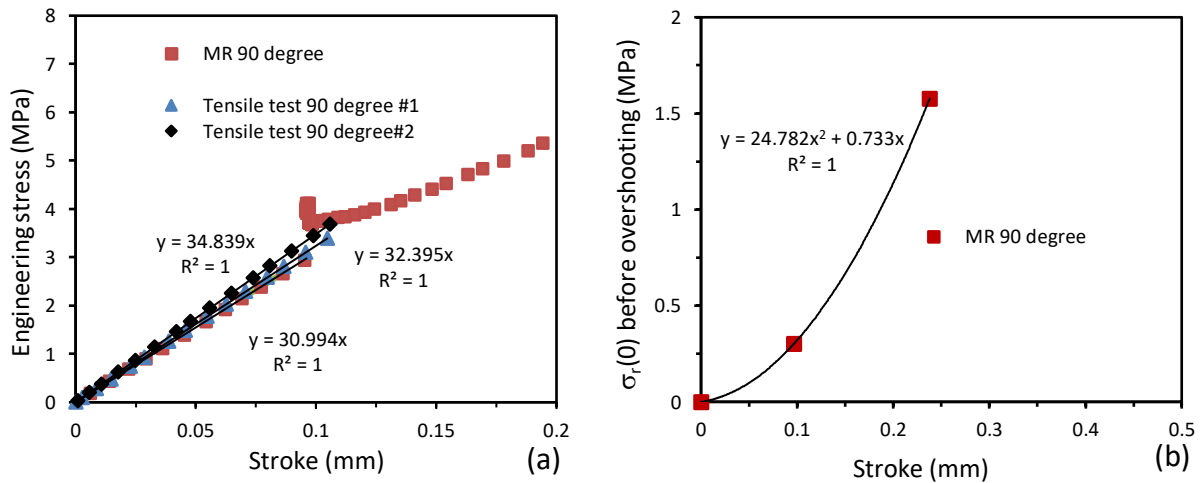


Figure 4-5 The initial slopes of engineering stress vs. stroke curves for  $[90^\circ]$  3D printed specimens using MR test and monotonic tensile test.

In summary, two  $E_1$  values 1800 MPa and 1700 MPa and two  $E_2$  values 900 MPa and 800 MPa were used to have four possible sets of  $E_1$  and  $E_2$  values that were used to predict QS elastic modulus  $E_x$  for  $[\pm\theta]_s$  3D printed specimens.

#### 4.2.3 Prediction of the elastic constants

The remaining unknown elastic constant for the unidirectional lamina is  $G_{12}$ , which was determined following the approach given in ref. [35], for which the determination required filament volume fraction ( $V_f$ ) and void volume fraction ( $V_v$ ) for the FDM parts. For this purpose, XCT technique was used to determine the volume fraction for filament and void in the 3D printed specimens.

As shown in the Figures 4-6 (a), (b) and (e), five different regions (darkened areas) were chosen to determine the volume fractions for each type of specimens. With the consideration that 3D printed  $[90^\circ]$  specimens have the same volume fractions as the  $[0^\circ]$  specimens, no test was conducted on the former specimens to determine their  $V_f$  and  $V_v$  values. Figures 4-6 (c) and (d) used red circles to show some examples of imperfections in the 3D printed  $[\pm 30^\circ]_s$  specimens. These areas were avoided in the examination. The XCT results are shown in Figure 4-4. The figure suggests that for the same type of specimens, difference of  $V_f$  among five chosen areas is around 1%. Therefore, a 1% error bar is used for each data point in the figure. The results show that the difference of  $V_f$  among different types of 3D printed specimens is negligible, especially with the consideration of the 1% error. This means that the change of the printing directions has little effect on  $V_f$ . As a result, a mean  $V_f$  value of 88% is chosen for 3D printed  $[0^\circ]$  specimen for the prediction of the elastic constants, and the same  $V_f$  value is used for  $[\pm 30^\circ]_s$  and  $[\pm 45^\circ]_s$  3D printed specimens.

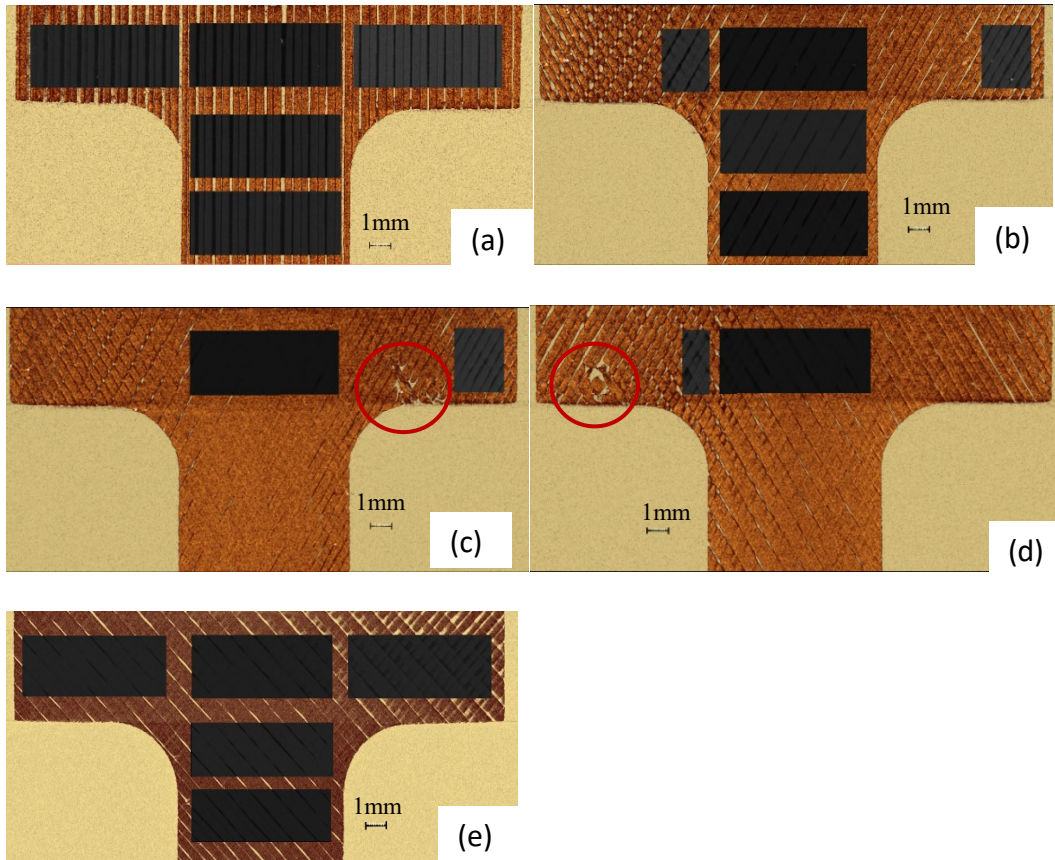


Figure 4-6 Segment processing of scanned 3D printed specimens in which five different stages (darkened area) were chosen for a 3D printed specimen: (a)  $[0^\circ]$ , (b)  $[\pm 30^\circ]_s$ , (c) imperfections in the  $[\pm 30^\circ]_s$  at the right side, (d) imperfections in the  $[\pm 30^\circ]_s$  at the left side, and (e)  $[\pm 45^\circ]_s$

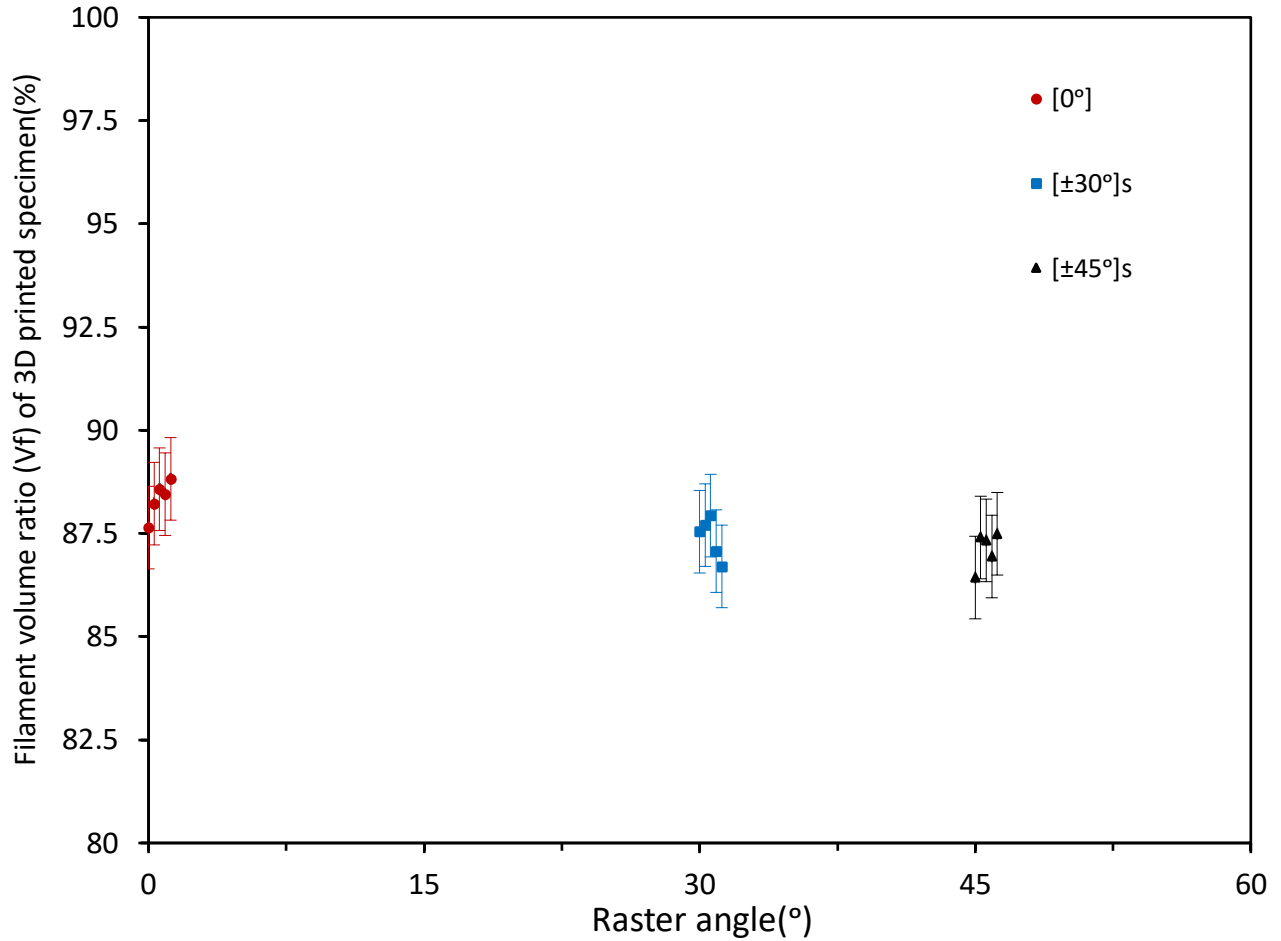


Figure 4-7 Plot of filament volume ratio ( $V_f$ ), in % of total volume, vs. raster angle ( $^\circ$ ) with error bar of 1% for three different types of 3D printed specimens. Five stages were chosen for each type of specimens.

For 3D printed specimens, there is no additional material used as the matrix. Rather, the matrix is represented by the same material that bonds the adjacent filaments. So, the rest of 12% is the average matrix volume  $V_m$  which represents the combination of voids and bonding material between the filaments, which are assumed to be a homogenous, elastic, and isotropic, with the properties directly related to the bonding between the filaments. As a result, the 3D printed specimen can be considered as a composite material that consists of filament and an average matrix, both being isotropic.

To determine the elastic constants for the ‘composite material,’ shear modulus ( $G_{12}$ ) for the filament and for the average matrix,  $G_f$  and  $G_m$ , respectively, need to be determined first, based

on linear elastic, isotropic material properties.  $G_f$  and  $G_m$  are related to  $E_f$ ,  $E_m$ ,  $\nu_f$  and  $\nu_m$  by the equations below [35]:

$$G_f = \frac{E_f}{2(1+\nu_f)}$$

$$G_m = \frac{E_m}{2(1+\nu_m)} \quad \text{Equation 4-12}$$

Values for the four constants that are needed to calculate  $G_f$  and  $G_m$ , are assigned to be filament QS elastic modulus for  $E_f$ , average matrix QS elastic modulus for  $E_m$ , filament Poisson's ratio for  $\nu_f$  and average matrix Poisson's ratio for  $\nu_m$ . A unidirectional lamina can be represented by a periodic structure that is formed by a representative volume element (RVE), defined as the smallest part of the material that can represent the whole material structure. Based on the strength of materials approach [35], the RVE can be represented by rectangular filament surrounded by the matrix, as shown in the Figure 4-7 [35], with  $E_1$  and  $E_2$  expressed as functions of  $E_f$  and  $E_m$ :

$$E_1 = E_f V_f + E_m V_m \quad \text{Equation 4-13}$$

$$\frac{1}{E_2} = \frac{V_f}{E_f} + \frac{V_m}{E_m} \quad \text{Equation 4-14}$$

After  $E_1$ ,  $E_2$ ,  $V_f$  and  $V_m$  were experimentally measured, Eqn.4-13 and 4-14 could then be used to determine  $E_f$  and  $E_m$  values.

Based on the strength of materials approach [35], Poisson's ratios for filament ( $\nu_f$ ) and average matrix ( $\nu_m$ ) have the following relationship with  $\nu_{12}$ .

$$\nu_{12} = \nu_f V_f + \nu_m V_m \quad \text{Equation 4-15}$$

Based on  $\nu_{12}=0.33$ , and  $\nu_f = 0.35$  [44], value for  $\nu_m$  was determined to be 0.18.

Values for  $G_f$  and  $G_m$  were determined using Equation 4-12, which were then used to predict the value for  $G_{12}$ . Based on the mechanics of materials approach [35],  $G_{12}$  is expressed as:

$$\frac{1}{G_{12}} = \frac{V_f}{G_f} + \frac{V_m}{G_m} \quad \text{Equation 4-16}$$

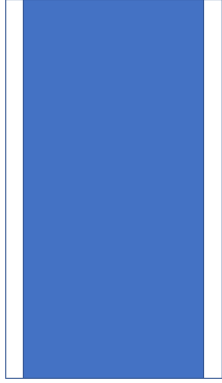


*Figure 4-8 Cross section view of representative volume element (RVE) of a unidirectional lamina based on mechanics of materials approach, blue area is filament and white area is matrix.*

All the elastic constants needed in CLT to predict elastic modulus for a unidirectional lamina, based on the mechanics of materials approach, are summarized in Table 4-1 with four combinations of possible  $E_1$  and  $E_2$  values.

However, Hashin [45] reported that for unidirectional glass/epoxy lamina with  $V_f$  in the range from 0.45 to 0.75, experimental results of  $E_2$  and  $G_{12}$  are higher than those predicted using the mechanics of materials approach, suggesting that the mechanics of materials approach may underestimate the  $E_2$  and  $G_{12}$  values for fiber composites. Therefore, elasticity model [46][47] was introduced. Since the predicted values for  $E_1$  and  $\nu_{12}$  using the elasticity model are very similar to those using the mechanics of materials approach [45], only equations from elasticity model to predict  $E_2$  and  $G_{12}$  were considered. For the prediction of  $G_{12}$ , one elasticity model named composite cylinder assemblage (CCA) model was adopted [45]. RVE for the CCA model is a single solid cylinder (filament) surrounded by cylindrical matrix, arranged in a hexagonal packing pattern with the maximum fibre volume fraction of 91% [53], so CCA model is valid to be used for specimens with  $V_f=88\%$ . as shown in Figure 4-8. The corresponding equation for  $G_{12}$ , expressed in terms of  $G_m$  and  $G_f$  [45] [48-50], is:

$$G_{12} = G_m \frac{G_m V_m + G_f (1 + V_f)}{G_f V_m + G_m (1 + V_f)} \quad \text{Equation 4-17}$$

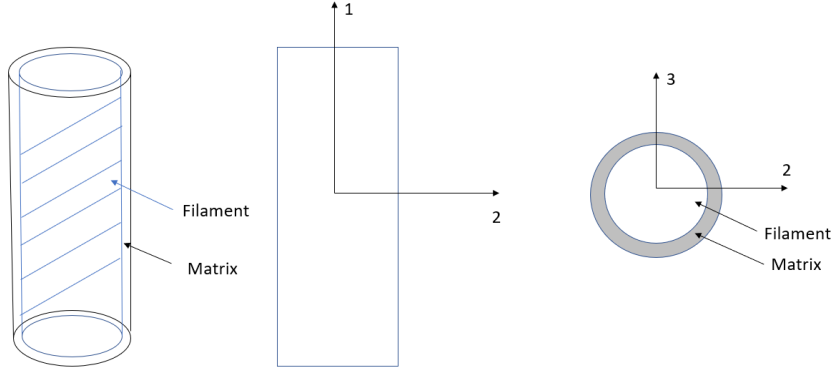


Figure 4-9 RVE of a unidirectional lamina based on CCA model(left), front view 1-2 axis(middle) and top view 2-3 axis (right).

Another elasticity model, named three-phase model [45] where the filament is surrounded by matrix and then surrounded by a homogeneous material that is equivalent to the composite, is used to derive the exact solution for  $E_2$  [45] for which the expression is given below.

$$E_2 = 2(1 + \nu_{23})G_{23} \quad \text{Equation 4-18}$$

where  $\nu_{23}$  is the transverse Poisson's ratio and  $G_{23}$  the transverse shear modulus on the 2-3 plane.

The transverse Poisson's ratio  $\nu_{23}$  is given by [51]:

$$\nu_{23} = \frac{K^* - mG_{23}}{K^* + mG_{23}} \quad \text{Equation 4-19}$$

where  $m$  is expressed as:

$$m = 1 + 4K^* \frac{\nu_{12}^2}{E_1} \quad \text{Equation 4-20}$$

And  $K^*$  is the bulk modulus of the composite material, expressed as:

$$K^* = \frac{K_m(K_f + G_m)V_m + K_f(K_m + G_m)V_f}{(K_f + G_m)V_m + (K_m + G_m)V_f} \quad \text{Equation 4-21}$$

$K_f$  and  $K_m$  are filament bulk modulus and average matrix bulk modulus, respectively. The equations are given by:

$$K_f = \frac{E_f}{2(1+\nu_f)(1-2\nu_f)}$$

$$K_m = \frac{E_m}{2(1+\nu_m)(1-2\nu_m)} \quad \text{Equation 4-22}$$



The transverse shear modulus on the 2-3 plane,  $G_{23}$ , is determined using the following function [48]:

$$A\left(\frac{G_{23}}{G_m}\right)^2 + 2B\left(\frac{G_{23}}{G_m}\right) + C=0 \quad \text{Equation 4-23}$$

where A, B and C are:

$$A=3V_fV_m^2(\gamma - 1)(\gamma + \eta_f) + [\gamma\eta_m + \eta_f\eta_m - (\gamma\eta_m - \eta_f)V_f^3][V_f\eta_m(\gamma - 1) - (\gamma\eta_m + 1)]$$

$$B=-3V_fV_m^2(\gamma - 1)(\gamma + \eta_f) + \frac{1}{2} [\gamma\eta_m + (\gamma - 1)V_f + 1][(\eta_m - 1)(\gamma + \eta_f) - 2(\gamma\eta_m - \eta_m)V_f^3] + \frac{V_f}{2}(\eta_m + 1)(\gamma - 1)[\gamma + \eta_f + (\gamma\eta_m - \eta_f)V_f^3]$$

$$C=3V_fV_m^2(\gamma - 1)(\gamma + \eta_f) + [\gamma\eta_m + (\gamma - 1)V_f + 1][\gamma + \eta_f + (\gamma\eta_m - \eta_f)V_f^3]$$

$$\eta_f = 3 - 4\nu_f \quad \eta_m = 3 - 4\nu_m \quad \gamma = \frac{G_f}{G_m} \quad \text{Equation 4-24}$$

$\nu_{23}$  and  $G_{23}$  are related to the other elastic constants that were introduced before, and thus by using equation 4-17 and 4-18 for the prediction of  $G_{12}$  and  $E_2$  based on the elasticity model approach, with equations 4-13 and 4-15 for the prediction of  $E_1$  and  $\nu_{12}$  from the mechanics of materials approach, all of the elastic constants for the unidirectional lamina which are needed for CLT can be determined. The MATLAB code used to solve the system of equations of Equations 4-12, 13, 15 and 17-24 are given in Appendix B. By taking  $E_1=1800$  MPa and  $E_2=800$  MPa as an example, results are summarized in Table 4-1 with two possible values for each of  $E_1$  and  $E_2$ . Note that the predicted  $G_{12}$  using the elasticity model approach has a better agreement with Hashin's [45] experimental data. However, the experiment data presented in ref. [45] are for fibre composite materials only. It is not clear whether this model is also suitable for 3D printed PETG. Therefore,  $G_{12}$  values obtained from both the mechanics of materials approach and the elasticity model approach are presented to evaluate their suitability for prediction of the QS elastic modulus  $E_x$  for the 3D printed PETG.

Table 4-1 Elastic constants for  $[0^\circ]$  3D printed specimen using two prediction approaches with four combinations of  $E_1$  and  $E_2$ , grey cells are the data known and white cells are predicted data.

	E1/E2 Combination #1	E1/E2 Combination #2	E1/E2 Combination #3	E1/E2 Combination #4
$E_1/E_2$ (MPa)	1800/900	1700/900	1800/800	1700/800
$\nu_{12}$	0.33	0.33	0.33	0.33
Mechanics of materials approach				
$G_{12}$ (MPa)	361	360	323	322
$E_f$ (MPa)	2021	1907	2025	1911
$E_m$ (MPa)	178	185	147	152
Elasticity model approach				
$G_{12}$ (MPa)	378	375	342	339
$E_f$ (MPa)	2030	1916	2033	1919
$E_m$ (MPa)	114	118	94	97

As shown in Table 4-1, for the same  $E_1$  and  $E_2$  values, the predicted  $G_{12}$  using the mechanics of materials approach is slightly smaller than that using the elasticity model approach. The main difference between the extruded specimen and  $[0^\circ]$  3D printed specimen is the presence of voids in the  $[0^\circ]$  specimen, thus the  $E_f$  value should be close to the QS elastic modulus for conventionally extruded specimen. The QS elastic modulus for conventionally extruded specimen is experimentally determined to be 2090 MPa which is close to the  $E_f$  values presented in Table 4-1. Therefore, this verifies the validity of using this approach to predict  $E_f$  values.

#### 4.2.4 Prediction QS elastic modulus $E_x$ using CLT

The predicted results for  $[\pm 30^\circ]_s$  and  $[\pm 45^\circ]_s$  3D printed specimens using mechanics of materials approach and elasticity model approach are shown in Table 4-2. The average values of the predicted results using different combinations of  $E_1$  and  $E_2$  values with max/min values are also shown in Table 4-2. For given  $E_1$  and  $E_2$  values, the predicted  $E_x$  values using the mechanics of materials approach are slightly lower than using  $G_{12}$  from the elasticity model approach, due to the lower value predicted for  $G_{12}$  from the mechanics of materials approach. Calculation details for the prediction of  $E_x$  values are shown in Appendix C, taking  $E_1=1800$  MPa and  $E_2=800$  MPa as an example.

Table 4-2 Predicted results using CLT for  $[\pm 30^\circ]_s$  and  $[\pm 45^\circ]_s$  specimens, grey cells are the average values of the results for the four  $E_1$  and  $E_2$  combinations and Max/Min predicted values.

$E_1/E_2$ combination	1800/900	1700/900	1800/800	1700/800	Average predicted value	Max/Min
Mechanics of materials approach						
$E_x [\pm 30^\circ]_s$ (MPa)	1315	1272	1253	1211	1263	1315/1211
$E_x [\pm 45^\circ]_s$ (MPa)	1021	1011	926	917	969	1021/917
Elasticity model approach						
$E_x [\pm 30^\circ]_s$ (MPa)	1341	1295	1284	1238	1290	1341/1238
$E_x [\pm 45^\circ]_s$ (MPa)	1054	1040	966	952	1003	1054/952

The QS elastic modulus for  $[\pm 30^\circ]_s$  and  $[\pm 45^\circ]_s$  3D printed specimens are also determined by using the experimental data and FEM simulation. The experiential results from FEM simulation are all shown in the Figure 4-10 with black open circles. The average predictions with error bars to show the maximum and minimum values of the predicted results, as the upper and lower bounds of the predictions, are also included in Figure 4-10, also indicated in Table 4-2 using grey cells. Red open circles in Figure 4-10 are the average predicted results using the mechanics of materials approach, and blue open circles the average predicted results using the elasticity model approach. Figure 4-10 suggests that the predicted results for  $[\pm 30^\circ]_s$  specimens are close to but higher than the average of the experimental results, with the overestimation being 9.8% and 12.2%, for mechanics of materials approach and elasticity models approach, respectively. For the  $[\pm 45^\circ]_s$  specimens, the predicted results from either approach are closer to the average of the experimental data, partly because the two experimental data for the  $[\pm 45^\circ]_s$  specimens are closer to each other than the two experimental data for the  $[\pm 30^\circ]_s$  specimens.

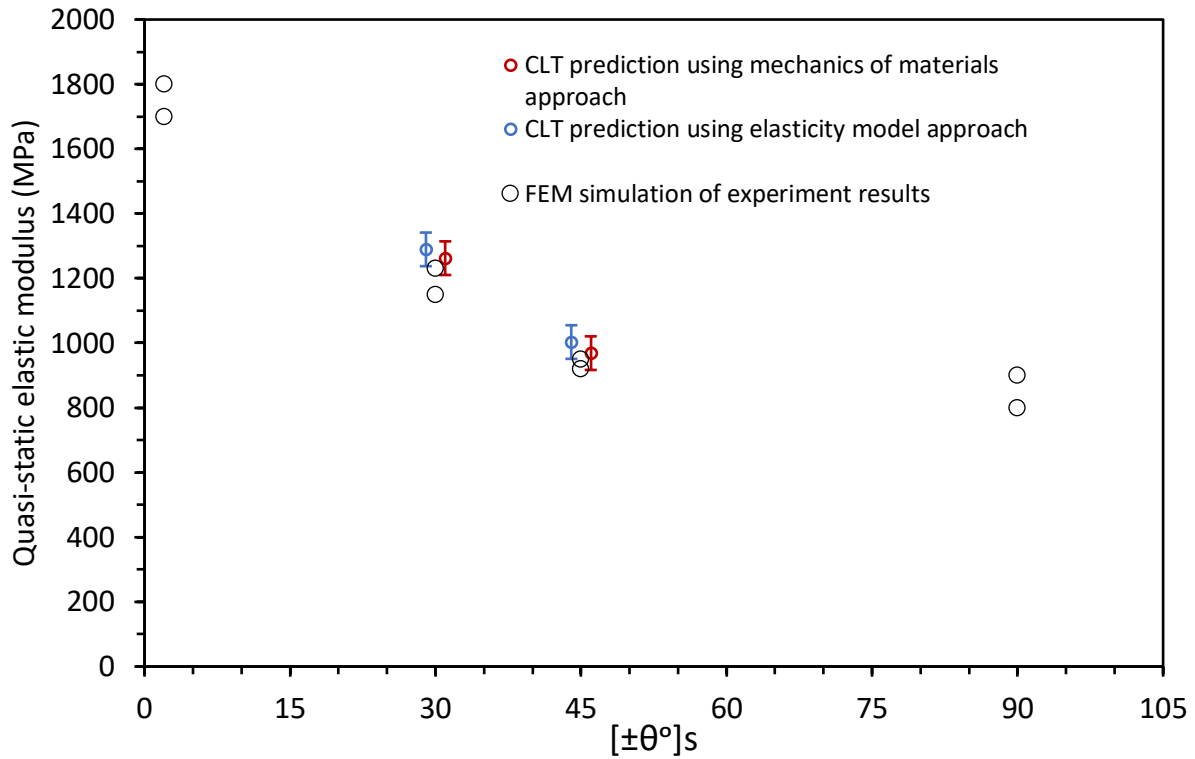


Figure 4-10 Predicted  $E_x$  using CLT with two approaches to predict  $G_{12}$  and FEM simulation of experiment results for 3D printed specimens with different angles.

Difference of the predicted elastic constants using the mechanics of materials and the elasticity models is not significant for the 3D printed PETG. No matter which approach is chosen, CLT can be used to provide a reasonable prediction of  $E_x$  for  $[\pm 30^\circ]_s$  and  $[\pm 45^\circ]_s$  3D printed specimens.

#### 4.3 Modified CLT using adjusted $E_m$ to predict $E_x$

Although CLT can predict the QS elastic modulus  $E_x$  for  $[\pm 30^\circ]_s$  and  $[\pm 45^\circ]_s$  specimens, the predicted results overestimate slightly the measured values for the  $[\pm 30^\circ]_s$  specimens, consistent with results reported in another work [39]. Therefore, it is possible that the overestimate is due to the initial assumptions of the CLT which does not consider the effect of void distribution on the 3D printed specimens, even though the void content has been considered using  $V_f$ . In this study, the CLT is slightly modified by considering the effect of void distribution, based on which the elastic properties of 3D printed specimens are predicted using elastic properties of filament and average matrix that are determined separately.

#### 4.3.1 Difference of interlaminar contact area among specimens of different raster angle configurations

One possible effect of voids is the difference in the interlaminar contact area among specimens of different raster angle configurations. As shown in Figure 4-11, the difference in the interlaminar contact area is shown using three unit cells of  $1 \times 1 \text{ mm}^2$ . Blue area in each unit cell of Figure 4-11 represents the interlaminar contact area among filaments. Figure 4-11(a) is for  $[0^\circ]$  specimen, with the assumption that filaments between layers are perfectly aligned, so that the interlaminar contact area is 88% of the total area, with the rest of the area occupied by voids. For the  $[\pm 30^\circ]_s$  and  $[\pm 45^\circ]_s$  specimens, as shown in the Figures 4-11 (b) and (c), respectively, the interlaminar area between  $30^\circ$  and  $-30^\circ$  layers and between  $45^\circ$  and  $-45^\circ$  layers are shown in blue colour, which results in a decrease in the interlaminar contact area to 73% of the total area, which is caused by some sections of the filament being in contact with voids due to the alternate printing directions. The decrease in the interlaminar area could cause decrease in the mechanical performance of the  $[\pm 30^\circ]_s$  and  $[\pm 45^\circ]_s$  specimens, which could not be considered by CLT as the CLT only considers in-plane contribution of the mechanical properties. As a result of the decrease in the interlaminar contact area, the use of elastic constants for  $[0^\circ]$  3D printed specimens to predict  $E_x$  for  $[\pm 30^\circ]_s$  and  $[\pm 45^\circ]_s$  specimens, CLT could overestimate the predicted results.

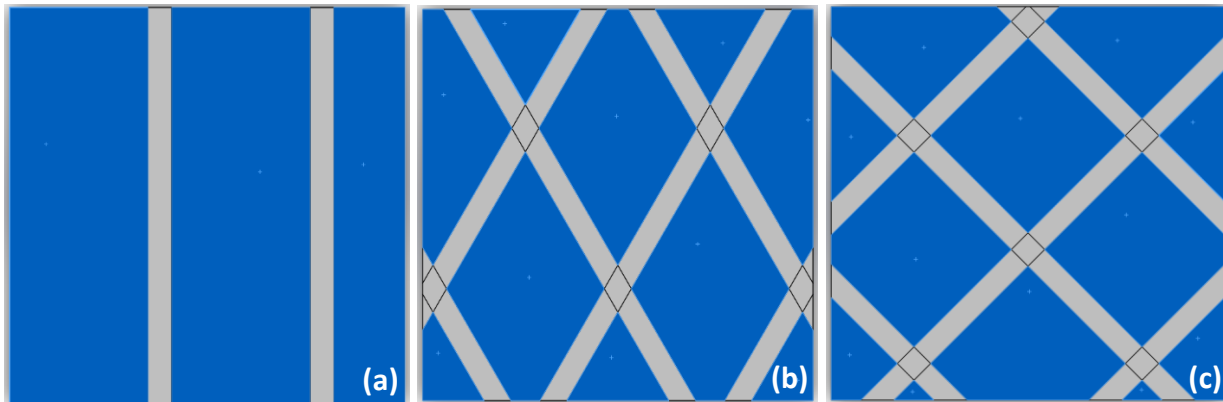


Figure 4-11 Schematic description of difference of interlaminar area (blue area) among different raster angle configurations using  $1 \text{ mm}^2$  unit cell: (a)  $[0^\circ]$  interlaminar area of  $0.88 \text{ mm}^2$ , (b)  $[\pm 30^\circ]_s$  interlaminar area of  $0.73 \text{ mm}^2$ , and (c)  $[\pm 45^\circ]_s$  interlaminar area is  $0.73 \text{ mm}^2$ .

As value for  $E_m$  here reflects directly the bonding between filaments, with the assumption that little bonding exists between filaments in the same lamina, bonding between the filament comes mainly from the interlaminar contact area. Therefore, decrease of the interlaminar area can cause

decrease of the equivalent  $E_m$  value. In the case of  $[\pm 30^\circ]_s$  and  $[\pm 45^\circ]_s$  specimens, the use of the elastic constants of  $[0^\circ]$  specimen is expected to cause overestimate of the bonding by 17%, as shown by the calculation below.

$$\%decreasing = \frac{88\% - 73\%}{88\%} = 17\%$$

With the above consideration, using the same  $E_f$  and  $\nu_{12}$  values from Table 4-1, but with the  $E_m$  values decreased by 17% from the original  $E_m$  values could result in different values for the predicted  $E_1$ ,  $E_2$  and  $G_{12}$  from those based the original  $E_m$  values from Table 4-1. A MATLAB program has been developed to solve the system equations using the elasticity model approach, as shown in Appendix D, taking  $E_m=78$  MPa and  $E_f=2033$  MPa. The predicted elastic constants  $E_1$ ,  $E_2$  and  $G_{12}$  based on adjusted  $E_m$  are shown in the Table 4-3, the original elastic constants from Table 4-1 are also shown in Table 4-3 for comparison, which shows that those predicted elastic constants are all decreased with using adjusted  $E_m$  values compared with the original elastic constants.

*Table 4-3 Predicted elastic constants for prediction of  $E_x$ , based on adjusted  $E_m$  and original  $E_f$ , grey cells are the data known and white cells are predicted data.*

$E_1/E_2$ combination in Table 4.1	1800/900	1700/900	1800/800	1700/800
$\nu_{12}$	0.33	0.33	0.33	0.33
Mechanics of materials approach				
$E_f$ (MPa) based on $[0^\circ]$ specimens	2021	1907	2025	1911
Adjusted $E_m$ (MPa) by 17% decrease	148	154	122	126
$G_{12}$ (MPa) ( $G_{12}$ in Table 4.1)	324 (361)	324 (360)	286 (323)	286 (322)
$E_1/E_2$ (MPa)	1796/802	1697/806	1797/705	1697/708
Elasticity model approach				
$E_f$ (MPa) based on $[0^\circ]$ specimens	2030	1916	2033	1919
Adjusted $E_m$ (MPa) by 17% decrease	95	98	78	81
$G_{12}$ (MPa) ( $G_{12}$ in Table 4.1)	344 (378)	341 (375)	308 (342)	307 (339)
$E_1/E_2$ (MPa)	1798/807	1698/805	1798/709	1698/713

#### 4.3.2 Prediction of QS elastic modulus $E_x$ using modified CLT

The QS elastic modulus  $E_x$  for  $[\pm 30^\circ]_s$  and  $[\pm 45^\circ]_s$  specimens is now predicted using Equation 4-10 again, based on the elastic constants shown in Table 4-3 which were after the decrease of  $E_m$  by 17%. The average % decrease compared to the original CLT prediction is:

$$\text{Average \% decrease compared to original CLT prediction} = \frac{\text{Average original CLT prediction} - \text{Average modified CLT prediction}}{\text{Average original CLT prediction}} * 100\%$$

Equation 4-25

the results show that average percentage decrease using modified CLT compared with original CLT predictions for the  $[\pm 30^\circ]_s$  specimen is about 4-5% while that for the  $[\pm 45^\circ]_s$  specimen is about 8-9%.

*Table 4-4 Prediction of results using modified CLT for  $[\pm 30^\circ]_s$  and  $[\pm 45^\circ]_s$  specimens, grey cells are the average values of the results for the four  $E_1$  and  $E_2$  combinations and Max/Min predicted values.*

Original $E_1/E_2$ combination	1800/900	1700/900	1800/800	1700/800	Average predicted value	Max/Min	Average % decrease compared to original CLT prediction
Mechanics of materials approach							
Predicted $E_x$ $\pm[30^\circ]_s$ (MPa)	1253	1213	1189	1150	1201	1253/1150	4.8%
Predicted $E_x$ $\pm[45^\circ]_s$ (MPa)	930	923	836	829	880	930/880	9.2%
Elasticity model approach							
Predicted $E_x$ $\pm[30^\circ]_s$ (MPa)	1286	1240	1227	1185	1235	1286/1185	4.3%
Predicted $E_x$ $\pm[45^\circ]_s$ (MPa)	971	956	882	873	921	971/873	8.2%

Average of the predicted results using square symbols and Max/Min values using error bars to indicate the upper and lower bounds of the results are presented in Figure 4-12 (data are grey cells in Table 4-4), original predicted results from Table 4-2 are also presented in Figure 4-12 using triangular symbols for comparison. Data in blue colour are based on the elasticity model approach and in red colour based on the mechanics of materials approach. The experimental results are shown in Figure 4-12 using open black circles.

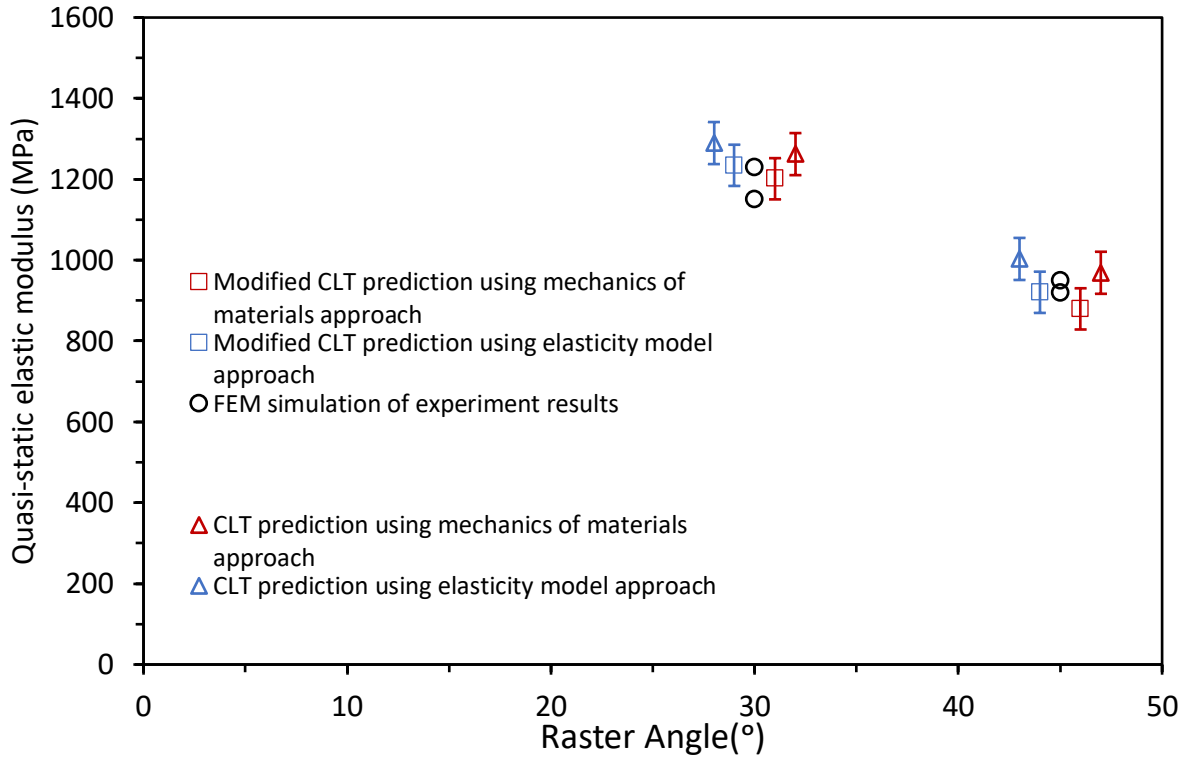


Figure 4-12 Predicted  $E_x$  using modified CLT with adjusted  $E_m$  equals to 83% of original  $E_m$ , the original CLT prediction results using two prediction elastic constants approaches, and FEM simulation of experimental  $E_x$  results.

After modifying the  $E_m$  value, all values for the predicted results dropped, with the predicted results for the  $[\pm 30^\circ]_s$  specimens being closer to the experimental results, suggesting that modified CLT provides a better prediction for  $[\pm 30^\circ]_s$  specimens. For the  $[\pm 45^\circ]_s$  specimens, the predicted results from either the Mechanics of materials approach or the Elasticity model approach are still close to the experimental results, but without a clear improvement from the original CLT method.

Prediction based on CLT is suggested to use the time-independent QS stress, rather than the applied stress which includes the time-dependent component. Overall, the CLT can provide a reasonable prediction of the QS elastic modulus for  $[\pm 30^\circ]_s$  and  $[\pm 45^\circ]_s$  specimens using the above two approaches, and there is no clear difference between the two approaches in this study. Modifications of the CLT is presented which considers effect of voids in the interlaminar region, due to change of the raster angle configurations, on the  $E_m$  values, even with the same  $V_f$ . This modification provides improvement in the ability of CLT to predict the experimental results.



## Chapter 5 Summary and future works

Main findings of the work done in the thesis are summarized below, followed by suggestions for the future work.

### 5.1 Summary of current work

This study focuses on an increasingly used 3D printed material PETG. Although some researchers already investigated the mechanical behaviours of the PETG 3D printed specimens, few of them focused on the analysis of relaxation behaviour of PETG. In this study, a newly developed MR test is used to characterize the relaxation behaviour of PETG specimens to determine the quasi-static stress component. The main findings in this study are summarized below:

1. The presence of holes in specimen tabs has significantly degraded the mechanical performance of  $[0^\circ]$  and  $[\pm 30^\circ]_s$  3D printed specimens as their fracture locations are around the holes. Therefore, 3D printed specimens without holes have been chosen for the analysis.
2. Comparison of MR test results for conventionally extruded and 3D printed PETG specimens was made. The results show that  $[0^\circ]$  specimen is less stiff than the extruded specimen, but the ratio of QS stress to the applied stress do not show any clear difference. Therefore, it is believed that the differences between PETG specimens using these two methods are mainly caused by the voids in the  $[0^\circ]$  specimens.
3. Comparison of MR test results for 3D printed specimens with different raster angle configurations,  $[0^\circ]$ ,  $[\pm 30^\circ]_s$  and  $[\pm 45^\circ]_s$  suggests that the raster angles have significant effects on the mechanical performance of 3D printed specimens, with the stiffness in the order of  $[0^\circ] > [\pm 30^\circ]_s > [\pm 45^\circ]_s$ .
4. Different 3D printed specimens show different fracture behaviour.  $[0^\circ]$  specimen survived from the test, and  $[\pm 30^\circ]_s$  and  $[\pm 45^\circ]_s$  specimens started fracture in the middle of the tests.
5. Raster angles have a significant effect on the relaxation behaviour of 3D printed specimens, the ratio of QS to applied stresses for 3D printed specimens shows some difference.

6. For each type of PETG specimens, the relationship between applied stress and QS stress, and relaxation fitting parameters ( $\sigma_r(0)$ ,  $\sigma_0$  and  $\tau_r$ ) are investigated. Three obvious transition points for applied stress were detected during the deformed process.
7. The comparison of applied stress with QS stress,  $\sigma_r(0)$ ,  $\sigma_0$  and  $\tau_r$  among different types of PETG 3D printed specimens suggests that the stress curves for the  $[\pm 30^\circ]_s$  specimen decreasing slowly and then fractured after the second transition point. This is different from the stress curves for any other PETG specimens. Variation of  $\sigma_r(0)$ ,  $\sigma_0$  and  $\tau_r$  as a function of stroke for the  $[\pm 30^\circ]_s$  specimen after the second transition point also showed different behaviour compared to other types of specimens.
8.  $\sigma_0$  curve does not always reflect the first transition point in applied stress curves for all types of PETG specimens, but  $\sigma_r(0)$  curves do.  $\tau_r$  value shows little correlation with the transition points of the applied stress. However, different  $\tau_r$  values are needed for different range of stroke.
9. Time independent QS stress is suggested to used for the analysis of CLT, CLT is valid for prediction of the QS elastic modulus  $E_x$  for  $[\pm 30^\circ]_s$  and  $[\pm 45^\circ]_s$  3D printed specimens.
10. With the consideration of the effect of voids on the mechanical performance of 3D printed specimens with different raster angles, modifications to the CLT can provide better prediction.

## 5.2 Future work

Suggestions for the future works are summarized below:

1. The possible transition points from  $\sigma_0$  curves between the second and the third transition points need to be further investigated.
2. The 3D printed specimens with 100% infill percentage still have voids in the specimens. Possibility of producing 3D printed specimens without voids should explored in the future study, to improve consistency of the results and to remove the potential effects of voids when making comparisons among different types of 3D printed specimens.
3. Microstructural analysis and additional experiments are needed to investigate the difference of fracture behaviours among 3D printed specimens

4. The behaviour of overshooting of the applied stress at the onset of each relaxation stage for PETG specimens need to be further investigated.

## APPENDIX

### Appendix A Detail calculations of applying CLT equations to 3D printed specimen

Applying analytical equations from CLT to the 3D printed specimens with different raster angle configurations. Since the midplane curvatures are 0 due to the experimental setup, the equations from CLT can be rewritten as:

$$\begin{bmatrix} N_x \\ N_y \\ N_{xy} \end{bmatrix} = \begin{bmatrix} A_{11} & A_{12} & A_{16} \\ A_{12} & A_{22} & A_{26} \\ A_{16} & A_{26} & A_{66} \end{bmatrix} \begin{bmatrix} \varepsilon_x^0 \\ \varepsilon_y^0 \\ \gamma_{xy}^0 \end{bmatrix}$$

$$\begin{bmatrix} M_x \\ M_y \\ M_{xy} \end{bmatrix} = \begin{bmatrix} B_{11} & B_{12} & B_{16} \\ B_{12} & B_{22} & B_{26} \\ B_{16} & B_{26} & B_{66} \end{bmatrix} \begin{bmatrix} \varepsilon_x^0 \\ \varepsilon_y^0 \\ \gamma_{xy}^0 \end{bmatrix} \quad \text{Equation A-1}$$

For all 3D printed specimens, each layer thickness is 0.2mm with total of 16 layers, 8 layer on the top of the middle plane and 8 layers on the bottom, so  $h/2$  is 1.6mm and  $h_k - h_{k-1}$  is 0.2mm. For  $[0^\circ]$  3D printed specimen, since each lamina is unidirectional lamina with direction 1 for the filament direction and direction 2 for the transverse direction, so the reduced stiffness matrix for  $[0^\circ]$  3D printed specimen is  $Q_{ij}$ . In Equation 4-7, the matrix A for  $[0^\circ]$  3D printed specimen is:

$$A_{ij} = \sum_{k=1}^n (Q_{ij})_k (h_k - h_{k-1})$$

$$A_{ij} = Q_{ij} * (-1.4 - (-1.6)) + Q_{ij} * (-1.2 - (-1.4)) + \dots + Q_{ij} * (1.6 - (1.4)) = h * Q_{ij}$$

Where h is the thickness of the specimen, 3.2mm. The matrix B for  $[0^\circ]$  3D printed specimen is:

$$B_{ij} = \frac{1}{2} \sum_{k=1}^n (Q_{ij})_k (h_k^2 - h_{k-1}^2)$$

$$B_{ij} = \frac{1}{2} (Q_{ij} * ((-1.4)^2 - (-1.6)^2) + Q_{ij} * ((-1.2)^2 - (-1.4)^2) + \dots + Q_{ij} * (1.4^2 - 1.2^2) + Q_{ij} * (1.6^2 - 1.4^2)) = 0 \quad \text{Equation A-2}$$

The angle from x-axis to printing direction clockwise to be defined as positive raster angle, but from Fig.4-1, the angle lamina with angle  $\theta$  is counterclockwise from x-axis. Therefore, the reduced stiffness matrices for  $[\pm 30^\circ]_s$  3D printed specimen can be noted as  $[\bar{Q}]_{+30}$  for  $-30^\circ$

laminate layers and  $[\bar{Q}]_{-30}$  for  $+30^\circ$  laminate layers, with  $\theta$  of  $+30^\circ$  and  $-30^\circ$ , respectively. So  $[\bar{Q}]_{+30}$  can be written as:

$$[\bar{Q}]_{+30} = \begin{bmatrix} \bar{Q}_{11+30} & \bar{Q}_{12+30} & \bar{Q}_{16+30} \\ \bar{Q}_{12+30} & \bar{Q}_{22+30} & \bar{Q}_{26+30} \\ \bar{Q}_{16+30} & \bar{Q}_{26+30} & \bar{Q}_{66+30} \end{bmatrix}$$

While the elements in  $[\bar{Q}]_{-30}$  are relative to the elements in  $[\bar{Q}]_{+30}$  as shown below:

$$[\bar{Q}]_{-30} = \begin{bmatrix} \bar{Q}_{11+30} & \bar{Q}_{12+30} & -\bar{Q}_{16+30} \\ \bar{Q}_{12+30} & \bar{Q}_{22+30} & -\bar{Q}_{26+30} \\ -\bar{Q}_{16+30} & -\bar{Q}_{26+30} & \bar{Q}_{66+30} \end{bmatrix}$$

Then matrix A and B for  $[\pm 30^\circ]_s$  3D printed specimen are:

$$A_{ij} = [\bar{Q}]_{-30} * (-1.4 - (-1.6)) + [\bar{Q}]_{+30} * (-1.2 - (-1.4)) + \dots + [\bar{Q}]_{+30} * (1.4 - 1.2) \\ + [\bar{Q}]_{-30} * (1.6 - 1.4) = h * \begin{bmatrix} \bar{Q}_{11+30} & \bar{Q}_{12+30} & 0 \\ \bar{Q}_{12+30} & \bar{Q}_{22+30} & 0 \\ 0 & 0 & \bar{Q}_{66+30} \end{bmatrix}$$

$$B_{ij} = \frac{1}{2} ([\bar{Q}]_{-30} * ((-1.4)^2 - (-1.6)^2) + [\bar{Q}]_{+30} * ((-1.2)^2 - (-1.4)^2) + \dots + [\bar{Q}]_{+30} * \\ (1.4^2 - 1.2^2) + [\bar{Q}]_{-30} * (1.6^2 - 1.4^2)) = 0 \quad \text{Equation A-3}$$

Similarly, the reduced stiffness matrices for  $[\pm 45^\circ]_s$  3D printed specimen can be written as:

$$[\bar{Q}]_{+45} = \begin{bmatrix} \bar{Q}_{11+45} & \bar{Q}_{12+45} & \bar{Q}_{16+45} \\ \bar{Q}_{12+45} & \bar{Q}_{22+45} & \bar{Q}_{26+45} \\ \bar{Q}_{16+45} & \bar{Q}_{26+45} & \bar{Q}_{66+45} \end{bmatrix}$$

$$[\bar{Q}]_{-45} = \begin{bmatrix} \bar{Q}_{11+45} & \bar{Q}_{12+45} & -\bar{Q}_{16+45} \\ \bar{Q}_{12+45} & \bar{Q}_{22+45} & -\bar{Q}_{26+45} \\ -\bar{Q}_{16+45} & -\bar{Q}_{26+45} & \bar{Q}_{66+45} \end{bmatrix}$$

Matrix A and B for  $[\pm 45^\circ]_s$  3D printed specimen are:

$$A_{ij} = [\bar{Q}]_{-45} * (-1.4 - (-1.6)) + [\bar{Q}]_{+45} * (-1.2 - (-1.4)) + \dots + [\bar{Q}]_{+45} * (1.4 - 1.2) \\ + [\bar{Q}]_{-45} * (1.6 - 1.4) = h * \begin{bmatrix} \bar{Q}_{11+45} & \bar{Q}_{12+45} & 0 \\ \bar{Q}_{12+45} & \bar{Q}_{22+45} & 0 \\ 0 & 0 & \bar{Q}_{66+45} \end{bmatrix}$$

$$B_{ij} = \frac{1}{2} ([\bar{Q}]_{-45} * ((-1.4)^2 - (-1.6)^2) + [\bar{Q}]_{+45} * ((-1.2)^2 - (-1.4)^2) + \dots + [\bar{Q}]_{+45} * \\ (1.4^2 - 1.2^2) + [\bar{Q}]_{-45} * (1.6^2 - 1.4^2)) = 0 \quad \text{Equation A-4}$$

So, matrix B is 0 for all types of 3D printed specimen due to the mirror symmetry of the lamina plates about the middle plane, then laminate resultant moments are 0 for all types of specimens and resultant forces are directly proportional to the reduced stiffness matrix  $\bar{Q}_{ij}$  ( $Q_{ij}$  for  $[0^\circ]$  specimen) except for  $\bar{Q}_{16}$  and  $\bar{Q}_{26}$  are 0 due to equal number of  $+\theta$  and  $-\theta$  lamina plates in each specimen (16 plates for each angle) with a factor of 3.2 which is the total thickness of the 3D printed specimen. So, the resultant forces can be written as the equation below with angle  $\theta$  (Reduced stiffness matrix would become  $Q_{ij}$  when  $\theta$  is  $0^\circ$ ):

$$\begin{bmatrix} N_x \\ N_y \\ N_{xy} \end{bmatrix} = h * \begin{bmatrix} \bar{Q}_{11+\theta} & \bar{Q}_{12+\theta} & 0 \\ \bar{Q}_{12+\theta} & \bar{Q}_{22+\theta} & 0 \\ 0 & 0 & \bar{Q}_{66+\theta} \end{bmatrix} \begin{bmatrix} \varepsilon_x^0 \\ \varepsilon_y^0 \\ \gamma_{xy}^0 \end{bmatrix} \quad \text{Equation A-5}$$

Due to the experiment test is uniaxial loading in x-direction, so  $N_y$  and  $N_{xy}$  are 0, and  $N_x$  is the normal force per unit length in x-direction, so under the small deformation, Eqn.A-5 can be rewritten as:

$$\begin{bmatrix} \sigma_x \\ 0 \\ 0 \end{bmatrix} = \begin{bmatrix} \bar{Q}_{11+\theta} & \bar{Q}_{12+\theta} & 0 \\ \bar{Q}_{12+\theta} & \bar{Q}_{22+\theta} & 0 \\ 0 & 0 & \bar{Q}_{66+\theta} \end{bmatrix} \begin{bmatrix} \varepsilon_x^0 \\ \varepsilon_y^0 \\ \gamma_{xy}^0 \end{bmatrix} \quad \text{Equation A-6}$$

The stiffness matrix for the  $[\pm\theta]_s$  3D printed specimen is denoted as  $\bar{Q}_{ij\pm\theta}$ , then the strains are given by:

$$\begin{bmatrix} \varepsilon_x^0 \\ \varepsilon_y^0 \\ \gamma_{xy}^0 \end{bmatrix} = \begin{bmatrix} \bar{Q}_{11+\theta} & \bar{Q}_{12+\theta} & 0 \\ \bar{Q}_{12+\theta} & \bar{Q}_{22+\theta} & 0 \\ 0 & 0 & \bar{Q}_{66+\theta} \end{bmatrix}^{-1} \begin{bmatrix} \sigma_x \\ 0 \\ 0 \end{bmatrix} \quad \text{Equation A-7}$$

The inverse matrix of  $\bar{Q}_{ij \pm\theta}$  is denoted as  $\bar{Q}_{ij \pm\theta}^*$ , which is the compliance matrix of the  $[\pm\theta]_s$  3D printed specimen. From Equation A-7,  $\epsilon_x^0 = \bar{Q}_{11+\theta}^* \sigma_x$ , where  $\bar{Q}_{11+\theta}^*$  is the element 11 in the compliance matrix  $\bar{Q}_{ij \pm\theta}^*$ , As  $\epsilon_x^0 = \frac{\sigma_x}{E_x}$ , so the elastic modulus in x-direction for the  $[\pm\theta]_s$  3D printed specimen is:

$$E_x = \frac{1}{\bar{Q}_{11+\theta}^*} \quad \text{Equation A-8}$$

Appendix B MATLAB code for solving the system of equations from elasticity model approach

The MATLAB manuscript use to solve the system of equations from elasticity model approach to predict  $G_{12}$  and solve other elastic constants.

```
clear;
clc;
tic;
syms E1 E2 Ef Em Vf Vm vm vf Kf Km v12 Gm Gf G12 gama A nf nm B C ...
    G23 v23 Ks m
E1=1800;
E2=800;
Vf=0.88;
Vm=0.12;
vf=0.35;
vm=0.18;
eqn1=E1-Ef*Vf-Em*Vm==0;
eqn2=v12-vf*Vf-vm*Vm==0;
eqn3=G12-Gm*(Vm*Gm+(1+Vf)*Gf)/((1+Vf)*Gm+Vm*Gf)==0;
eqn4=Gm-Em/(2*(1+vm))==0;
eqn5=Gf-Ef/(2*(1+vf))==0;
eqn6=Km-Em/(2*(1+vm)*(1-2*vm))==0;
eqn7=Kf-Ef/(2*(1+vf)*(1-2*vf))==0;
eqn8=gama-Gf/Gm==0;
eqn9=nf-3+4*vf==0;
eqn10=nm-3+4*vm==0;
eqn11=A-3*Vf*Vm^2*(gama-1)*(gama+nf)-(gama*nm+nf*nm-(gama*nm-nf)*Vf^3)...
    *(Vf*nm*(gama-1)-(gama*nm+1))==0;
eqn12=B+3*Vf*Vm^2*(gama-1)*(gama+nf)-1/2*(gama*nm+(gama-1)*Vf+1)*((nm-1)...
    *(gama+nf)-2*(gama*nm-nm)*Vf^3)-Vf/2*(nm+1)*(gama-1)*(gama+nf+(gama*nm...
    -nf)*Vf^3)==0;
eqn13=C-3*Vf*Vm^2*(gama-1)*(gama+nf)-(gama*nm+(gama-1)*Vf+1)*(gama+nf...
    +(gama*nm-nf)*Vf^3)==0;
eqn14=A*(G23/Gm)^2+2*B*(G23/Gm)+C==0;
eqn15=E2-2*(1+v23)*G23==0;
eqn16=v23-(Ks-m*G23)/(Ks+m*G23)==0;
eqn17=m-1-4*Ks*v12^2/E1==0;
eqn18=Ks-(Km*Kf+(Vf*Kf+Vm*Km)*Gm)/(Vm*Kf+Vf*Km+Gm)==0;
```

```
[solEf,solEm,solKf,solKm,solv12,solGm,solGf,...
solG12,solgama,solA,solB,solC,solnf,solnm,solG23,solv23,solKs, solm]= ...
vpasolve([eqn1 eqn2 eqn3 eqn4 eqn5 eqn6 eqn7 eqn8 eqn9 eqn10...
eqn11 eqn12 eqn13 eqn14 eqn15 eqn16 eqn17 eqn18],...
[Ef Em Kf Km v12 Gm Gf G12 gama A B C nf nm G23 v23 Ks m])
```

## Appendix C Detail calculations of the prediction of QS elastic modulus for $[\pm\theta]_s$ 3D printed specimen

The following calculations taking the combination of  $E_1=1800$  MPa and  $E_2=800$  MPa as an example. From predicted  $G_{12}$  using mechanics of materials approach the reduced stiffness matrix Q is:

$$[Q]=\begin{bmatrix} Q_{11} & Q_{12} & 0 \\ Q_{12} & Q_{22} & 0 \\ 0 & 0 & Q_{66} \end{bmatrix} = \begin{bmatrix} \frac{E_1}{1-\nu_{12}\nu_{21}} & \frac{\nu_{21}E_1}{1-\nu_{12}\nu_{21}} & 0 \\ \frac{\nu_{21}E_1}{1-\nu_{12}\nu_{21}} & \frac{E_2}{1-\nu_{12}\nu_{21}} & 0 \\ 0 & 0 & G_{12} \end{bmatrix} = \begin{bmatrix} 1891.55 & 277.43 & 0 \\ 277.43 & 840.69 & 0 \\ 0 & 0 & 323 \end{bmatrix}$$

Then  $\bar{Q}_{ij_{\pm 30}}$  for  $[\pm 30]_s$  specimen, based on Eqns.4-4 is:

$$\bar{Q}_{ij_{\pm 30}} = \begin{bmatrix} \bar{Q}_{11+30} & \bar{Q}_{12+30} & 0 \\ \bar{Q}_{12+30} & \bar{Q}_{22+30} & 0 \\ 0 & 0 & \bar{Q}_{66+30} \end{bmatrix} = \begin{bmatrix} 1462.83 & 443.44 & 0 \\ 443.44 & 937.40 & 0 \\ 0 & 0 & 489.01 \end{bmatrix}$$

The inverse of  $\bar{Q}_{ij_{\pm 30}}$  is

$$[\bar{Q}_{ij_{\pm 30}}]^{-1} = \begin{bmatrix} 7.981 & -3.775 & 0 \\ -3.775 & 12.45 & 0 \\ 0 & 0 & 20.45 \end{bmatrix} \times 10^{-4}$$

Then the predicted QS elastic modulus for  $\pm[30]_s$  3D printed specimen  $E_{\pm 30^\circ}$  is:

$$E_{\pm 30^\circ} = \frac{1}{\bar{Q}_{11+30}^*} = \frac{1}{7.981 \times 10^{-4}} = 1253 \text{ MPa}$$

Similarly, the  $\bar{Q}_{ij_{\pm 45}}$  for  $[\pm 45]_s$  specimen is:



$$\bar{Q}_{ij_{\pm 45}} = \begin{bmatrix} \bar{Q}_{11+45} & \bar{Q}_{12+45} & 0 \\ \bar{Q}_{12+45} & \bar{Q}_{22+45} & 0 \\ 0 & 0 & \bar{Q}_{66+45} \end{bmatrix} = \begin{bmatrix} 1144.77 & 498.77 & 0 \\ 498.77 & 1144.77 & 0 \\ 0 & 0 & 544.35 \end{bmatrix}$$

The predicted QS elastic modulus for  $\pm[45^\circ]_s$  3D printed specimen  $E_{\pm 45^\circ}$  is:

$$E_{\pm 45^\circ} = \frac{1}{\bar{Q}_{11+45}^*} = \frac{1}{1.08 \times 10^{-3}} = 926 \text{ MPa}$$

From predicted  $G_{12}$  using elasticity model approach, the reduced stiffness matrix Q is:

$$[Q] = \begin{bmatrix} 1891.55 & 277.43 & 0 \\ 277.43 & 840.69 & 0 \\ 0 & 0 & 342 \end{bmatrix}$$

Then the predicted QS elastic modulus for  $[\pm 30^\circ]_s$  3D printed specimen  $E_{\pm 30^\circ}$  is:

$$E_{\pm 30^\circ} = \frac{1}{\bar{Q}_{11+30}^*} = \frac{1}{7.791 \times 10^{-4}} = 1284 \text{ MPa}$$

The predicted QS elastic modulus for  $[\pm 45^\circ]_s$  3D printed specimen  $E_{\pm 45^\circ}$  is:

$$E_{\pm 45^\circ} = \frac{1}{\bar{Q}_{11+45}^*} = \frac{1}{1.04 \times 10^{-3}} = 966 \text{ MPa}$$

Appendix D MATLAB code for solving the system of equations with adjusted  $E_m$  for elasticity model approach

**The MATLAB manuscript use to solve the system of equations from elasticity model approach for modified CLT with adjusted  $E_m$  (results from original combination  $E_1/E_2=1800 \text{ MPa}/800 \text{ MPa}$  as an example)**

```
Ef=2033;
Em=78;
Vf=0.88;
Vm=0.12;
vf=0.35;
vm=0.18;
eqn1=E1-Ef*Vf-Em*Vm==0;
eqn2=v12-vf*Vf-vm*Vm==0;
eqn3=G12-Gm*(Vm*Gm+(1+Vf)*Gf)/((1+Vf)*Gm+Vm*Gf)==0;
eqn4=Gm-Em/(2*(1+vm))==0;
eqn5=Gf-Ef/(2*(1+vf))==0;
eqn6=Km-Em/(2*(1+vm)*(1-2*vm))==0;
eqn7=Kf-Ef/(2*(1+vf)*(1-2*vf))==0;
```

```

eqn8=gama-Gf/Gm==0;
eqn9=nf-3+4*vf==0;
eqn10=nm-3+4*vm==0;
eqn11=A-3*Vf*Vm^2*(gama-1)*(gama+nf)-(gama*nm+nf*nm-(gama*nm-nf)*Vf^3)...
*(Vf*nm*(gama-1)-(gama*nm+1))==0;
eqn12=B+3*Vf*Vm^2*(gama-1)*(gama+nf)-1/2*(gama*nm+(gama-1)*Vf+1)*((nm-1)...
*(gama+nf)-2*(gama*nm-nm)*Vf^3)-Vf/2*(nm+1)*(gama-1)*(gama+nf+(gama*nm...
-nf)*Vf^3)==0;
eqn13=C-3*Vf*Vm^2*(gama-1)*(gama+nf)-(gama*nm+(gama-1)*Vf+1)*(gama+nf...
+(gama*nm-nf)*Vf^3)==0;
eqn14=A*(G23/Gm)^2+2*B*(G23/Gm)+C==0;
eqn15=E2-2*(1+v23)*G23==0;
eqn16=v23-(Ks-m*G23)/(Ks+m*G23)==0;
eqn17=m-1-4*Ks*v12^2/E1==0;
eqn18=Ks-(Km*Kf+(Vf*Kf+Vm*Km)*Gm)/(Vm*Kf+Vf*Km+Gm)==0;
[solE1,solE2,solKf,solKm,solv12,solGm,solGf,...
solG12,solgama,solA,solB,solC,solnf,solnm,solG23,solv23,solKs, solm]= ...
vpasolve([eqn1 eqn2 eqn3 eqn4 eqn5 eqn6 eqn7 eqn8 eqn9 eqn10...
eqn11 eqn12 eqn13 eqn14 eqn15 eqn16 eqn17 eqn18],...
[E1 E2 Kf Km v12 Gm Gf G12 gama A B C nf nm G23 v23 Ks m])

```

## Bibliography

- [1] Srivatsan, T. Sudarshan, T. Additive manufacturing, innovations, advances, and applications. CRC Press, Florida, USA 2015.
- [2]. Srivatsan, T. Manigandan, K. Sudarshan, T. Additive manufacturing of materials, Viable techniques, metals, advances, advantages, and applications, Additive Manufacturing, pp. 15–62, CRC Press 2015
- [3] ISO/ASTM 52900:2015(E), Standard Terminology for Additive Manufacturing-General Principles-Terminology, 2015.
- [4] S.S. Crump, Apparatus and Method for Creating Three-dimensional Objects, Stratasys Incorporated, US, 1992.
- [5] P.F. Jacobs, Rapid Prototyping & Manufacturing: Fundamentals of Stereolithography, Society of Manufacturing Engineers, 1992.
- [6] J.-P. Kruth, B. Vandenbroucke, v.J. Vaerenbergh, P. Mercelis, Benchmarking of Different SLS/SLM Processes as Rapid Manufacturing Techniques, 2005.
- [7] L.J. Kumar, C.G. Krishnadas Nair, Current Trends of Additive Manufacturing in the Aerospace Industry, 2017, pp. 39e54.
- [8] S. Curran, P. Chambon, R. Lind, L. Love, R. Wagner, S. Whitted, D. Smith, B. Post, R. Graves, C. Blue, Big area additive manufacturing and hardware-in-the-loop for rapid vehicle powertrain prototyping: A case study on the development of a 3-D-printed Shelby Cobra, SAE Technical Paper, 2016.
- [9] A.A. Zadpoor, J. Malda, Additive manufacturing of biomaterials, tissues, and organs, Ann. Biomed. Eng. 45 (1) (2017) 1e11.
- [10] Brenken, B., Barocio, E., Favaloro, A., Kunc, V., Pipes, R.B. Fused filament fabrication of fiber-reinforced polymers: A review. Addit. Manuf. 21, 1–16, 2018
- [11] What is PETG? ACME Plastics, Inc. (n.d.). Retrieved October 26, 2021, from <https://www.acmeplastics.com/pet-g>.
- [12] Joseph Flynt, PETG filament: Properties, how to use, and Best Brands. 3D Insider. Retrieved October 26, 2021, from <https://3dinsider.com/petg-filament/> ,2018
- [13] G.P. Tandon, T.J. Whitney, R. Gerzeski, H. Koerner, J. Baur, Process parameter effects on interlaminar fracture toughness of FDM printed coupons, Mech. Compos. Multi-functional Mater. 7 (2017) 63e71.

- [14] R.J. Zaldivar, D.B. Witkin, T. McLouth, D.N. Patel, K. Schmitt, J.P. Nokes, Influence of processing and orientation print effects on the mechanical and thermal behavior of 3D-Printed ULTEM® 9085 material, *Addit. Manuf.* 13 (2017) 71e80.
- [15] Barrios, J.; Romero, P. Improvement of surface roughness and hydrophobicity in PETG parts manufactured via fused deposition modeling (FDM): An application in 3D printed self-cleaning parts. *Materials* 2019, 12, 2499.
- [16]. Lee, K.M.; Park, H.; Kim, J.; Chun, D. Fabrication of a superhydrophobic surface using a fused deposition modeling (FDM) 3D printer with poly lactic acid (PLA) filament and dip coating with silica nanoparticles. *Appl. Surf. Sci.* 2019, 467–468, 979–991.
- [17]. Roy, R. *A Primer on Taguchi Method*, 2nd ed.; Society of Manufacturing Engineers (SME): Dearborn, MI, USA, 2010.
- [18] Guessasma, S.; Belhabib, S.; Nouri, H. Printability and tensile performance of 3D printed polyethylene terephthalate glycol using fused deposition modelling. *Polymers* 2019, 11, 1220.
- [19] Sepahi, M. T., Abusalma, H., Jovanovic, V., & Eisazadeh, H. Mechanical properties of 3D-printed parts made of polyethylene terephthalate glycol. *Journal of Materials Engineering and Performance*, 30(9), 6851–6861,2021
- [20] Khosravani, M. R., Soltani, P., & Reinicke, T. Fracture and structural performance of adhesively bonded 3D-printed PETG single lap joints under different printing parameters. *Theoretical and Applied Fracture Mechanics*, 116, 103087,2021
- [21] S. Akpınar, R. Sahin, The fracture load analysis of different material thickness in adhesively bonded joints subjected to fully reversed bending fatigue load, *Theor. Appl. Fract. Mech.* 114 (2021) 102984.
- [22] Salazar-Martín, A. G., García-Granada, A. A., Reyes, G., Gomez-Gras, G., & Puigoriol-Forcada, J. M. Time-dependent mechanical properties in polyetherimide 3D-printed parts are dictated by isotropic performance being accurately predicted by the generalized time hardening model. *Polymers*, 12(3), 678,2020.
- [23] Mainardi, F.; Spada, G. Creep, relaxation and viscosity properties for basic fractional models in rheology. *Eur. Phys. J. Spec. Top.* 2011, 193, 133–160.
- [24] Sadigh, M.A.S. Creep simulation of adhesively bonded joints using modified generalized time hardening model. *J. Mech. Sci. Technol.* 2016, 30, 1555–1561.

- [25] Tan, N., & Jar, P.-Y. B. Determining deformation transition in polyethylene under tensile loading. *Polymers*, 11(9), 2019.
- [26] Hong, K.; Rastogi, A.; Strobl, G. A model treating tensile deformation of semicrystalline polymers: Quasi-static stress-strain relationship and viscous stress determined for a sample of polyethylene. *Macromolecules* 2004, 37, 10165–10173.
- [27] Zhang, W., Wu, A. S., Sun, J., Quan, Z., Gu, B., Sun, B., Cotton, C., Heider, D., & Chou, T.-W. Characterization of residual stress and deformation in additively manufactured ABS polymer and composite specimens. *Composites Science and Technology*, 150, 102–110, 2017
- [28] Eyring, H. Viscosity, plasticity, and diffusion as examples of absolute reaction rates. *J. Chem. Phys.* 1936, 4, 283–291.
- [29] Ward, I.M. The yield behaviour of polymers. *J. Mater. Sci.* 1971, 6, 1397–1417.
- [30] Tervoort, T.A.; Smit, R.J.M.; Brekelmans, W.A.M.; Govaert, L.E. A constitutive equation for the elasto-viscoplastic deformation of glassy polymers. *Mech. Time-Depend. Mater.* 1998, 1, 269–291.
- [31] Thompson, A.; Maskery, I.; Leach, R.K. X-ray computed tomography for additive manufacturing: A review. *Meas. Sci. Technol.* 2016, 27, 072001.
- [32] Wang, X., Zhao, L., Ying, J., Fuh, H., Lee, H.-P., 2019. Effect of porosity on mechanical properties of 3d printed polymers: experiments and micromechanical modeling based on x-ray computed tomography analysis. *Polymers* 11, 1154.
- [33] [www.theobjects.com], O. R. S. (n.d.). Our products. About Us | Our Products. Retrieved November 16, 2021, from <https://www.theobjects.com/company/products.html>.
- [34] Petersmann, S., Spoerk, M., Van De Steene, W., Üçal, M., Wiener, J., Pinter, G., & Arbeiter, F. (2020). Mechanical properties of polymeric implant materials produced by extrusion-based additive manufacturing. *Journal of the Mechanical Behavior of Biomedical Materials*, 104, 103611.
- [35] Kaw, A. K. (2006). In *Mechanics of Composite Materials* (pp. 62–332). Taylor & Francis.
- [36] Kelly, A., Cahn, R. W., & Bever, M. B. (1994). *Concise encyclopedia of composite materials* (pp. 159–162). Pergamon.
- [37] Casavola, C., Cazzato, A., Moramarco, V., & Pappalettere, C. (2016). Orthotropic mechanical properties of fused deposition modelling parts described by classical laminate theory. *Materials & Design*, 90, 453–458.

- [38] Kumar Mishra, P., & P, S. (2020). Prediction of in-plane stiffness of multi-material 3D printed laminate parts fabricated by FDM process using CLT and its mechanical behaviour under tensile load. *Materials Today Communications*, 23, 100955.
- [39] Alaimo, G., Marconi, S., Costato, L., & Auricchio, F. (2017). Influence of meso-structure and chemical composition on FDM 3D-printed parts. *Composites Part B: Engineering*, 113, 371–380. <https://doi.org/10.1016/j.compositesb.2017.01.019>
- [40] Li L, Sun Q, Bellehumeur C, Gu P. Composite modeling and analysis for fabrication of fdm prototypes with locally controlled properties. *J Manuf Process* 2002;4(2):129e41.
- [41] Mallick PK. Fiber-reinforced composites: materials, manufacturing, and design. CRC press; 2007.
- [42] Magalhães, L. C., Volpato, N., & Luersen, M. A. (2013). Evaluation of stiffness and strength in fused deposition sandwich specimens. *Journal of the Brazilian Society of Mechanical Sciences and Engineering*, 36(3), 449–459. <https://doi.org/10.1007/s40430-013-0111-1>
- [43] Huysamen, H. W., Kinnear, W. A., Fonternel, T. E., Turton, E., Yadroitsava, I., & Yadroitsev, I. (2020). 3D printed laryngoscope for endotracheal intubation. *South African Journal of Industrial Engineering*, 31(3). <https://doi.org/10.7166/31-3-2446>
- [44] Özen, A., Ganzosch, G., Barchiesi, E., Auhl, D. W., & Müller, W. H. (2021). Investigation of deformation behavior of PETG-FDM-printed metamaterials with pantographic substructures based on different slicing strategies. *Composites and Advanced Materials*, 30, 263498332110164. <https://doi.org/10.1177/26349833211016477>
- [45] Hashin, Z., Theory of fiber reinforced materials, NASA tech. rep. contract no: NAS1-8818, November 1970.
- [46] Hashin, Z., Analysis of composite materials — a survey, *ASME J. Appl. Mech.*, 50, 481, 1983.
- [47] Knott, T.W. and Herakovich, C.T., Effect of fiber orthotropy on effective composite properties, *J. Composite Mater.*, 25, 732, 1991.
- [48] Christensen, R.M., Solutions for effective shear properties in three phase sphere and cylinder models, *J. Mech. Phys. Solids*, 27, 315, 1979.
- [49] Hyer, M.W., *Stress Analysis of Fiber-Reinforced Materials*, WCB McGraw–Hill, New York, 1998.

- [50] Timoshenko, S.P. and Goodier, J.N., *Theory of Elasticity*, McGraw–Hill, New York, 1970.
- [51] Hashin, Z., Analysis of properties of fiber composites with anisotropic constituents, *ASME J. Appl. Mech.*, 46, 543, 1979.
- [52] Dielectric Manufacturing. (2021, November 19). Material properties of thermoplastic PETG - exceptionally durable. Dielectric Manufacturing. Retrieved March 30, 2022, from <https://dielectricmfg.com/knowledge-base/petg/>
- [53] Spencer, A. (1986). The transverse moduli of fibre-composite material. *Composites Science and Technology*, 27(2), 93–109. [https://doi.org/10.1016/0266-3538\(86\)90066-7](https://doi.org/10.1016/0266-3538(86)90066-7)
- [54] PETG filament - overview, step-by-step settings & problems resolved. rigid.ink. (n.d.). Retrieved March 30, 2022, from <https://rigid.ink/blogs/news/175700615-petg-filament-heres-what-you-need-to-know>